RHEOLOGICAL CHARACTERIZATION OF CELLULOSE NANOMATERIALS FOR QUALITY CONTROL AND PROCESSING

A Dissertation
Presented to
The Academic Faculty

by

Jianshan Liao

In Partial Fulfillment
of the Requirements for the Degree
Doctor of Philosophy in the
School of Chemical & Biomolecular Engineering

Georgia Institute of Technology
May 2021

RHEOLOGICAL CHARACTERIZATION OF CELLULOSE NANOMATERIALS FOR QUALITY CONTROL AND PROCESSING

Approved by:

Dr. Victor Breedveld, Advisor
School of Chemical & Biomolecular Engineering
Georgia Institute of Technology

Dr. Robert Moon
School of Material Science & Engineering
Georgia Institute of Technology

Dr. Saad Bhamla
School of Chemical & Biomolecular Engineering
Georgia Institute of Technology

Dr. Elsa Reichmanis
School of Chemical & Biomolecular Engineering
Georgia Institute of Technology

Dr. Carson Meredith
School of Chemical & Biomolecular Engineering
Georgia Institute of Technology

Date Approved: December 17, 2020

To mom, dad and Xiangyu for the love and support

ACKNOWLEDGEMENTS

First and foremost, I would like to thank Dr. Victor Breedveld for his continuous mentorship of my research work. His perseverance and rigorous attitude to the scientific research, curiosity of the new and the unknown, as well as his attention to the details and the fundamentals greatly influenced me on my way to becoming a scientist. I am grateful for the knowledge and expertise that I have gained from his advising. He gave me a lot of freedom to study what I was interested in and encouraged me to take on many collaboration projects, which broadened my knowledge of other materials. Moreover, I am extremely grateful for his support of my professional growth, such as attending conferences and doing a summer internship. I also really appreciate his support that allowed me to take a few more days off during the holiday and spring breaks to travel and relax. I would also like to thank my committee members, Dr. Saad Bhamla, Dr. Carson Meredith, Dr. Robert Moon and Dr. Elsa Reichmanis for their suggestions and insights about my research. Special thanks to Dr. Robert Moon for helping me understand the manufacturing of the cellulose nanomaterials and providing many useful papers. In addition, I would like to thank my undergraduate research advisors Dr. Greg Thurber and Dr. Ron Larson for having me working in their research groups and encouraging me to apply for graduate schools. Thanks also to the undergraduate program advisor Dr. Susan Montgomery who helped me navigate my studies as an undergrad student.

Thanks to Breedveld group members, Dr. Lu Jiang, Dr. Won Tae Choi, Dr. Cornelia Rosu, Dr. Haisheng Lin, Dr. Fengyi Zhang, Dr. Nikhil Raj, Maritza Mujica and Sumner Dudick for listening to my problems and helping me whenever I needed. Many thanks to

Lu for helping me settling down in the group, Cornelia for the constant checking-in, answering questions about polymer chemistry and the holiday cards, Nikhil and Sumner for helping me get into the lab many times when I forgot my buzzcard, and Maritza for helping me with the SEM imaging and the rotary evaporator. I was very fortunate to have Kim Anh Pham in the lab for two years in her undergraduate, who worked patiently and meticulously on many measurements, thanks for her hard work. Thanks should also go to the graduate mentors in my undergraduate research groups, Dr. Sumit Bhatnagar, Dr. Liang Zhang, Dr. Cornelius Cilliers, Dr. Bruna Menezes and Dr. Ryan Hall who taught me numerous experimental techniques and research skills, and helped me get prepared for the graduate school.

I would also like to thank the former and current graduate students in the nanocellulose group at Georgia Tech, from who I learned so much about the nanocellulose materials in addition to their rheology. Many thanks to Dr. Bailey Risteen for helping me figure out where to purchase the cellulose nanomaterials, Dr. Nathan Ellebracht for answering questions about freeze drying and helping me become a leader of the group, Dr. Nikolay Semenikhin and Dr. Jeffery Luo for teaching me to do the TEMPO reaction and imaging the fibrils, and Dr. Cameron Irvin for sharing the details of making hydrogels.

Some measurements and processing of the materials in my research would not be possible without the help of many graduate students at Georgia Tech. I'd like to acknowledge the assistance of Dr. Chinmay Satam and Yue Ji for helping me numerous times homogenize lots of nanofibril suspensions which took quite a long time, Tola Okesanjo for assistance of the rotary evaporator and the homogenizer, Sujin Lee for setting

up the polarized microscope. Thanks to Tom Groseclose and Ronald Rondon for helping me with the floor centrifuge.

I wish to thank many friends who help me get through the difficult times of the graduate school. Many thanks to Jianyuan Zhai, Chaoyi Chang and Mingxuan Lu for listening to my frustrations and complains about the research and the job search. Thanks to Jianyuan for making the delicious food, taking me on numerous drives to the restaurants, grocery stores, yoga and dance studios, Chaoyi for sharing insights on classical music and going to the concerts and ballet performance together. Thanks to Xiangyun Lei and Yuan Yao for hosting dinners during the holidays. Thanks to Qishi Chen and Lijuan Zhang for encouraging me even though we are at different sides of the hemisphere.

I would like to thank my parents for their support of my decision to get a Ph.D. Mom and dad, thanks for nonetheless supporting the rebellious daughter who stubbornly tries to figure out her life. And finally, to Xiangyu Ni, for keeping me grounded and laughing through the difficult times; this would not have been possible without you.

TABLE OF CONTENTS

LIST OF TABLES

LIST OF FIGURES

LIST OF SYMBOLS AND ABBREVIATIONS

AFM	Atomic force microscopy
ChNF	Chitin nanofiber
CNC	Cellulose nanocrystal
CNF	Cellulose nanofibril
G'	Storage modulus
G''	Loss modulus
MW	Molecular weight
NA	Numerical aperture
PEG	Polyethylene glycol
POM	Polarized optical microscopy
PVA	Polyvinyl alcohol
RPM	Rounds per minute, the unit of rotational speed
SEM	Scanning electron microscope
TEM	Transmission electron microscopy
TEMPO	(2,2,6,6-tetramethylpiperidine-1-yl)oxyl
TEMPO-CNF	TEMPO oxidized cellulose nanofibril
wt%	Weight percentage, ratio of mass
$\dot{\gamma}$	Shear rate
η	Viscosity
$[\eta]$	Intrinsic viscosity
η_r	Relative viscosity
η_s	Specific viscosity

η_{sp}	Specific viscosity
η_0	Zero-shear viscosity
η_∞	High-shear viscosity
η_{water}	Water viscosity
λ	Characteristic timescale of the system (a parameter in the Cross model)
Ω	Rotational speed

SUMMARY

Demand for sustainable materials has increased in recent years as consumers and industry evaluate the environmental impact of their material usage. Cellulose nanomaterials (CNM), which utilize the nanoscale building blocks of natural cellulose, have emerged as promising sustainable materials that are produced from renewable sources, such as wood and plant materials. The uniquely high strength and low density of CNM make them promising candidates to replace petroleum-based materials in a wide range of applications such as rheological modifiers, composites and hydrogels. Despite having desirable properties and characteristics, the commercialization of CNM is hindered by its limited production capacity; a significant challenge for scale-up is the lack of robust, rapid and reliable quality control method to ensure product reproducibility and quality. In this thesis, we explore the use of rheology as a method to characterize cellulose nanomaterials. In addition to robust experimental protocols for rheological measurements, we develop rheological models and propose new parameters to bridge the gap between lab-scale measurements and industrial-scale quality control.

Detailed preparation and test protocols are developed to obtain reliable and reproducible rheological results for aqueous suspensions of cellulose nanocrystals (CNC) and TEMPO oxidized cellulose nanofibril (TEMPO-CNF), including more robust methods to determine sample concentration and check for shear hysteresis in viscosity measurement. Small changes in concentration, temperature and ionic strength affect the microstructures, and can be detected by rheological measurements.

To enable quick comparison between different flow curves without selectively picking viscosities at specific shear rates, we introduce a rheological model that combines the classical power law and Cross models: $\eta = a\dot{\gamma}^{-b} + \eta_\infty + \frac{\eta_0 - \eta_\infty}{1+(\lambda\dot{\gamma})^m}$, where $\dot{\gamma}$ is the shear rate and η the viscosity. The model accurately describes the flow curves across the full range of the shear rates we explored (0.01-1000 s^{-1}) and for all tested concentrations for both CNC (1.0-11.6 wt%) and TEMPO-CNF (0.20-2.40 wt%). Key model parameters correlate well with suspension concentration, and this model can thus be used to estimate the concentration of an uncharacterized CNM sample, which greatly reduces the testing time by performing a viscosity test compared to the conventional gravimetric oven-drying test. The model can also be used to estimate the salt concentration in a sample. Finally, the model was used to define a rheological 'flow index' parameter for TEMPO-CNF in the viscoelastic regime to describe and compare the effects of morphology and surface charge more effectively. Zero-shear viscosity η_0 is first determined from the Cross model, and the flow index k is defined through the scaling relation $\log_{10}(\eta_0) = k \cdot c - \log_{10}(\eta_{water})$, c being suspension concentration and η_{water} water viscosity. The flow index decreases with higher homogenization energy and higher surface charge, and is related to the fibril network structure. Moreover, the flow index of all homogenized samples collapse onto a single curve when plotted against cumulative homogenization energy, exhibiting a power law scaling. This flow index summarizes all viscosity information across multiple concentrations and the full range of shear rates into a single parameter, which can be used for quality control and/or benchmarking of cellulose nanomaterials, and which can guide the selection of optimum processing conditions.

Because research grade rheometers are not common in industrial environments, we explored extending the preparation and test protocols for viscosity measurements of CNC suspensions with a Brookfield viscometer. This spindle-type viscometer is commonly used for the industrial quality control. With proper sample mixing and data averaging protocols, we found that variations caused by using different spindles and sample-to-sample variations are small. Although the viscometer has a limited range of rotational speed and lacks sensitivity compared to more advanced research grade rheometer, it can still capture the flow curves at different concentrations (3.6-10.9 wt%). Flow curves with the characteristic three-regime shape could also be captured for samples at intermediate concentrations with nematic phases, and those flow curves can accurately be described by the combined model.

In addition to the quality control, the dewater/drying process is another key barrier to the commercialization of CNM materials. CNM materials are typically produced in aqueous suspension with high water content, which requires subsequent water removal step to reduce transportation cost or as a pre-processing step for applications such as rheological modifiers and composites. In this thesis, reverse dialysis is developed as an alternative dewatering method for CNM that avoids common dewatering issues like irreversible aggregation and sample heterogeneity. The redispersibility in a dewatering-redilution cycle is quantified by viscosity, and the redispersibility of the TEMPO-CNF dewatered via reverse dialysis is much better than via rotary evaporation. The method can also be applied to dewatering of CNC, chitin nanofiber and composites of polyvinyl alcohol (PVA) and TEMPO-CNF. Concentrated and well-dispersed PVA/TEMPO-CNF composite gels can be obtained at component concentrations that are difficult to achieve by other methods.

Reverse dialysis thus increases the processing range for these sustainable nanomaterials while preserving their beneficial morphological properties.

CHAPTER 1. INTRODUCTION

Demand for materials from sustainable and renewable resources has increased in recent years as consumers and industry evaluate the environmental impact of their material usage. [1] Cellulose is a class of sustainable materials that are produced from renewable sources, such as wood and plant materials. [2] Although traditional cellulose materials and their derivatives have been used extensively in the past for products like paper, cardboard, textiles, pharmaceuticals and consumables, these materials have limitations when competing with high performance materials like polymers and inorganic nanoparticles. [3] To bridge this gap, cellulose nanomaterials (CNMs), which utilize the nanoscale building blocks of natural cellulose, have emerged as promising materials. [4] The unique properties of CNM make it a promising candidate to replace petroleum-based materials in a wide range of applications. The CNM has high strength and low density, which can be used as additives in composites, hydrogels and aerogels to improve the mechanical properties. [5-8] Their high surface area-to-volume ratio enhance interactions with polymers and nanoparticles, which can be used to as rheological modifiers in food, drilling fluids and coatings. [9-13] Their negative surface charge and the hydroxyl groups enable charge interactions and hydrogen bonding to enhance barrier properties or as stabilizers in emulsions. [14-16] The hydroxyl group and large surface area also allow chemical functionalization for CNM to be used as catalysts, templates for flexible electronics and broaden their applicable ranges in films and composites. [17-20] The work presented in this thesis aims to expand the toolbox that characterize and process the cellulose nanomaterials in the manufacturing setting.

1.1 Structure, Properties and Production of Cellulose Nanomaterials

Cellulose nanomaterials (CNM) is a renewable and sustainable class of nanomaterials that are produced from abundant cellulose sources, such as wood and plant materials. [3] Cellulose is the essential component in plant cell walls and has hierarchical structures across multiple length scales, from fiber (mm scale), microfibril (μm) to nanofibril (nm). [3, 21] (**Figure 1.1**) Its basic chemical unit is a linear chain of D-glucose, which can be viewed as a high molecular weight polymer (n = 1000 - 1500).

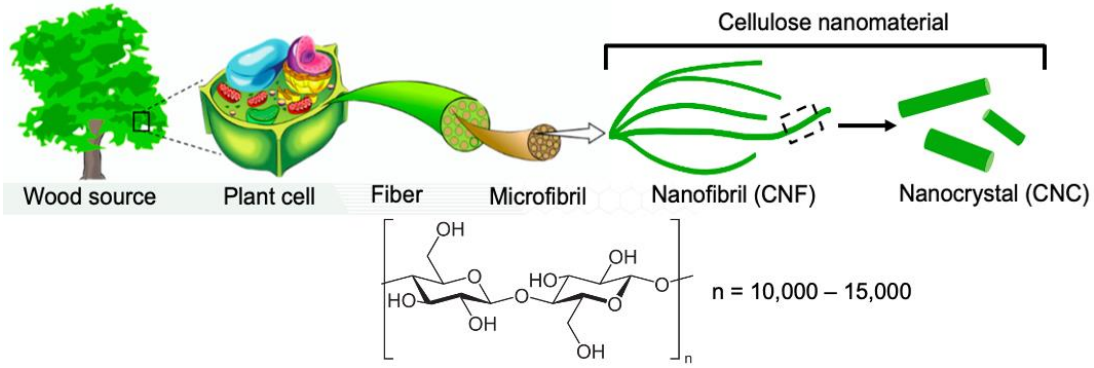

Figure 1.1 Hierarchical structure of the cellulose and the chemical structure of the basic unit of cellulose nanomaterial. The figure is partially reproduced from Miyashiro *et al.* [21]

The research on CNM in the past 20 years have explored and expanded the application areas in emulsions and dispersions, [22, 23] 3D printing, [24-26] energy storage and electronics, [27, 28] drug delivery, [29] tissue engineering, [30, 31] and functional materials. [32, 33] CNM offers high strength, large aspect particle ratio and low density, which is ideal for use as reinforcement materials in composites, films, hydrogels and fibers. [34-38] Moreover, the hydroxyl groups on the fibril surface facilitate surface modification or functionalization through chemistries that have been developed for other materials with reactive hydroxyl groups. The structure and properties of the cellulose nanomaterials,

together with their biodegradability, open up potential applications as rheological modifiers in coating, [39-41] food, [11, 42] cosmetics [43, 44] and pharmaceuticals, [45] and as barrier materials in packaging. [46-48] Three major types of the CNM are often used as the starting materials in research: nanocrystals, nanofibrils and oxidized nanofibrils. Their structure and properties are summarized in the following subsections.

1.1.1 Cellulose Nanocrystal (CNC)

Cellulose nanocrystals (CNCs) are rigid, rod-like colloidal particles, usually with length from 50 to 500 nm, width from 3 to 5 nm and aspect ratio of 15-100.[49] [50] (**Figure 1.2**) CNCs can be manufactured from diverse sources such as wood pulp, cotton, tunicate and bacterial cellulose. [51] The commercially available CNC materials are mostly produced from wood pulp using sulfuric acid hydrolysis, which introduces negatively charged sulfate ester group ($-OSO_3^-$) to the surface.[52, 53] The resulting negative surface charge provides good colloidal stability and dispersibility for CNCs in water.

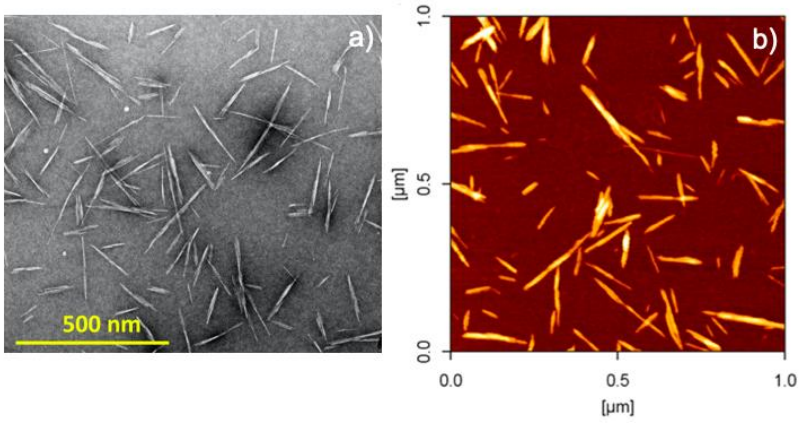

Figure 1.2 Microscopy images of CNC showing individual particles: a) TEM and b) AFM. The figures are reproduced from Jakubek *et al.* [49] This CNC was a National Research Council Canada-certified reference material (CNCD-1, (www.nrc.ca/crm)).

CNC suspensions in water are classified in different phases according to their concentrations. Although the exact threshold concentrations vary for different CNC materials depending on source and production method, in general, at low concentrations, CNC suspension are in the isotropic phase, where the particles are randomly oriented and distributed. [54] At higher concentrations, CNC particles self-assemble and form a chiral nematic (or cholesteric liquid-crystalline) phase. In this phase, the particles lack positional order at rest but possess some orientational order within layers, and the preferred direction rotates throughout layers forming a helical structure. [55] The preferred orientation is represented by a unit vector *n* called "director". [56] (**Figure 1.3a**) The director rotates sinusoidally when it moves along the helical axis *z*, where

$$n_x = \cos(q_0 \cdot z + \phi)$$

$$n_y = \sin(q_0 \cdot z + \phi)$$

$$n_z = 0$$

both *z* and ϕ values are arbitrary, and

$$p = 2\pi/q_0$$

where *p* is the chiral pitch, a common parameter to characterize chiral nematic phases. The pitch is often temperature sensitive. CNC suspensions in the chiral nematic phase show "fingerprint" texture when observed under the crossed-polarized microscopy. (**Figure 1.3b**) The distance between two adjacent fingerprint lines represents half of the chiral pitch, *p*/2.

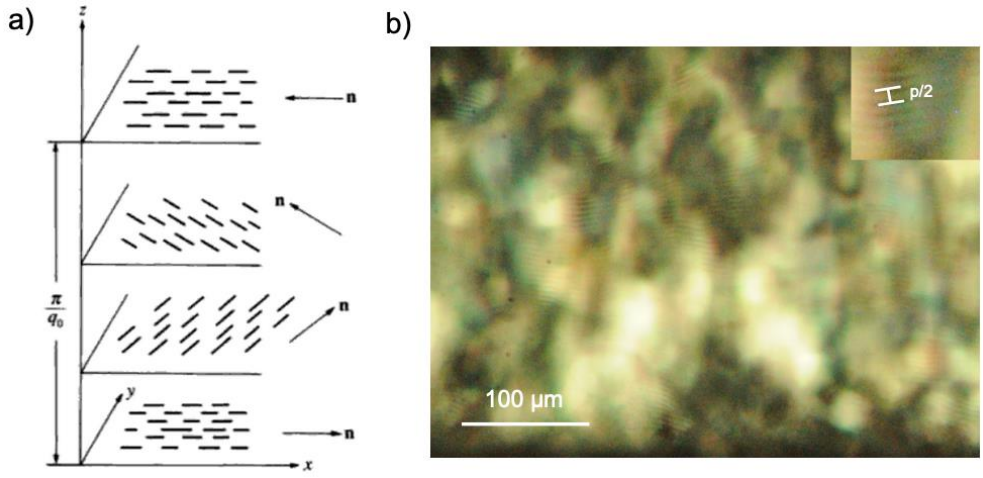

Figure 1.3 a) The arrangement of particles in the chiral nematic phase where the director n shows different orientational orders in layers along the z axis; [56] b) the polarized microscopy image of 7.7 wt% CNC showing birefringence and "fingerprint" texture.

A biphasic phase exists between the isotropic and chiral nematic phase that contains both phases. [54, 57] In a vial, the two phases tend to separate into an isotropic phase on top and chiral nematic phase at the bottom. [57, 58] The phase separation can be observed between cross polarizers. [55, 57] (**Figure 1.4a**) At concentrations higher than the chiral nematic phase, CNC suspensions are in a gel phase, where the "fingerprint" pattern is no longer visible. [57] (**Figure 1.4b**)

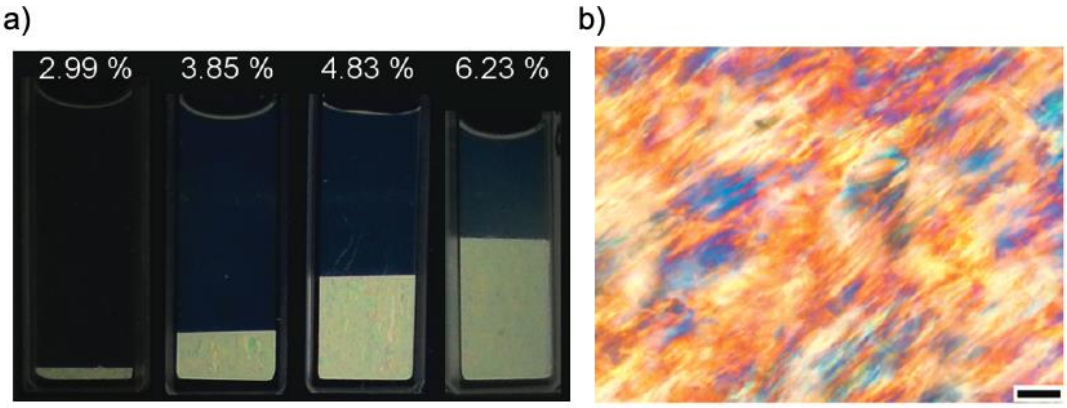

Figure 1.4 a) Suspensions of CNC in biphasic regime phase that are observed under cross polarizer; in a vial, the sample phase separates into isotropic phase (dark) on top and chiral nematic phase at the bottom (bright); [57] b) polarized microscope image of CNC in the gel phase showing no "fingerprint" texture. The scale bar is 50 µm. The figure is reproduced from Ureña-Benavides *et al*. [57]

1.1.2 Cellulose Nanofibril (CNF)

Cellulose nanofibrils are long flexible fibrils of length from 1 to 100 µm, width from 1 to 50 nm width and an aspect ratio of 100-2000. [3, 59] The fibrils are often aggregated and have large size variations as shown in the light microscope and the SEM images. (**Figure 1.5 and Figure A.1 in Appendix A**) There is not yet a clear criterion to differentiate between cellulose nanofibrils (CNFs) and cellulose microfibrils (CMFs). The CNFs used in some studies have similar morphologies as the CMFs used in some other studies. [60-62] The most recent classification by Isogai categorizes fibrils of 5-100 nm wide as cellulose nanonetworks that have heterogenous network structures such as fibril bundles and branches. [63] Fibrils of ~3 nm wide are categorized as cellulose nanofibril and are individually dispersed in water. According to this definition, the materials that are referred to as CNF in this thesis would fall in the category of cellulose nanonetwork.

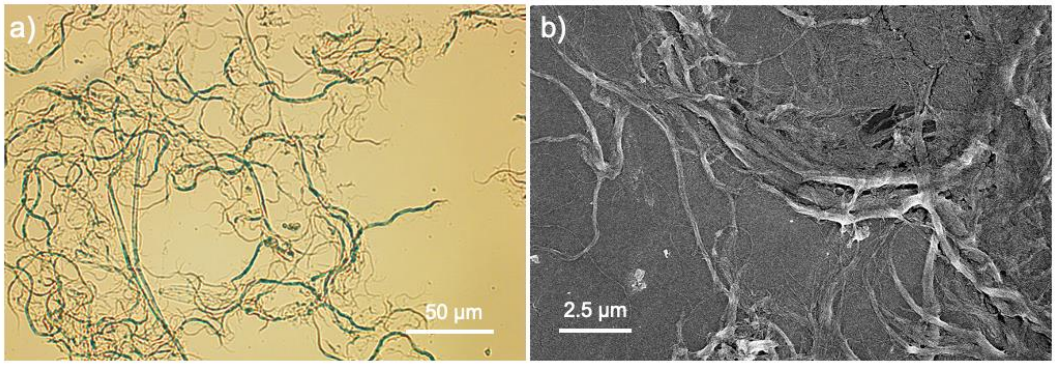

Figure 1.5 a) Light microscope and b) SEM images show that CNFs are aggregated and have large size variations.

CNF is manufactured by repeated mechanical processing such as high-pressure homogenization,[64] grinding,[59] refining [65] and twin-screw extrusion [66, 67] to fibrillate and isolate the fibrils from thick cellulose fiber bundles. A filtration step is usually applied to remove large unfibrillated or partially fibrillated fibrils to achieve more homogenous fibril sizes. [59] The surface charge of CNF is relatively low. Therefore, aqueous CNF suspensions are usually flocculated, which can be observed visually. (**Figure 1.6 (a) and (b)**)

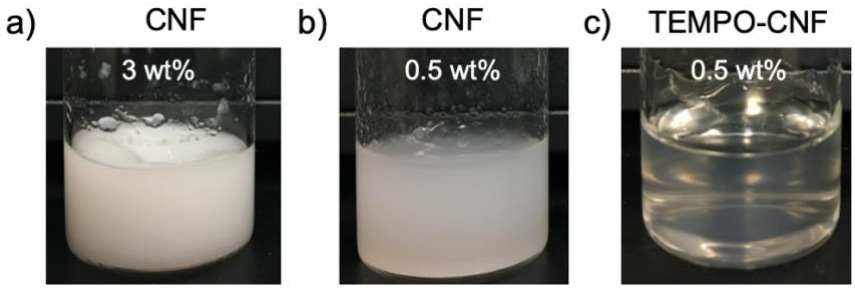

Figure 1.6 CNF materials used in this thesis; aqueous suspensions of CNF at a) 3 wt% and b) 0.5 wt%, showing significant levels of flocculation, and c) a clear 0.5 wt% TEMPO-CNF suspension with negative fibril surface charges to improve fibril dispersion, reduce flocculation and enhance transparency.

1.1.3 TEMPO-mediated Oxidation Cellulose Nanofibril (TEMPO-CNF)

Chemical or enzymatic pretreatment is essential to further fibrillate cellulose bundles to obtain individually dispersed fibrils.[68] TEMPO ((2,2,6,6-tetramethylpiperidine-1-yl)oxyl) mediated oxidation is one of the most common chemical treatments, which selectively oxidizes C6 hydroxyl groups to carboxylate groups.[69, 70] (**Figure 1.7**) Negative charges are thus introduced on the fiber surface, helping to repel and stabilize fibrils in suspension when they are separated from fiber bundles through subsequent mechanical refining, such as blending or high-pressure homogenization. [70] In combination with the mechanical treatment, TEMPO pre-treatment results in fibrils with smaller sizes and narrower size distributions: width from 3 to 5 nm, length from 0.5 to 10 μm and aspect ratio from 300 to 1000. [63] Moreover, the fibrils are individually dispersed, where the suspension is transparent without apparent aggregations. (**Figure 1.6c**) The fibrillated TEMPO-CNF suspension is stable without phase separation if rest for long period. Other common chemical pretreatments used in the literature studies include carboxymethylation, [71] carboxyethylation, [72] phosphorylation [73] and periodate oxidation. [74] The pretreatments also introduce charges on fibril surfaces to stabilize the suspensions with subsequent fibrillation processing. [75]

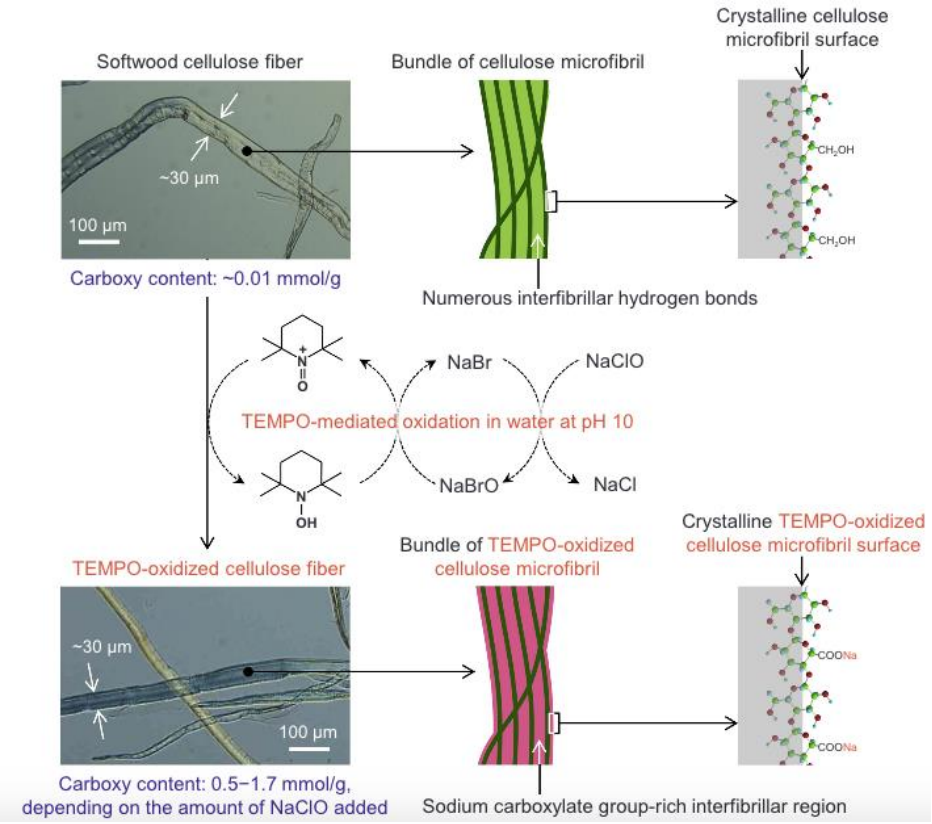

Figure 1.7 a) TEMPO mediated oxidation selectively oxidizes C6 hydroxyl groups to carboxylate groups while retains the original fibril morphology. The figure is reproduced from Isogai *et al.* [76]

The surface charge of TEMPO-CNF is measured via conductometric titration, and is quantified in terms of the carboxyl content (mmol per gram of dry TEMPO-CNF). [77] Since -COOH is a weak acid, the protocol is to first add around 2 ml of 0.1M NaOH solution to fully deprotonate the dilute TEMPO-CNF suspension. The modified procedure based on the Foster *et al*. [77] is using TEMPO-CNF suspension of 0.6 to 1 mg/ml with a total volume of 200 ml. Then, 0.1M of HCl titration solution is added at 100 µl each time while simultaneously tracking the pH and conductivity, until the pH drops below 4.5. (**Figure 1.8**) The conductivity curve exhibits two equivalent points, which are the two intersection points determined by linear fitting three parts of the conductivity curve. The difference between the two points is the HCl volume which is used to calculate the total

moles of HCl (usually in unit of mmol) in the titration. The amount of dry TEMPO-CNF is determined from the volume and concentration of its dilute suspension, and the carboxyl content of TEMPO-CNF is determined by dividing the total moles of HCl by the dry amount of TEMPO-CNF.

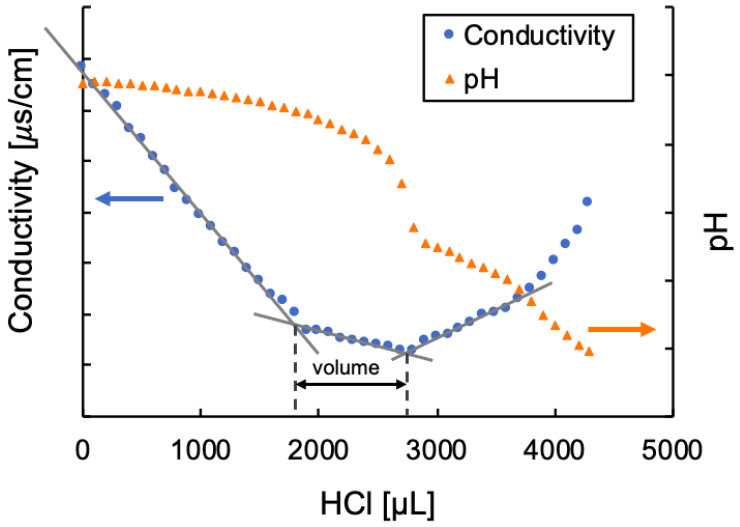

Figure 1.8 Illustration of surface charge determination via conductometric titration of a representative TEMPO-CNF suspension with conductivity and pH data and the fitted lines to guide determining the intersection points.

A summary of the properties of CNC, CNF and TEMPO-CNF materials used in this thesis is presented in **Table 1-1**. As the properties of cellulose nanomaterials vary significantly even when using the same sources and processing conditions, it is important to specify the size and surface properties for each nanomaterial. Batch number information of a commercial product should also be included if available.

Table 1-1 Summary of the properties and the supplier for the cellulose nanomaterials used for the studies described in this thesis.

	CNF	TEMPO-CNF	CNC
Type	Fibrils		Colloidal nanoparticles
Manufacturing	Mechanical	Chemical + Mechanical	Chemical
Length	1 - 100 μm	1 - 5 μm	50 - 500 nm
Width	5 - 50 nm	3 - 10 nm	3 - 5 nm
Aspect ratio	100 - 2000	300 - 1000	15 - 100
Surface charge	/	Negative	Negative
Supplier	University of Maine, the process development center (https://umaine.edu/pdc/nanocellulose/)		

1.2 Challenges of Quality Control in Cellulose Nanomaterials Manufacturing

Despite having desirable properties and characteristics, cellulose nanomaterial (CNM) production capacity is still limited, which hinders further advancement and commercialization. In 2017, the daily production capacity of all companies that produce at full scale was 1.8 ton for cellulose nanocrystal (CNC), 4.3 ton for cellulose nanofibril (CNF) and 31.6 ton for cellulose microfibril (CMF), which is much less than the potential demand for applications across industries - estimated to be around 64,000 ton. Though the projected number may be overly optimistic, scale-up of the current production is clearly needed. [78-80]

A key challenge to scale up the production is that CNM materials suffer from large variations in properties even when the manufacturing process is carried out under nominally the same reaction condition. [52, 81] To expand the production capacity to industrially relevant scales and to ensure production of CNM at consistent quality, one of the most urgent issues to be addressed is the lack of standardized, rapid and reliable

characterization methods for quality control during the manufacturing process. [49, 82] Current characterization techniques, such as electron microscopy and light scattering, are time-consuming in terms of sample preparation and imaging processing, and cannot easily be integrated into an industrial manufacturing process for online monitoring. [49, 81] Moreover, these methods suffer from potential bias because they only probe a small portion of the CNM sample; as a result, they can misrepresent the sample's bulk properties. Thus, a robust, rapid and accurate characterization method is needed for the quality control of these nanomaterials in manufacturing.

1.3 Challenges of Dewatering the Cellulose Nanomaterials

Cellulose nanomaterials are all first produced as aqueous suspensions at low concentrations, because they have low gelation concentrations (1-3 wt% for CNF, 10 wt% for CNC) due to their high aspect ratio, and some key processing steps, such as fibrillation through pressure homogenization, cannot be performed at higher concentrations. [63, 83] Subsequent dewatering or drying is therefore necessary to increase the suspension concentrations to reduce transportation costs, or to be used in applications that require higher concentrations of the nanomaterials. In fact, the dewatering/drying process has been identified as a key barrier to successful commercialization of the cellulose nanomaterials. [84]

A challenge in dewatering or drying of these nanomaterials is the redispersibility. The most common techniques remove water through air-liquid phase transport: evaporation, freeze-drying and spray-drying. [83, 85, 86] These techniques are known to cause aggregation, especially for cellulose nanofibrils, because of the presence of hydroxyl

groups on the fibril surface to form hydrogen bonds. [87, 88] The aggregates are often irreversible and persist when the material is redispersed, thus greatly reducing the benefit of large surface area of these nanomaterials. Fully redispersion of the cellulose nanofibrils from their dewatered or dried form is challenging, often requiring extensive mechanical forces such as sonication and high shear mixing for a long time. [89-91] Some studies have tried to improve redispersion by using additives to stabilize the electrostatic charges [92, 93] or by modifying the surface chemistry of the fibrils before dewatering or drying. [88, 94] Nevertheless, such mechanical and chemical treatments will likely change the morphology or the chemical composition, which is not ideal for reprocessing the nanofibrils and incorporating them, for example, into polymer composites. Overall, there lacks a dewatering method that can retain the nanomaterial's redispersibility without changing its morphology and surface charge and without introducing extra additives.

1.4 Overview of the Thesis

The goals of this thesis are to develop rheological test protocols and models for quality control of the cellulose nanomaterials (CNM), and to provide improved understanding of dewatering and redispersion of CNM through rheological characterization. Chapter 2 summarizes the literature findings of rheological characterizations and models for CNM, with a focus on viscosity measurements and basic oscillatory rheology as a function of key parameters like concentration, ionic strength and temperature. Chapter 3 develops preparation and test protocols to obtain reliable and accurate rheological results at relevant processing conditions and investigates the processing-structure-property relationships for CNM. Chapter 4 develops a rheological model that accurately describes the flow curves of CNC and TEMPO-CNF across

concentrations and shear rates, which can be used to quickly estimate the concentration of an uncharacterized sample. A rheological parameter is also developed to capture the effect of morphology and surface charge of the TEMPO-CNF. Chapter 5 extends the preparation and test protocols for viscosity measurements of CNC suspensions using an industrial-grade viscometer to characterize flow curves at different concentrations. The variability of the flow curves and effect of mixing are investigated. Chapter 6 presents a dewatering method to obtain concentrated cellulose nanomaterial without compromising redispersibility, and to create polymer composite gels with well-dispersed nanocelluloses at concentrations that are otherwise hard to achieve. The homogeneity and redispersibility of the dewatered materials are characterized by rheology. Chapter 7 summarizes the major findings of this thesis and provides recommendations for future research.

CHAPTER 2. LITERATURE REVIEW OF RHEOLOGICAL CHARACTERIZATION OF CELLULOSE NANOMATERIALS

Rheology studies the deformation and flow of the materials. It provides information on how "fluid-like" or "solid-like" materials are, which are characteristics that depend on measurement timescale. The rheological behavior of materials reflects their microstructure and structural changes under different conditions. This chapter reviews the literature on rheological characterization and modeling of cellulose nanocrystal (CNC), cellulose nanofibril (CNF) and TEMPO-cellulose nanofibril (TEMPO-CNF), summarizing the current understanding of process-structure-property relations for cellulose nanomaterials (CNM) with a focus on the effect of conditions and processing parameters relevant in manufacturing processes.

2.1 Rheological Characterization and Modeling of Cellulose Nanocrystal

2.1.1 Flow Curves at Different Concentrations

The shear rheology (viscosity as a function of shear rate) of aqueous cellulose nanocrystal (CNC) suspensions has been studied as function of CNC concentration, including concentration related phase change. In general, as one would expect, the viscosity increases with concentration. [54, 57, 95] The flow curves of CNC across concentrations are generally categorized into three groups. **(Figure 2.1)** At high concentrations, the viscosity decreases continuously with increasing shear rate, showing a single shear thinning behavior, and these samples are in the gel phase. [95] This is also confirmed by the frequency sweep, where G' is larger than G''. At intermediate CNC concentrations, the

flow curves first show shear thinning at lower shear rates, followed by a viscosity plateau region at intermediate shear rates, and another shear thinning region at high shear rates. For these concentrations, fingerprint textures can be observed using polarized optical microscopy (POM), indicates that the samples are in the liquid crystalline phase. [57]

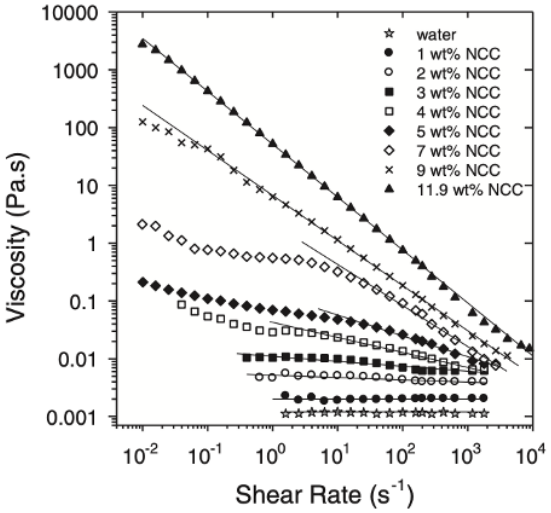

Figure 2.1 The flow curves of cellulose nanocrystal (CNC) across concentrations from isotropic phase, liquid crystalline phase to gel phase. The figure is reproduced from Xu *et al.* [95]

Using a rheometer coupled with POM imaging, Shafiei-Sabet *et al.* proposed that the first shear thinning region is related to the breakdown of aggregated domains, which contain clusters of CNC nanoparticles. [54, 57] **(Figure 2.2)** In the plateau region, the domains align in the flow direction. The unchanged viscosity indicates that the external shear force is not strong enough to break down individual domains. The viscosity decreases again in the second shear thinning region as larger shear forces are able to break down individual nanoparticles and align them in the flow direction. This three-region flow curve has also been observed for liquid crystalline polymers, such as hydroxypropyl cellulose. [96-98] Frequency sweeps of the samples at these intermediate concentrations show that

these are viscoelastic fluids, with $G'' > G'$, but with G' still being detectable, indicating that the sample has some elasticity. [95]

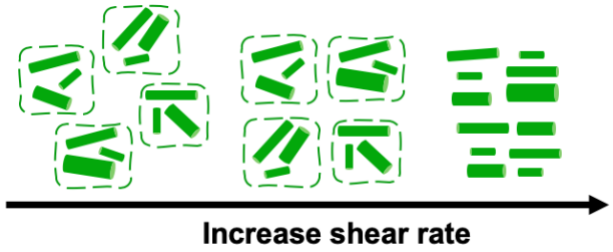

Figure 2.2 The alignment of domains and nanoparticles when the CNC suspension under continuous shear. The first shear thinning regime of the flow curve is due to breakdown of domains, and the second shear thinning regime is because of the breakdown of individual nanoparticles.

At low concentrations, the viscosity is constant across most of the shear rates, exhibiting Newtonian behavior. The samples of these concentrations appear dark under POM and are thus classified as isotropic phase. [54, 99] The variations in viscosity are found to be small. Haywood *et al.* found that the viscosity points at lower shear rates have larger variations, as well as the points in the transition regime (liquid crystalline to gel and isotropic to liquid crystalline), likely because of the microstructural changes in the phase transition. [100]

Nevertheless, not all studies report well-defined three-region flow curves when studying CNC suspensions across the whole range of concentrations. In some studies, the flow curves change from single shear thinning (power law) behavior directly to Newtonian fluid behavior when decreasing concentrations. [101, 102] Some studies report flow curves with three regions, but the slope of the first shear thinning is very small, making that region hard to discern. [103, 104] Other studies report a strong shear thinning at low shear rates, but the slope of the shear thinning (viscosity versus shear rate) is larger than 1, which is a

rheological anomaly for steady state measurements of homogeneous is samples. [105, 106] This may result from incorrect loading or insufficient pre-shear, so that the sample inside the measuring system is not homogenous.

The CNC suspensions were found to disobey the empirical Cox-Merz rule at intermediate concentrations in the liquid crystalline phase, which is also a common characteristic for polymers in the lyotropic liquid crystalline phase. [57, 107] The complex viscosity η^* is more than 10 times larger than the shear viscosity η. At lower concentrations, even though η^* and η do not overlap, the difference is much smaller, and η^* is only slightly larger. [108, 109]

2.1.2 Mixing Methods

Commercial CNC products are available in two forms: slurry and dried powder. [80] To prepare CNC at various concentrations, mixing the stock with water is needed, which is a critical step to ensure good dispersion and measurement reproducibility. [110] For dried CNC powders, which are heavily aggregated, sonication is recommended to effectively disperse the particles. [77] Shafiei-Sabet *et al.* investigated the effect of total sonication energy (0 to 5000 J/g) that was applied to disperse CNC suspensions on suspension rheology. [54] The first 1000 J/g of sonication energy significantly reduces the viscosity, but the viscosity levels off as the energy input is increased further. Moreover, the flow curve shows a single shear thinning regime without sonication, whereas it shows the characteristic shape of three-region behavior after 1000 J/g or more of sonication energy is applied, indicating that some aggregates are broken down. (**Figure 2.3**) Nevertheless, the size of the primary CNC particles does not change according to

observations with TEM. Beck *et al*. also find that 5000 J/g sonication energy is insufficient to break the covalent sulfate bond of CNC. [111]

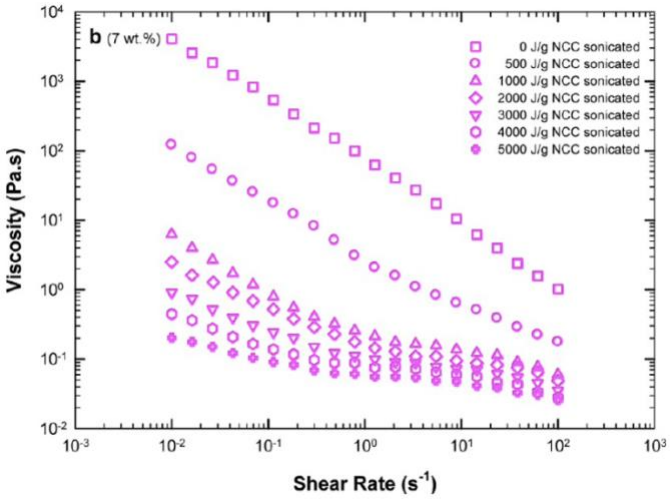

Figure 2.3 The flow curves for 7 wt% CNC suspensions sonicated at different energy levels. The viscosity decreases significantly after 1000 J/g sonication and levels off at higher sonication levels. The figure is reproduced from Shafiei-Sabet *et al.* [54]

However, sonication does affect the electrostatic interactions between CNC particles. Both zeta-potential and conductivity have been found to increase with increasing sonication energy. [54] Moreover, polarized optical microscopy of CNC sonicated at 2000 J/g shows that both the size of liquid crystalline domain and the pitch size increased compared to control samples without homogenization. [54] Sonication likely liberates excess ions trapped in the bound layer of CNC particles, expanding its electronic double layer, thus changing the electrostatic interactions among the particles. Another problem is unclear justification of a proper sonication energy for dispersing samples. Shafiei-Sabet *et al*. use 1000 J/g as this energy level sufficiently breaks down the aggregates, and further energy input does not make much difference as suggested by the similar values of viscosity and the hydrodynamic radius. [54] Jakubek *et al*. choose a sonication energy of 4850 J/g

for the same reason, and these authors mention that similar hydrodynamic radius could be obtained, which is an indication of reproducible redispersibility. [49] On the other hand, Beck *et al*. argued that using the same total energy input to sonicate samples at different concentrations may not lead to the same level of dispersion. [111] In their study, the average particle size and size distribution varied with the sample concentration, even when the same sonication energy was applied. Beuguel *et al*. suggested that the power level and not just total energy, also affects dispersion. [109] They found that an aqueous suspension of dried CNC powder that was sonicated at 50 W had a much lower viscosity than when the suspension was sonicated at 10 W, even though the total energy was kept constant.

For slurry, sonication is also found to greatly reduce the suspension viscosity. Gicquel *et al*. reported that the phase separation of the sonicated sample phase happens much faster, and it has a narrower biphasic range. [112] These observations indicate that sonication notably changes the existing microstructure. Therefore, some studies prefer to use mechanical shearing such as vortex mixing or homogenization (Ultraturax disperser) for mixing in order to preserve the microstructure of the samples prepared from slurries. [95, 112]

2.1.3 Modeling and Aspect Ratio Estimation

Using rheological models to describe the flow curves of CNC suspensions has been investigated in several previous studies. Lu *et al*. fit the flow curves using the power law model, (Equation 2-1) where k is the flow consistency index and m is the power law index. [101, 113] Larger m values indicate stronger shear thinning and thus more prevalent inter-particle association. The index m has been found to follow a power law scaling with CNC

volume fraction (and therefore weight fraction), although both *m* and the volume fraction span less than one decade.

$$\eta = k\dot{\gamma}^{-m} \tag{2-1}$$

The Carreau model (Equation 2-2) has also been used to fit flow curves and to extract the zero-shear viscosity η_0; [101] the value of η_0 increases slowly at lower volume fractions ϕ where suspensions are essentially Newtonian liquids, while it increases sharply at higher volume fraction ϕ when suspensions transition to the gel phase. η_∞ is the viscosity at infinite shear rate; λ is the relaxation time and both *n* and *m* control the viscosity in the shear thinning regime.

$$\eta = \eta_\infty + \frac{\eta_0 - \eta_\infty}{(1+(\lambda\dot{\gamma})^n)^m} \tag{2-2}$$

Neither model can accurately capture the flow curves at all concentrations. The power law model can fit the flow curves at high concentrations that have a single shear thinning behavior. The Carreau model, on the other hand, captures the flow curves at lower concentrations, where the viscosity transitions between plateaus at low and high shear rates via shear thinning. Neither of these models is able to describe the flow curves at intermediate concentrations where the viscosity exhibits shear thinning at low shear rates, followed by a plateau, and then another shear thinning regime.

Xu *et al*. and Gicquel *et al*. use the power law model to fit the whole flow curves at high concentrations, and fit the shear thinning region of the flow curves at lower concentrations. [95, 112] (see, for example the fit lines in **Figure 2.1**) Although the model is able to locally capture the behavior of the viscosity, selection of the data points to use

for fitting seems arbitrary and no thorough justification is provided by the authors. Overall, there currently is not a rheological model that can describe the full flow curves across concentrations and across shear rates.

In addition to using rheological models to fit the flow curves, viscosity measurements have been used to estimate the aspect ratio (length/width) of the CNC particles. Although there are several correlations to estimate the aspect ratio (*f*) of rigid rod-like particle from the intrinsic viscosity [η], [114, 115] previous studies have predominantly used the Simha equation [116] (Equation 2-3), where λ is the particle shape coefficient, λ = 1.8 for cylindrical rods and λ = 1.5 for ellipsoid rods. [115]

$$[\eta] = \frac{f^2}{15(ln2f-\lambda)} + \frac{f^2}{5(ln2f-\lambda+1)} + \frac{14}{15} \tag{2-3}$$

The intrinsic viscosity $[\eta]$ is estimated from the relative viscosity η_r, which is measured viscosity η divided by solvent viscosity η_s. Boluk *et al.* estimated [η] using Fedors' equation, (Equation 2-4) where η is measured by Ubbelohde capillary viscometer, *c* the concentration and c_m the maximum packing concentration of the particles. [117, 118]

$$\frac{1}{2(\sqrt{\eta_r}-1)} = \frac{1}{c[\eta]} - \frac{1}{c_m[\eta]} \tag{2-4}$$

Moreover, as CNC is negatively charged, it forms an electrostatic double layer, which affects the estimation of true particle size. [119] To approximate the true particle size, salt is added to the CNC suspension to compress the double layer and the corresponding *[η]* is measured. However, as the neutral rigid rod-like body is unlikely to reach, Boluk *et al.* used the *[η]* of particles having 1 nm double layer thickness as characterized by the inverse of the Debye screening length κ^{-1}, [118] which is then used to estimate the aspect ratio.

Though Fedors' model takes into account the primary electroviscous effect, its validity for CNC suspensions is questionable because c_m may become negative at certain ionic strengths, which is physically impossible. [115]

Other correlations such as the Huggins equation and Kraemer equation have been used to estimate $[\eta]$ from η_r. [120] However, the validity of the Huggins equation for CNC is also still questionable. In previous work, the extracted Huggins parameters for three CNC samples of different morphologies were 0.556, 0.308, and 0.27, which fall outside the theoretical range of parameters in good solvent (0.25-0.5) or for rod-like particles (>0.4). [121, 122] In addition, the authors chose to use the viscosity at 1000 s^{-1} to determine the η_r, which is outside the Ubbelohde viscometer range of 300-600 s^{-1}. [115, 119] As CNC is shear thinning at high shear rates, the choice of shear matters in this regime, further complicating the estimation analysis.

2.1.4 Temperature Effects

Two temperature ranges are mostly studied in the literature: 110-150 ºC for investigation of the thermal stability of CNC, and 10-50 ºC for understanding the viscosity behavior and the underlying microstructure of suspensions. CNC can be used as rheological modifier for drilling fluids in enhanced oil recovery, thus understanding the thermal stability at high temperatures is important. [123, 124] CNC was found to start degrading at 110 ºC. From the quality control perspective, the temperature should be less than 110 ºC when determine the CNC concentration by oven drying to avoid degradation. [125]

For the studies on the temperature influence on suspension rheology in the range of 10-50 ºC, at low concentrations (isotropic phase) the flow curves were found to decrease

with increasing temperature; at high concentrations (gel phase), the viscosity stayed in essence the same as temperature increased. [54] At intermediate concentrations (biphasic and liquid crystalline phase), the viscosity first decreases until around 30 ºC, then increases at 50 ºC. Microstructural changes at elevated temperatures have also been observed. Using polarized optical microscopy (POM) imaging, Pan *et al*. found that higher temperatures led to more packed chiral nematic domains and larger pitch size, [126] and Shafiei-Sabet *et al*. reported that the size of the fingerprint region decreased, indicating a reduction of liquid crystalline phase. [54, 57] These changes are not profound, but the underlying reason for the non-monotonic change in viscosity and microstructure at intermediate CNC concentrations is still unclear. Xu *et al*. suggested that the viscosity increase was caused by the melting of the liquid crystalline phase at higher temperatures. [127] Yet, this hypothesis has not been confirmed by POM imaging. Studies on aqueous solutions of hydroxypropyl cellulose, a cellulose derivative that has been widely used as a model system to study the polymer liquid crystalline behaviors, also found temperature dependent viscosity and microstructures. [128] The viscosity decreases as temperature goes up from 5 to 15 ºC, then starts to increase from 15 to 30 ºC. Viscosity data at 5, 20 and 35 ºC collapse into a single master curve when plotted versus shear stress. Using POM imaging, the isotropic region was found to grow relative to the surrounding liquid crystalline region. [129]

2.1.5 Ionic Strength Effects

Because the CNC nanoparticles have negative surface charges, changes in electrostatic interactions will change the microstructures of the suspensions. [130, 131] The ionic strength (I) can be modulated by adding salt, which is calculated as Equation 2-5, where c is the salt concentration and z is the valency of the ions.

$$I = \frac{1}{2}\sum_{i=1}^{n} c_i z_i^2 \quad (2\text{-}5)$$

For example, the ionic strength of a 1 mM Na_2SO_4 solution is $\frac{1}{2}(2(1)^2 + 1(2)^2) = 3$ mM. [132]

Shafiei-Sabet *et al.* investigated the effect of adding 0-15 mM NaCl to CNC suspensions of a wide concentration range. [133] At low concentrations (isotropic phase), adding salt leads to viscosity decrease, as the electroviscous effect is weakened. At intermediate (liquid crystalline phase) and high (gel phase) concentrations, the viscosity first decreases then increases because of aggregation. Cherhal *et al.* characterized the aggregation process using small-angle neutron scattering (SANS) and found that the aggregation process happened as soon as the salt was added. [134] The process also restarts as soon as the system is at rest, even if the aggregation process is disrupted. Moreover, the viscosity change is sensitive to the salt concentration, but weakly dependent on CNC concentration. [135] The nanoparticles also aggregate faster at higher temperatures due to increased hydrophobic interactions. In addition to NaCl, Phan-Xuan *et al.* studied the influence of adding mono-, di- and tri-valent salts. [136] At the same salt concentration, the higher valence salt leads to a lower gelation concentration due to higher degree of aggregation. Among the monovalent salt, the smaller the ion size, the larger the gelation concentration.

Beck *et al.* added salt to both the as-received CNC and the dialyzed CNC, and compared their viscosity change. [137] The dialyzed CNC is the same as the as-produced CNC except that it is dialyzed against water to remove residual salts. The dialyzed CNC

has a much higher viscosity initially, and its viscosity decreases significantly after the salt is added. (**Figure 2.4**) After 5 mM ionic strength, the two viscosity curves overlap.

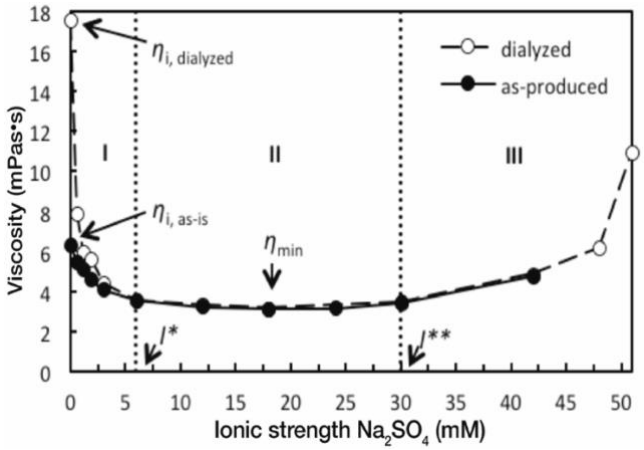

Figure 2.4 Viscosity of as-produced and dialyzed CNC suspension as a function of ionic strength. The CNC in this figure is in acid form, which is different from the CNC in the neutral sodium form used in this thesis. The figure is reproduced from Beck *et al.* [137]

Bertsch *et al*. performed an in-depth study to understand the microstructural changes caused by adding salt. [138] As CNCs are charged rod-like particles, salt screens the charges resulting in electrostatic interactions with shorter range. Adding salt first decreases the viscosity, G' and G'' due to compression of the electron double layers, then increases the viscosity due to intermolecular attraction and the resulting formation of aggregates. (**Figure 2.5**)

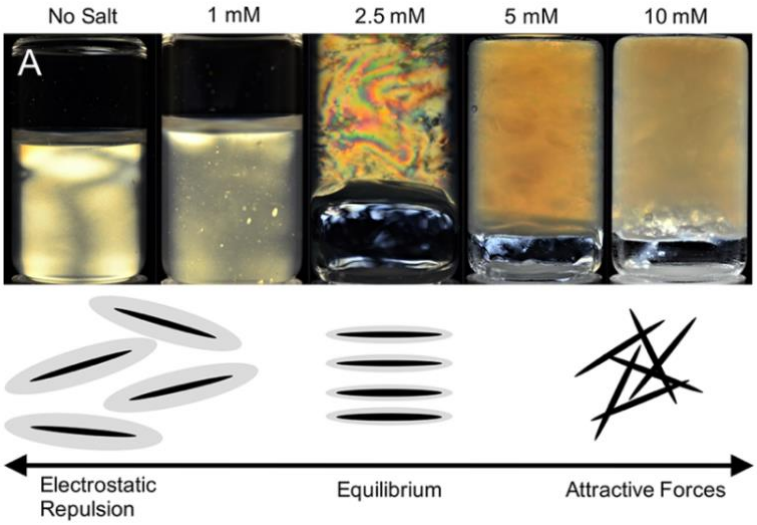

Figure 2.5 4 wt% CNC suspensions with different $CaCl_2$ concentrations imaged between cross-polarizer that shows phase change. The illustration shows the aggregation mechanism, where the rod is CNC particle (black) surrounded by electron double layer (grey). The figure is reproduced from Bertsch *et al.* [138]

Phase diagrams have been developed for CNC at different salt and pH conditions. Li *et al*. developed a phase diagram as a function of CNC concentration and pH, which showed regions of isotropic, chiral nematic and nematic phases characterized by the polarized optical microscope. [139] A series of studies by Xu el al. comprehensively investigated the rheological behavior of salt-added CNC suspensions. The first phase diagram as a function of CNC and salt concentrations was identified via rheology and was classified into five phases: liquid, viscoelastic, repulsive glass, attractive glass and gel. [140] The follow-up study provided more details about the viscoelastic regime by using both rheology and POM characterization, and identified a new phase: liquid crystalline hydroglass. [141, 142] These phases are summarized in a generalized phase diagram, together with the data points from previous studies plotted on the phase boundary. [143] (**Figure 2.6**) The generalization of CNCs from different labs and sources into one phase diagram indicates that salt concentrations and interparticle forces dominantly determine

the phase behavior, regardless of the source, size and the surface charge of the CNC. The generalized phase diagram helps accelerate the application development of CNC in some newly identified phases. For example, Bertsch *et al*. found that CNC suspensions in the attractive glass phase had mechanical properties similar to gels, while still retaining the optical properties of the nematic domains, which provides opportunities to produce flexible and optically active CNC-based materials. [144]

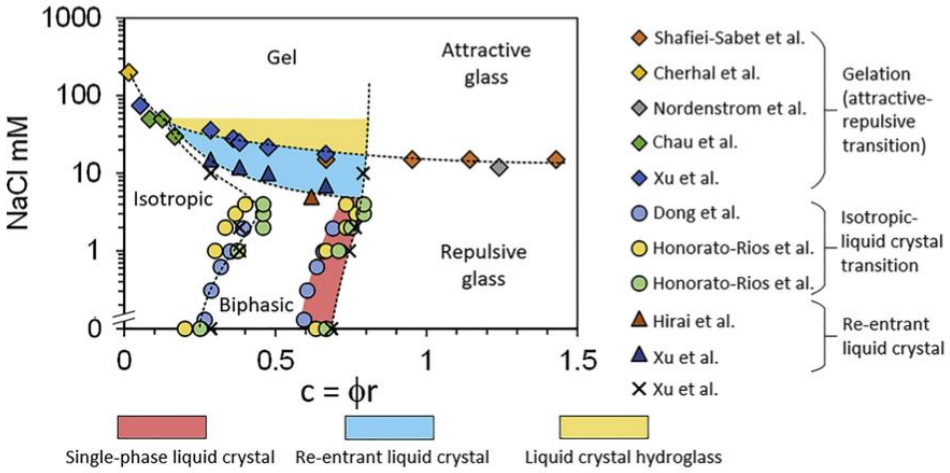

Figure 2.6 The generalized phase diagram for CNC suspensions as a function of NaCl concentration and dimensionless CNC concentration. The figure is reproduced from Xu *et al.* [143]

2.2 Rheological Characterization of Cellulose Nanofibril

Of the most commonly studied CNMs, cellulose nanofibril (CNF) poses the biggest challenges for rheological characterization due to the large fibril sizes and heterogenous networks. The CNM materials discussed in this section also include TEMPO and enzymatically pretreated CNF that are not effectively fibrillated, showing similar rheological behaviors as the mechanically refined CNF. The occurrence of flow instabilities is a key concern during shear viscosity measurements. Wall-slip, heterogenous

flow and shear banding are among the most-raised issues that can affect experiments. Nechyporchuk *et al*. detected the wall-slip of TEMPO-CNF suspensions under steady shear by visualizing the 2D flow pattern at the surface using a TiO_2 filament to create white contrast on the suspension surface captured by CCD camera, [145] which shows up as a white margin at the interface of the suspension and the rotating shaft. Wall-slip has been found in cone-plate and Couette geometries with both smooth and roughened surface at low shear rates. Though it is less apparent when using the roughened plate, some undeformed area still exist. The vane geometry can avoid wall-slip at low shear rates, but it exerts insufficient force to shear the whole suspension. [146] Shear stress as a function of shear rate can also indicate the existence of wall-slip, if a sudden drop in shear stress is found at low shear rates. [145, 147] (**Figure 2.7**) Wall-slip has also been observed in soft particle systems and foams by monitoring shear stress at low shear rates. [148, 149] A good protocol for assessing wall-slip is to measure shear stress as a function of shear rate using different geometries. If the shear stress curves show no sudden drop at low shear rates and the curves measured using different geometries overlap, concerns about potential wall-slip are alleviated.

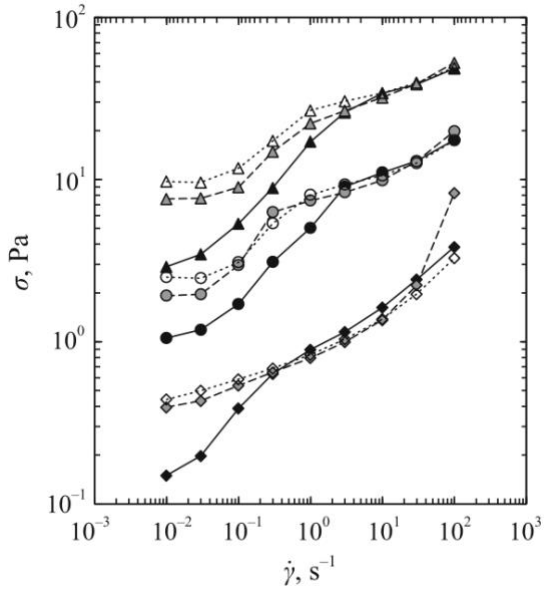

Figure 2.7 The shear stress as a function of shear rate measured using different geometries for TEMPO-CNF suspensions at 0.5 wt% (diamonds); 1.0 wt% (circles) and 1.5 wt% (triangles): roughened Couette (empty symbols), vane geometry (half-filled symbols) and smooth Couette geometries (filled symbols). The stress drop at lower shear rates indicates the presence of wall-slip. The figure is reproduced from Nechyporchuk *et al.* [145]

While wall-slip can be observed via rheology, shear banding is not effectively reflected in the viscosity or shear stress curves, and flow visualization is needed. Nechyporchuk *et al.* again used TiO_2 to visualize the 2D flow of CNF/CMF suspensions. [150] Shear banding was found to occur at intermediate shear rates. Regimes of different flow speed exist, where the suspension closer to the outer cylinder of a Couette geometry is more stagnant. At higher suspension concentrations, where the interactive forces between the fibrils are larger compared to the shear force, the shear banding shifts to higher shear rates.

Nazari *et al.* suggested that the mechanism of wall-slip and shear banding in the CNF suspensions under shear flow could be explained by the presence of a water-rich layer near the stationary plate or cylinder of the corresponding geometry. [151] They observed

that CNF flocs were ejected during continuous shear measurements in a cone-plate geometry. By adding tracer particles to the CNF suspension, they found that the fibrils under shear moved as flocs, and only the water layer near the bottom plate was continuously sheared. Thus, the shear thinning of CNF suspensions should be explained by the water layer rather than breakdown of aggregated fibrils as suggested in other studies. [120, 152] However, the authors also pointed out that wall-slip is conceptually different from the existence of a water-rich layer and that the interpretation as wall-slip should be used with caution. As more than 90% of a CNF suspension is water, the existence of a water layer is the characteristics of this material, which cannot be avoided. Methods that suppress the wall-slip during a measurement may risk misrepresenting the true flow behaviors of CNF.

2.3 Rheological Characterization and Modeling of TEMPO-CNF

2.3.1 Concentration Effects

Due to the concerns of wall-slip and heterogenous flow, rheology studies of TEMPO-CNF across a wide range of concentrations are limited, especially studies of shear viscosity. Some studies have measured the oscillatory rheology, where G' and G'' decrease with decreasing concentration, and where G' is found to have a power law relationship with the concentration, c: $G' \sim c^{\alpha}$. [153, 154] As the length and aspect ratio of the fibrils are larger than for CNC, gelation occurs at a much lower suspension concentrations: ~0.5 wt%) [155], which is an order of magnitude lower than the gelation concentration of CNC (~5 wt%) [140] although the exact values depend on nanoparticle or fibril characteristics.

As the fibril sizes of TEMPO-CNF, CNF and cellulose microfibrillated fibrils (CMF) are not well distinguished in literature, some early rheological studies of CNF and CMF are also reviewed here. These studies measured the flow curves for several concentrations. [156-158] Even though wall-slip concern were not explicitly addressed, the studies found that at high concentrations, the viscosity decreases with shear rate, showing a single shear thinning behavior. At intermediate concentrations, the viscosity first decreases, then plateaus and is finally followed by another shear thinning regimes; this behavior is similar to the three-regime shape of flow curves for CNC suspensions in liquid crystalline phase, as discussed in Section 2.1.1. Hysteresis loops in the flow curves are also reported for suspensions at intermediate concentrations. [152, 157] Nevertheless, the origin of the three-regime and hysteresis is unclear, which may even be an artefact caused by heterogenous flow. [159]

2.3.2 Morphological Effects

Previous studies have changed the morphology of TEMPO-CNF suspensions mainly via pressure homogenization. Besbes *et al.* reported that viscosity increased with higher number of passes through the homogenizer at constant pressure. [160] The viscosity change was unfortunately probed only within a narrow shear rate range from 1 to 10 s^{-1}, and the viscosity increased from 18 *Pa·s* without homogenization to 70 *Pa·s* after 15 passes. Naderi *et al.* found that higher number of passes leads to increase of viscosity and oscillatory moduli (G' and G'') for carboxymethylated CNF, [161] and Lin *et al.* found that higher viscosity resulted from homogenization at higher pressure for bacterial CNF. [162] Non-monotonic changes were reported by Shogren *et al.*, who found that G' increased with

increasing homogenization passes, reaching a maximum after the 2nd pass, and then noticed that G' started to decrease. [163]

The change of fibril size during the pressure homogenization process is unclear, as few studies provide reliable size characterizations. It is generally regarded that viscosity increases indicate fibrillation, while viscosity decreases indicate shortening of the fibrils. [64] Li *et al*. measured the fibril size by dynamic light scattering, and found that the average particle size decreased with increasing pressure and number of passes, though the rheological properties are not characterized. [164] Grinding and refining are also used to change the morphology of TEMPO-CNF, though the fibrillation efficiency is not as high as the pressure homogenizer, and the produced fibrils are not well dispersed. [165, 166]

Some studies obtained different fibril sizes by using different wood pulps. [167, 168] Although the size characterization showed that the fibril lengths are different, the differences in rheology cannot be attributed to fibril size only. The fibril composition also varies with the pulp source, which may also lead to different rheological properties.

The morphology of TEMPO-CNF is rarely changed by sonication, because the fibrils are readily broken by the high energy intensity of sonication. [169, 170] In fact, sonication has been used to produce TEMPO-CNC, where the cellulose fiber is first treated with TEMPO-mediated oxidation to produce fibrils of high surface charge (at least 1 mmol/g). [171, 172] The following sonication process not only fibrillates, but also break down the fibrils into needle-like nanoparticles.

2.3.3 Surface Charge Effects

The surface charge of TEMPO-CNF is increased by increasing the amount of oxidation agent or the oxidation time, and is quantified by the carboxylate content measured via conductometric titration as discussed in Section 1.1.3. [70, 77] Previous studies report surface charges mostly in the range of 150-1000 μmol/g. [160, 173] The rheological properties η, G' and G'' were found to decrease with higher surface charge by some studies. [160, 174, 175] In contrast, Bettaieb *et al*. reported the reverse trend, where G' and G'' slightly increased with higher surface charge, but their samples were not fibrillated under identical conditions. [176] The sample with higher surface charge underwent fewer grinding passes, which could easily have led to a lower degree of fibrillation and thus higher G' and G''. Wen *et al*. produced lignin-containing TEMPO-CNF with carboxylate content of 0.5 to 1.3 mmol/g. [177] With increasing carboxylate content, the lignin content decreases, and the viscosity was found to increase. This shows that the TEMPO oxidation will also affect the lignin content of the fibril, which needs to be characterized if the nanofibrils are not lignin-free.

2.3.4 Modeling and Size estimation

Rheological models have been used to fit the flow curves of TEMPO-CNF suspensions in the literature. However, the parameters extracted from the models are not typically used to estimate material properties and changes thereof. Sebenik *et al*. used Roberts-Barnes-Carew (RBC) model (**Equation 2-6**) to extract the zero-shear viscosity η_0 and tracked its changes over days to study the aging effect. σ_r is the critical stress, and the exponent *m* describes the shear thinning. [178] The model, which is a variation of the Cross

model (**Equation 2-7**) can fit the flow curves at several concentrations. λ is the characteristic time in the Cross model.

$$\eta = \eta_\infty + \frac{\eta_0 - \eta_\infty}{1+(\sigma/\sigma_c)^m} \quad (2\text{-}6)$$

$$\eta = \eta_\infty + \frac{\eta_0 - \eta_\infty}{1+(\lambda\dot{\gamma})^n} \quad (2\text{-}7)$$

The Herschel–Buckley model (**Equation 2-8**) has been used to fit the flow curve of CNF/CMF at 0.5 wt% for different fibril morphologies. [179] τ is the shear stress, τ_0 the apparent yield stress, *k* the flow consistency and *n* is the flow index. Thought the model fits the data well, the data itself covers only a narrow range of shear rates (10 to 100 s^{-1}), and consequently the shear stress range only covers 5 to 15 Pa.

$$\tau = \tau_0 + k\dot{\gamma}^n \quad (2\text{-}8)$$

Size estimations of TEMPO-CNF in previous studies mostly use intrinsic viscosity *[η]* and related empirical equations. Iwamoto *et al*. estimate the aspect ratio of CNF from *[η]* using the Simha equation (Equation 2-3) and λ = 1.5 is used. [180] The *[η]* is obtained by extrapolating η/η_s at zero concentration, and η_s is the solvent viscosity. However, *[η]* is taken at the shear rate of 39.81 s^{-1}, which is much smaller than the shear rate at which the viscosity is extracted to estimate the CNC aspect ratio as discussed in Section 2.1.3. Shinoda *et al*. developed an equation that connects the degree of polymerization (DP_v) of TEMPO-CNF to the fibril length: Length = 4.286 DP_v – 757. [181] The DP_v is calculated from *[η]* using an empirical equation for rigid polymers: $[\eta] = 0.57 \cdot DP_v$ and *[η]* was measured by a capillary viscometer. Tanaka *et al*. developed an empirical equation to estimate the aspect ratio *p* of TEMPO-CNF by measuring its viscosity (Equation 2-9),

where ρ is the density of nanocellulose $\rho = 1.6$ g/cm^3 and $[\eta]_e$ is the experimental intrinsic viscosity. [182] The $[\eta]_e$ is determined from the Fedors equation (Equation 2-4). The authors pointed out that their equation had a similar form as the well-known Mark-Houwink-Sakurada equation $[\eta] = K \cdot M^a$, where M is the molecular weight, and K and a are constants.

$$\rho \cdot [\eta]_e = 0.15 \cdot p^{1.9} \tag{2-9}$$

In addition to using the intrinsic viscosity, some studies have showed that the maximum relaxation time (τ) can be used to estimate the length of TEMPO-CNF fibril. An empirical equation developed for the flow behavior of rigid rod-like particles in the dilute regime is used (Equation 2-9), where η_s is the solvent viscosity, k_B is Boltzmann constant, T is the absolute temperature, L is the fibril length. [183] d is the fibril width, which is estimated as hydrodynamic radius or determined by electron microscopy. τ can estimated from the cross-over frequency in a frequency sweep for a viscoelastic suspension, where the intersection indicates the boundary of terminal relaxation and rubbery plateau regions. For very dilute suspension that G' is undetectable, τ is determined by $1/\dot{\gamma}_{crit}$, where $\dot{\gamma}_{crit}$ is the critical shear rate at the beginning of the shear thing. [184]

$$\tau = \frac{\pi \eta_s L^3}{18 k_B T ln(L/d)} \tag{2-9}$$

Nevertheless, validating the accuracy of these models is challenging as the size of the fibrils are even more difficult to measure due to the fibril flexibility compared to the rigid CNC particle.

CHAPTER 3. DEVELOPING PREPARATION AND TEST PROTOCOLS FOR RHEOLOGICAL CHARACTERIZATION OF CELLULOSE NANOMATERIALS

Parts of the material in this chapter have been published in two manuscripts: J. Liao, K.A. Pham and V. Breedveld, Rheological characterization and modeling of cellulose nanocrystal and TEMPO-oxidized cellulose nanofibril suspensions, *Cellulose* **27** (7), 3741-3757 (2020), DOI: 10.1007/s10570-020-03048-2; and J. Liao, K.A. Pham and V Breedveld, TEMPO-CNF suspensions in the viscoelastic regime: capturing the effect of morphology and surface charge with a rheological parameter, *Cellulose* **28**, 813–827 (2021), DOI: 10.1007/s10570-020-03572-1.

3.1 Introduction

As discussed in Chapter 1, to expand the production capacity to industrially relevant scales and to ensure consistently producing high-quality cellulose nanomaterials (CNM), one of the most urgent issues to be addressed is the lack of standardized, rapid and reliable characterization methods for quality control during the manufacturing process. [82, 84] The current characterization techniques, such as electron microscopy and light scattering, are expensive and time-consuming, and cannot easily be integrated into an industrial manufacturing process for online monitoring. Moreover, these methods suffer from potential bias because they only probe a small portion of the CNM sample; as a result, they can misrepresent the sample's bulk properties. Rheological measurement provides an attractive alternative. Rheological instrumentation (rheometer or viscometer) is relatively

inexpensive, easy to operate on a routine basis and can use CNM suspensions directly without extensive preparation steps. In fact, rheology is routinely used in research, development and quality control for polymer production because the methodology can provide quantitative monitoring of several important polymer properties, such as molecular weight (average value and distribution) [185] and microstructure (*e.g.* long chain branching). [186]

Compared to polymers, for CNM there is still a need to develop standardized protocols for viscosity measurements and robust empirical models to quantify the flow behavior and microstructure. The shear rheology (viscosity as a function of shear rate) of CNM has been studied with the main focus being the effect of concentration. In general, it has been found that the higher the concentration, the higher the viscosity. The flow curves of CNC can be classified into three general categories with regards to the shape of the flow curve, even though the actual viscosity values have been found to depend on the source, processing and preparation conditions. [54, 57, 102, 105] At low concentrations, the viscosity is essentially constant across shear rates indicating Newtonian behavior, or a low-shear viscosity plateau is accompanied by slight shear thinning at high shear rates. At intermediate CNC concentrations, shear thinning is first observed at the lowest shear rates, followed by a viscosity plateau region, and then another shear thinning region at high shear rates. This three-region flow curves resembles that of liquid crystalline polymers. [98] The first shear thinning region has been suggested to originate from the breaking of aggregated domains or clusters. The plateau region indicates that the microstructure of the CNC suspension remains unchanged until the shear flow is finally strong enough to align individual particles, which shows as the second shear thinning region. [54] At the highest

concentrations, the viscosity decreases linearly with increasing shear rates on a log-log plot, indicating a gel phase with typical power-law behavior.

The rheology of CNF and TEMPO-oxidized cellulose nanofibrils (TEMPO-CNF) have also been studied. CNF consists of aggregated fibril bundles and long fibers of large size variations; therefore, it is difficult to perform accurate and reproducible rheological studies. [146, 152, 158] Wall slip, heterogeneous flow and flocculation may occur during the measurement process, and thus affect the reproducibility and the reliability of the results. [150, 151] Chemical pretreatment have been developed to obtain individually dispersed fibers, and reduce energy consumption during the CNF manufacturing process. TEMPO (2,2,6,6-tetramethylpierridine-1-oxy) mediated oxidation of CNF followed by grinding fibrillates the fibers. However, wall slip, shear banding and heterogeneous flow may still occur during the rheological measurement, and thus affect the reproducibility and the reliability of the results. [145, 187] Another method to fibrillate and obtain highly dispersed TEMPO-CNF is through pressure homogenization. [188-190] Considering its improved dispersibility, smaller fibril length and more uniform size distribution, TEMPO-CNF, especially when pressure homogenized, is a better alternative to perform in-depth rheological studies. Previous rheological studies on TEMPO-CNF have investigated the effect of rheometer geometry, [191, 192] viscoelastic and gel properties measured by oscillatory rheology, [153, 168, 193], aging [178] and flow curves over a limited range of concentrations. [167, 190, 194]

Although previous studies have characterized the CNM viscosity and studied the concentration effect, a knowledge gap still exists when it comes to translating lab-scale rheological characterization to industry-scale quality control. One of the challenges that

must be resolved is the lack of robust test protocols to obtain reliable data. Published studies provide few specific guidelines and protocols for rheological measurements of cellulose nanomaterials at different conditions. [77, 195]

In this chapter, we develop detailed preparation and test protocols for characterization of cellulose nanocrystal (CNC) and TEMPO-mediated oxidized cellulose nanofibril (TEMPO-CNF). The preparation protocols include methods to determine sample concentrations and to disperse samples in water to form suspensions. The rheological test protocols include sample conditioning prior to testing and experimental parameters such as shear rates and interval time. We present detailed rheological studies of CNC and TEMPO-CNF at different concentrations, different temperatures, and study the effect of ionic strength on CNC rheology.

3.2 Materials and Preparation Protocols

3.2.1 Materials

Cellulose nanocrystals (CNC) at concentration of 12.1 wt%, cellulose nanofibril (CNF) (Lot # U-44) at 3 wt% and TEMPO-CNF (Lot # 2018-FPL-CNF-121) at 1.1 wt% were purchased in slurry form from the Process Development Center at the University of Maine, and stored at 4 °C, which is preferred for long-term storage. [196] Sodium chloride (NaCl), calcium chloride ($CaCl_2$), and dialysis tubing (14,000 MW cutoff) were purchased from Ward's Science (Rochester, NY). A gold-coated silicon wafer for SEM imaging was obtained from Angstrom Engineering Inc. (Kitchener, Canada) The TEMPO-CNF material used in the temperature study (Section 3.4.7) was provided by Jeffery Luo from the Kumar

group at Georgia Tech, and the procedure to produce the TEMPO-CNF suspension is described in his previous publication. [188]

3.2.2 Determination of Dry Content (CNC and TEMPO-CNF)

The dry content of all CNM stock was determined by oven-drying following the procedures in the protocol published by the Canadian Standard Association[195] except for the last step, in which our samples were first left in the lab to cool down and then placed in a TAPPI standard temperature and humidity controlled room (23 °C and 50% relative humidity) for 5 days to achieve equilibrium. The stock concentration of commercial CNC is 11.5 wt%, TEMPO-CNF is 1.08 wt% and TEMPO-CNF used in the temperature study is 0.8 wt%.

3.2.3 Preparation of CNM Samples at Various Concentrations

Rheological measurements require standardized protocols for sample handling,[110] especially for samples prepared at various concentrations when mixing is involved that can affect sample rheology. The CNM stock is in slurry form and kept in a fridge at 4 °C. Samples at various concentrations were prepared by diluting the stock. Before sample preparation, the stock was taken out from the fridge to warm up to room temperature. Each sample was prepared to have a total mass of 6 g in a 20 mL vial to reduce possible variability resulting from dilution. The sample was vortexed (Fisher vortex) at speed 6 or 7 for at least 30 seconds until it was visually homogenous without apparent aggregation.

3.2.4 Dialysis of CNC and Preparation at Different Ionic Strengths

Portions of the original CNC suspension were dialyzed in two separate dialysis tubes against distilled water for 7 days while changing the water every 12 hours for the first 2 days, then every 2 days for the next 5 days. The two batches of dialyzed CNC were denoted as ‘‘dia-CNC-1’’ and ‘‘dia-CNC-2’’. The dia-CNC-1 was used to study the concentration effect on viscosity, and the dia-CNC-2 was used to study the effect of added salt on viscosity. For dia-CNC-2 with added salt NaCl and $CaCl_2$, the ionic strength is used to represent the amount of salt added to the dialyzed CNC suspensions, which includes both salt concentration (c) and valence (z): $I = \frac{1}{2}\sum_{i=1}^{n} c_i z_i^2$. For example, 0.01 mol/L NaCl solution has an ionic strength of 0.01 mol/g and 0.01 mol/L of $CaCl_2$ has an ionic strength of 0.03 mol/L.

3.2.5 Polarized Optical Microscopy

Polarized microscopy images of CNC were taken using a Leica DM 2500p microscope with a polarizer. A drop of CNC suspension was placed between two microscope cover slips (25 x 75 mm, 1.0 mm thick, VWR Micro Slides). The polarizer was set at a 90-degree angle.

3.2.6 FE-SEM Imaging

Negative contrast was used to image the CNC and TEMPO-CNF to minimize the substrate interactions on distorting the fiber size.[197] The samples were diluted to 0.01 wt% in water, dropped onto a gold-coated silicon wafer and air-dried. Samples were not coated with metal prior to imaging. Scanning electron microscopy (SEM) imaging was

performed using a Hitachi SU8010 FE-SEM at 1kV accelerating voltage and working distance (WD) around 3 mm. **Figure 3.1** shows the SEM images of the CNC and TEMPO-CNF used in this study.

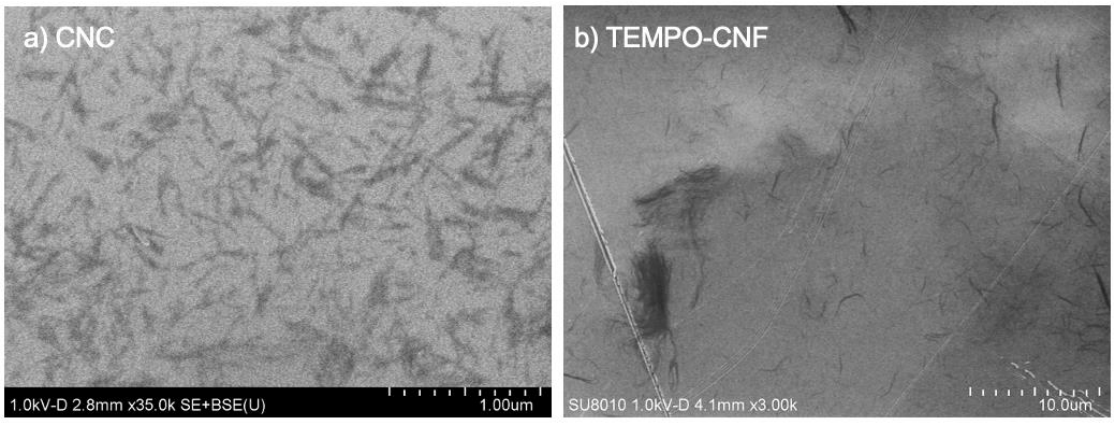

Figure 3.1 SEM images of (a) CNC and (b) TEMPO-CNF used in this study. These two materials are commercial products purchased from the processing development center of University of Maine.

3.3 Rheological Test Protocols

The rheological measurements were performed on a rotational rheometer (MCR 302, Anton Paar) with a cone-plate geometry. The cone is 50 mm in diameter (cone angle 1.01°, truncation 0.053 mm), and the bottom plate insert has a diameter of 60 mm. Both plates have smooth surfaces. The nominal sample volume is approximately 0.62 mL to ensure full coverage. The temperature for all measurements was at 25 °C and an evaporation blocker was used to prevent evaporation. [198] The sample was loaded onto the bottom plate, and the top plate was manually lowered down under slow rotation upon touching the sample to help distribute the sample evenly between the plates. The whole test sequence took approximately 35 minutes, during which evaporation of the sample was

negligible. The edge of the sample did not recede and there was no trace of dry film forming on the plate.

Each measurement started with pre-shear at 1 s^{-1} for 30 seconds and subsequently rested for 10 minutes to reset the sample's shear history after sample loading. Each viscosity measurement consisting of three flow curves can enable detecting thixotropic effects that could complicate data interpretation and eliminate potential hysteresis effects for both CNC and TEMPO-CNF. (**Figure 3.2**) The shear rates and averaging time for the measurement protocol are specified as in **Table 3-1**. In each interval, the shear rate increased, and the averaging time decreased according to a logarithmic ramp rate. The flow curves were measured with three points per decade of shear rate. The viscosity data reported in this study represents the average of the values measured during the three intervals at that specific shear rate. The repeatability of the flow curves at each concentration was checked by running viscosity tests for three fresh samples.

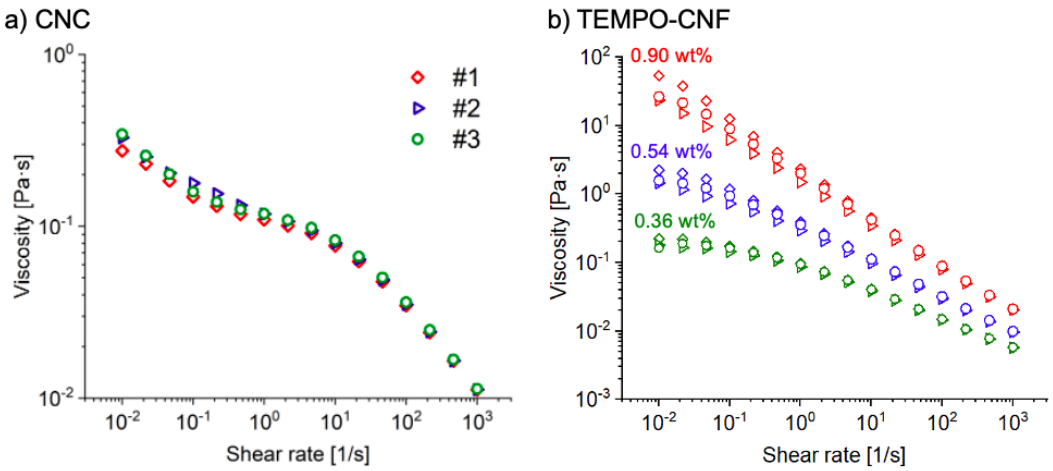

Figure 3.2 Each viscosity measurement consists of three intervals. The first interval is from low to high shear rate, the second interval from high to low shear rate, and the third interval from low to high shear rate again. Examples of three intervals of flow curves are measured in one viscosity test for (a) 5.8 wt% CNC sample and (b) TEMPO-CNF of 0.90 wt%, 0.54 wt% and 0.36 wt%. The thixotropy is apparent for TEMPO-CNF at high concentrations (> 0.54 wt%), whereas the thixotropy is negligible at lower concentrations (⩽0.54 wt%).

Table 3-1 Shear rate and averaging time during logarithmic shear rate ramp used for viscosity measurements in this study.

Interval	Shear rate [s^{-1}]	Averaging time [s]
#1	0.01 - 1000	100 - 5
#2	1000 - 0.01	5 - 100
#3	0.01 - 1000	100 - 5

It is important to identify the appropriate lowest shear rate at which accurate viscosity data can be obtained, especially for low concentration samples, due to instrument limitations and sample loading issues. Correct measurements, in general, have similar shapes of the three consecutive flow curves, with the first curve having a slightly higher viscosity, the second curve slightly lower viscosity and the third curve in between. (**Figure 3.2**) Correct loading of the sample, without too much excess of sample volume around the cone, is also important to obtain accurate viscosity data.

For oscillatory test, strain amplitude sweeps from 0.01 to 10 at frequency 1 rad/s were performed to identify the linear viscoelastic region. Frequency sweeps from 0.1 to 100 rad/s were then performed to examine viscoelasticity and probe gel-like behavior. A recovery test was used to study the time evolution of the material microstructure destruction and subsequent recovery at rest. G' and G'' are measured in three intervals of different strain, all at 1 rad/s frequency. The strains used in the first and the third interval are the same and are within the linear viscoelastic region based on the strain sweep experiment. This small strain probes the initial state of the material microstructure in the first interval and the structural recovery during the third interval. The strain in the second interval is 10, aiming to destroy the existing microstructure. The recommended times are at least 10 minutes for the first and second interval, and at least 30 minutes for the third interval.

Flow curves were also measured at elevated temperatures ranging from 25 ºC to 55 ºC. Silicone oil with viscosity 10 mPa·s was added to cover the outer edge of the suspension that that is exposed to air. (**Figure 3.3**) The 60 mm bottom plate, which is slightly larger than the cone, was used to provide space for the silicone oil layer. Shear rates of 0.01 – 100 s^{-1} was used to avoid the silicone oil from being mixed with the measured nanomaterials by secondary flows that can develop at higher shear rates.

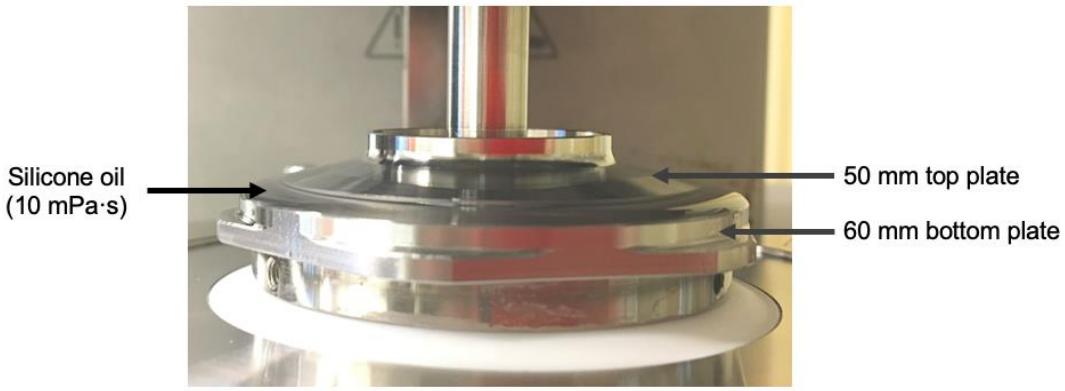

Figure 3.3 The setup for rheological temperature studies where a silicone oil with viscosity 10 mPa·s is used to cover the outer edge of the sample to prevent evaporation.

3.4 Results and Discussions

3.4.1 Dry Content of CNC and TEMPO-CNF

Dried CNM can easily absorb water from the ambient environment due to the accessible hydroxyl groups on the surface. The moisture content of dried CNC films can reach up to 11.2 wt% when exposed to 80% relative humidity (RH), and cellulose microfibril films can reach 15 wt% moisture content when exposed to 90% RH. [199] Moreover, a hysteresis loop exists in the sorption isotherm: at the same RH value, the moisture content is higher upon desorption than adsorption. Thus, it is difficult to determine the CNM dry content due to its strong dependence on the ambient environment. **Table 3-2** summaries the dry content (wt%) of the CNC and TEMPO-CNF that is measured gravimetrically after exposure to different environmental conditions. The dry content of the stock solution is quantified as m_2/m_1, where m_2 is the sample weight after drying, and m_1 is the initial weight of the suspension sample before drying. The m_2 for the condition

labeled “after oven-dry” is measured 15 minutes after the sample is removed from the oven and has cooled down to room temperature. The sample container is covered loosely with parafilm to prevent dust contamination. The m_2 for the condition “in lab” is measured after the sample container is exposed to the ambient air of the relatively well-controlled lab (22.5°C ± 0.5°C and 51.5% ± 1.5% RH) for at least 5 days; and the m_2 for the condition “in environmental chamber” is measured after the sample container is kept in a TAPPI standard temperature and humidity control room (23°C and 50% RH) for at least 5 days. The lab condition is close to the TAPPI standard, but with a larger variability than the dedicated environmental chamber. The average and standard deviation of the dry contents are obtained from five measurements performed throughout a year using the same stock solution from the supplier. The standard deviation is the smallest for samples that are tested after equilibrium in the environmental chamber. Therefore, the dry contents for other CNM materials (dialysis CNC and TEMPO-CNF) are determined using the same protocol. The difference in dry content is 0.6 wt% for CNC and 0.07 wt% for TEMPO-CNF between supplier specification and oven drying with subsequent exposure to the environmental chamber room. This implies that one should not directly use the specified dry content, especially if the concentration is high, but should determine the dry content after receiving the samples from the supplier.

Table 3-2 Dry contents [wt%] of as-received CNC and TEMPO-CNF after reaching equilibrium in different environments.

Material	Supplier specification	After oven-dry	In lab	In environmental chamber
CNC	12.1	10.63 ± 0.16	11.54 ± 0.17	11.51 ± 0.05
TEMPO-CNF	1.1	1.01 ± 0.05	1.11 ± 0.05	1.08 ± 0.03

3.4.2 Effect of Mixing Method

The CNC and TEMPO-CNF samples were diluted from stock to several concentrations to study their rheology. Therefore, a reproducible mixing method that can produce consistent results is essential. 5.8 wt% CNC suspensions were prepared using vortex mixing and probe sonication at different speed/power settings for different lengths of time, and the resulting flow curves were compared (**Figure 3-4**). Lower vortex speed or shorter time leads to insufficient mixing. Higher vortex speed or longer duration does not change the viscosity, (**Figure 3.4a**) but the strong mixing will generate bubbles in the suspension that are challenging to remove. The flow curves are reproducible if the same vortex speed and time are used. Probe sonication also leads to reproducible results when using the same sonication power and time, but the flow curves are more sensitive to the sonication power and time than to vortex speed and time. Sonication power at 30% for 30 seconds produces a flow curve smaller than using 20% power, and sonication at 20% power for 3 minutes leads to a significant decrease in viscosity compared to 30 seconds. (**Figure 3.4b**) The probe sonication helps disperse the CNC particles in water suspension, especially for freeze-dried CNC.[54, 200] Nevertheless, for CNC in slurry form, sonication disperses the particles at the cost of changing the existing microstructures and morphologies. The aspect ratio of the CNC particles can be reduced due to the locally high sonication energy, and consequently the sample viscosity decreases, although suspensions with and without sonication are both stable, and their flow curves exhibit the same qualitative behavior as a function of concentration. However, the unknown effect of sonication on nanoparticle size and aspect ratio is undesirable for this study. In addition, vortex mixing works well for both CNC and TEMPO-CNF, allowing for consistent sample

preparation protocols. Sonication is known to affect TEMPO-CNF fibers more strongly than CNC, breaking the fibers and thus changing the suspension microstructure, leading to fibrillation or gelation. [169, 171] An Ultra-Turrax mixers are often used in the literature to mix TEMPO-CNF or CNF with water to avoid fibril breakage; these mixers impose mechanical shearing similar to the vortex mixing.[90, 92]

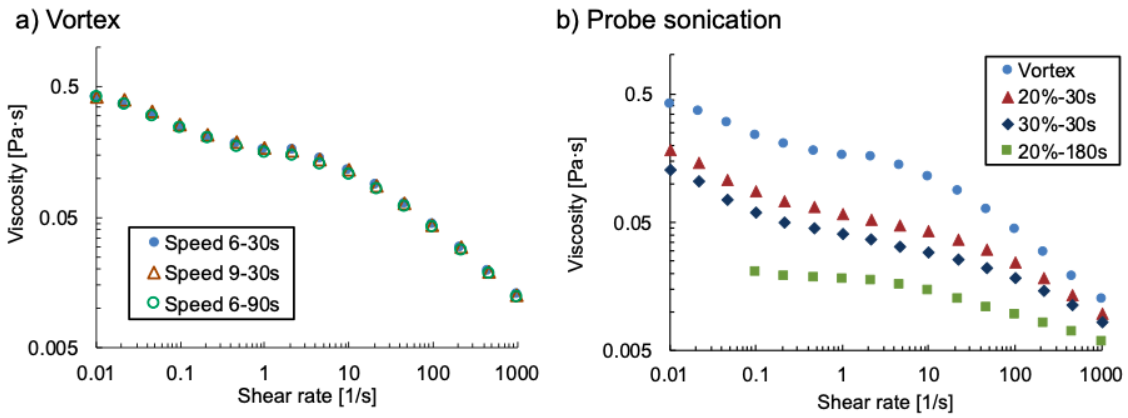

Figure 3.4 5.8 wt% CNC suspensions prepared by mixing the stock at 11.5 wt% with water by (a) vortex mixing and (b) probe sonication at different settings (speed/power and time), where 20% and 30% are the sonication power percentage.

3.4.3 Rheology of CNC Suspensions

The viscosity and phase behavior of CNC depend strongly on concentration. **Figure 3.5** shows the viscosity of CNC suspensions for dry contents ranging from 1.0 to 11.5 wt% with error bars indicating the variability. Every data point on the flow curve is calculated by first averaging the three intervals of each test as specified in the Methods section, and then averaging again among three separate tests. For clarity, the viscosity data are split into two figures. The shapes of the flow curves resemble data reported in the literature. [54, 95, 112] At low concentrations (1.0 - 3.8 wt%), the shear viscosity values are essentially constant at low shear rates, with the onset of shear thinning at around 10 s^{-1}. At medium

concentrations (4.3 - 9.6 wt%), the viscosity shows a three-region viscosity profile: shear thinning at low shear rates, then a plateau, followed by another shear thinning region at high shear rates. This shape of the flow curve indicates that CNC is in the chiral nematic phase. [54, 95] At high concentrations (9.5 - 11.5 wt%), the viscosity depends on shear viscosity according to a power-law relation across the entire range of shear rates, which is a typical gel behavior.

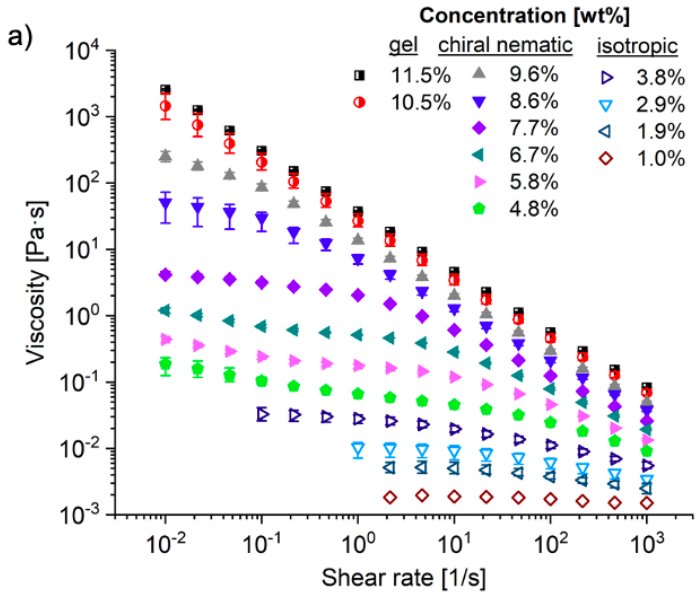

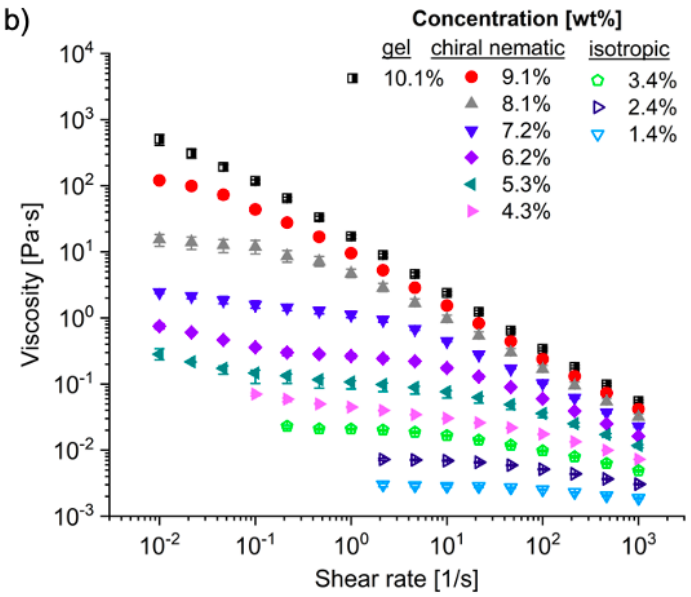

Figure 3.5 Flow curves of CNC suspensions as a function of shear rate at different solids contents; 10.1 - 11.5 wt% samples are in gel phase (half-closed symbols), 9.6 to 4.8 wt% in chiral nematic phase (closed symbols), and 3.8 to 1.0 wt% in isotropic phase (open symbols). The standard deviation for each point is shown as the error bar. The upper limit of the error bar is calculated as the maximum value of three tests (averaging the three intervals for each test) minus the average of the three tests. The lower limit of the error bar is calculated as the average minus the minimum.

The variability of the viscosity measurement, which has not been reported before in detail, is shown as the standard deviation of each data point. Generally, the standard deviation is smaller at high shear rates than at low shear rates, because larger shear force is imposed on the suspension to align the CNC particles, while at low shear rates randomly oriented CNC particles lead to more variations in viscosity. Moreover, the variation in viscosity is more significant at transition concentrations (around 4.8 and 8.6 wt%) at low shear rates. The phase transition from isotropic to chiral nematic of this CNC occurred at around 4.3 wt%, where the polarized microscopy image of 4.3 wt% is completely dark, while the image of 4.8 wt% shows patterns in faint colors (**Figure 3.6**) The phase transition from chiral nematic to gel phase is indicated by the frequency sweep, where 9.6 wt% shows

G' larger than *G''* at all frequencies, while 8.6 wt% shows crossover between *G'* and *G''* at 10 rad/s. (**Figure 3.7**)

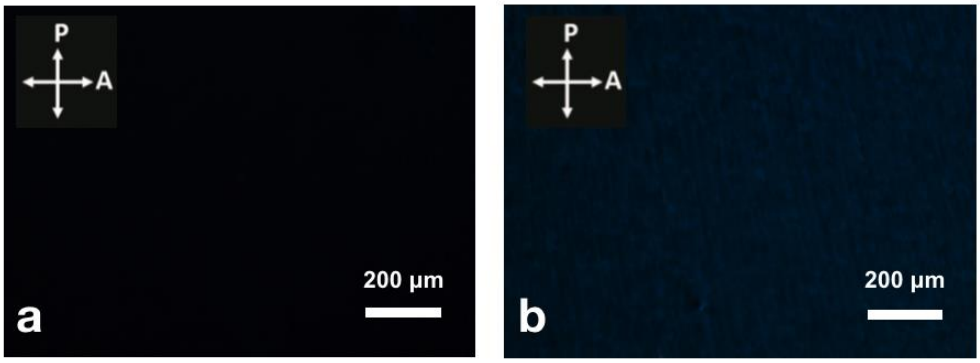

Figure 3.6 Cross-polarized microscopy images of (a) 4.3wt% shows no birefringence, completely black (b) 4.8 wt% shows patterns in faint colors, indicating the onset of liquid crystalline phase.

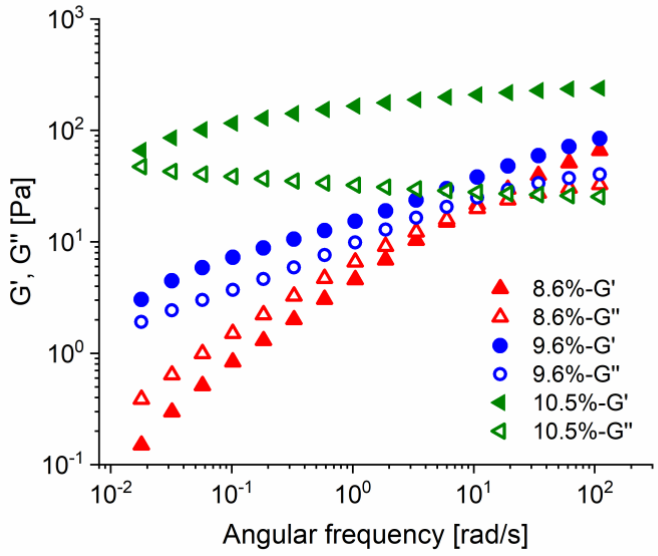

Figure 3.7 Frequency sweep shows the transition from chiral nematic phase to gel phase. 8.6 wt% is in the viscoelastic phase, where G' is smaller than G'' below 10 rad/s and G' is larger than G'' above 10 rad/s. 9.6 wt% shows G' larger than G'' at all frequencies, indicating that it is in the gel phase.

3.4.4 Rheology of TEMPO-CNF Suspensions

The rheology of TEMPO-CNF suspension, which is concentration dependent, is measured to identify the viscoelastic regime. (**Figure 3.8**) The frequency sweep data are split into two figures for clarity. At 1.08 wt%, the highest concentration investigated, the viscosity decreases with increasing shear rate, showing shear thinning behavior. Furthermore, G' is larger than G'' and both stay unchanged over a broad frequency range, indicating a gel. For 0.63-0.90 wt%, the viscosity at low shear rates gradually approaches a low-shear plateau. Gelation happens at around 0.63-0.72 wt% where $G' = G''$ across the frequency. At 0.10-0.54 wt%, $G'' > G'$ but still showing detectable G' values, suggesting a liquid-like viscoelastic behavior. For concentrations below 0.10 wt%, the G' is much smaller than G'', indicating that it is in the dilute regime. The correlation between viscosity and the concentration transitions from linear to power-law at around 0.10 wt%. (**Figure 3.9**) This threshold concentration identifies the boundary between the dilute and the viscoelastic regime.[184] Hence, this TEMPO-CNF sample is considered to be in the viscoelastic regime in the concentration range 0.10-0.54 wt%.

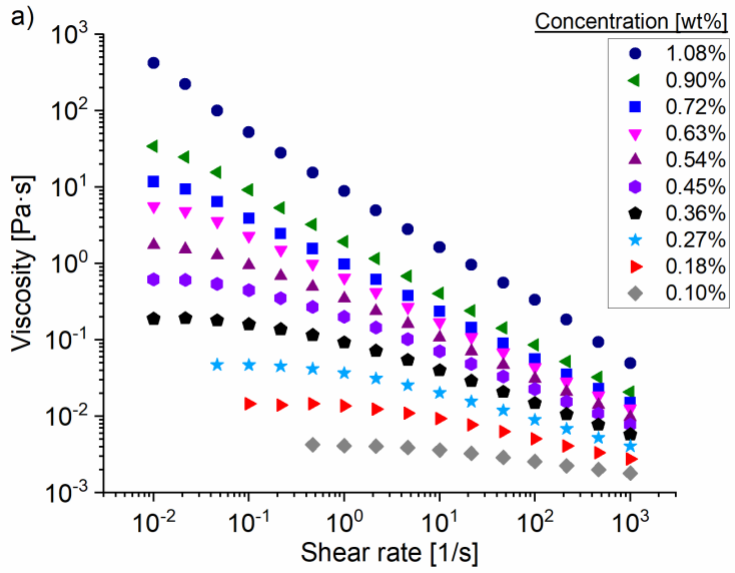
a)
Concentration [wt%]
1.08%
0.90%
0.72%
0.63%
0.54%
0.45%
0.36%
0.27%
0.18%
0.10%
Viscosity [Pa·s]
Shear rate [1/s]

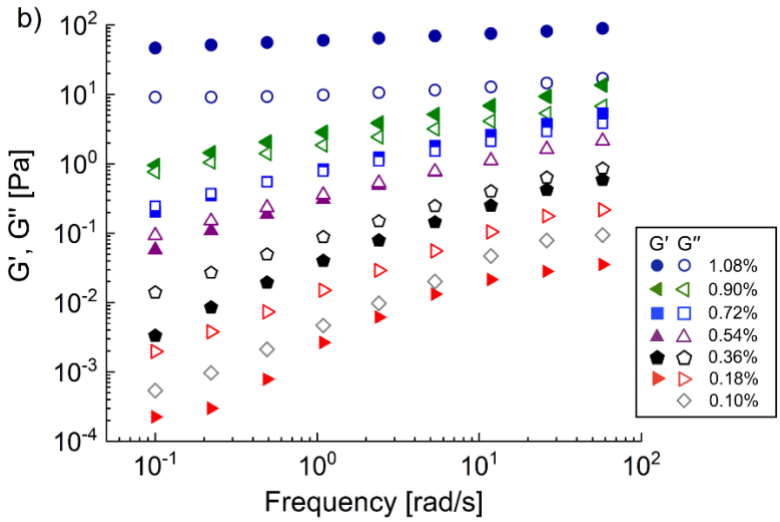
b)
G' G"
1.08%
0.90%
0.72%
0.54%
0.36%
0.18%
0.10%
G', G" [Pa]
Frequency [rad/s]

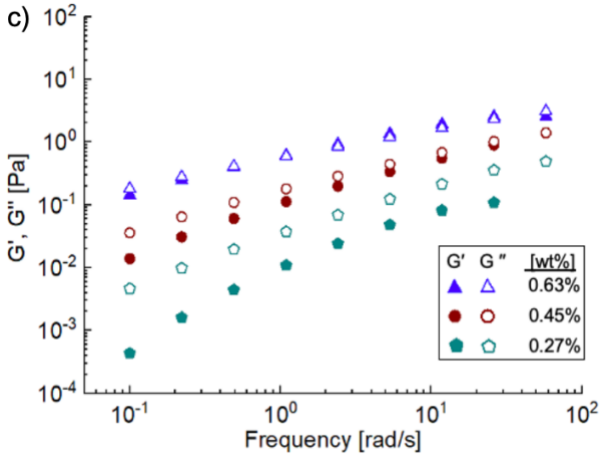

Figure 3.8 (a) Flow curves of TEMPO-CNF at different concentrations in dilute, viscoelastic and gel regimes. (b) and (c) The frequency sweep shows that gelation occurs around 0.63-0.72 wt%. 0.10-0.54 wt% is considered in the viscoelastic regime where G'' > G'.

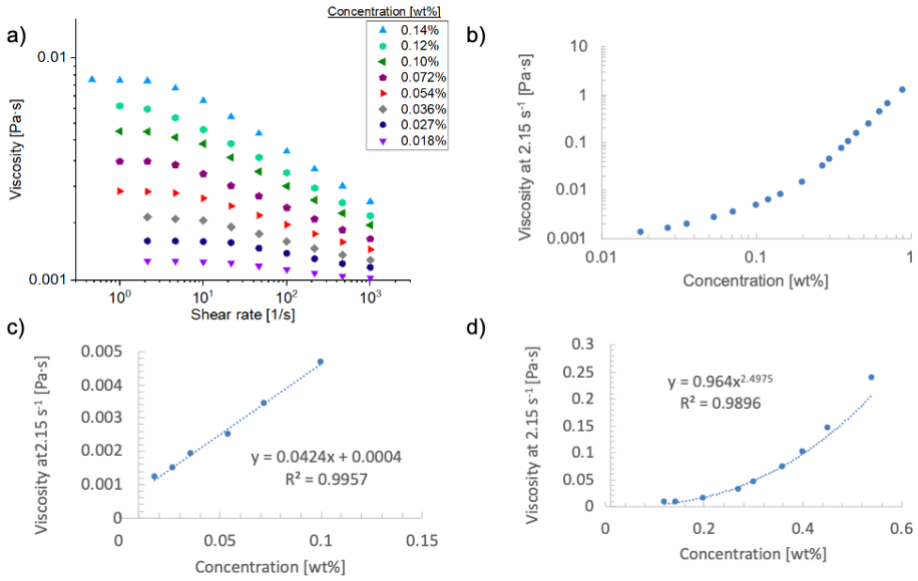

Figure 3.9 Additional rheological characterization for TEMPO-CNF suspensions: (a) flow curves at concentrations near and in the dilute regime; data supplemental to Figure 3.8a and presented here for enhanced clarity. (b) viscosities at 2.15 s^{-1} as a function of concentration, showing different scaling in the dilute and viscoelastic regimes and identifying 0.10 wt% as the threshold concentration for the viscoelastic regime. (c) viscosity scaling (linear) with concentration in the dilute regime (< 0.10 wt%); (d) viscosity scaling (power law) with concentration in the viscoelastic regime (0.10-0.54 wt%).

The flow curves in the viscoelastic regime plateau at low shear rates, then exhibit shear thinning at higher shear rates. Most of the CNF flow curves reported in the literature are purely shear thinning at higher concentrations, directly shifting to Newtonian behavior at lower concentrations. [168, 190] This is likely because the fibrils have larger lengths and smaller surface charges than the TEMPO-CNF used in this study. The TEMPO-CNF used in this study has a comparatively small fibril length (10-15 μm) even without homogenization. Its carboxylate content of 1.1 ± 0.1 mmol/g is also higher than many of the TEMPO-CNF samples described in the literature.[160, 174, 190] More negatively charged fibrils repel each other more strongly, resulting in better dispersion of fibrils in water. As a result, the CNF samples exhibit smaller viscosity at the same concentration as smaller friction is required to move fibrils under flow.

3.4.5 Wall-slip for CNC and TEMPO-CNF Suspensions

Concerns of wall-slip and heterogenous flow have been raised in measuring the rheology of TEMPO-CNF in the viscoelastic regime in previous studies.[61, 150, 187] Nevertheless, in our study, the stress versus shear rate curves show no signs of stress drop at low shear rate, which is otherwise a key indicator of slip. (**Figure 3.10**) These stress curves also show that the hysteresis probed by the three-interval measurement is small in the gel regime, and negligible in the viscoelastic and dilute regimes. A more definitive test to check whether a rheology test shows wall-slip is to measure the sample in multiple instruments and or geometries. The flow curves of TEMPO-CNF (pressure homogenized at 25000 psi for 7 passes) were measured using three different geometries: a smooth cone (angle 1°, diameter 50 mm) with a smooth bottom plate, the same smooth cone with a rough bottom plate, and a concentric cylinder (bob diameter 16.66 mm, cup diameter 18.07mm,

effective bob length 25 mm) with smooth surfaces. **Figure 3.11** shows the measured flow curves using three geometries at two different concentrations following our standard protocol. Each flow curve is the average of the three intervals. The agreement between the geometries is near-perfect across the entire shear rate range, with no significant deviations. The viscosity range of these samples is similar to viscosities of non-homogenized samples for which wall-slip has been reported in the literature; therefore, relevant range of stresses and viscosities are probed in these multi-geometry tests. Overall, considering the stress-shear rate curves of the original sample, and the flow curves measured by three geometries for another, similar TEMPO-CNF sample, the wall slip issue for the TEMPO-CNF suspensions in this study is believed to be negligible.

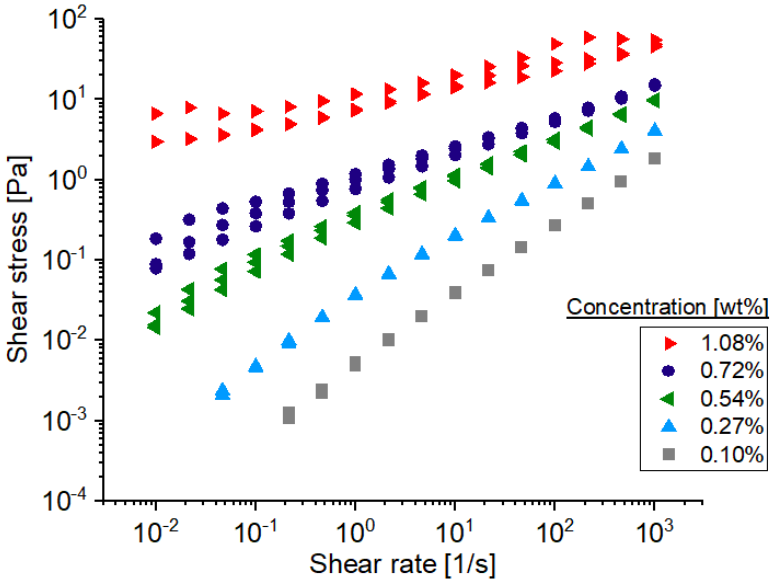

Figure 3.10 Three-interval flow curve measurements of TEMPO-CNF suspensions: stress vs shear rate curves for 1.08 wt%, 0.72 wt% (gel regime), 0.54 wt%, 0.27 wt% (viscoelastic regime), 0.1 wt% (dilute regime). Some hysteresis exists for samples in the gel regime, while little hysteresis is observed for samples in the viscoelastic and dilute regime.

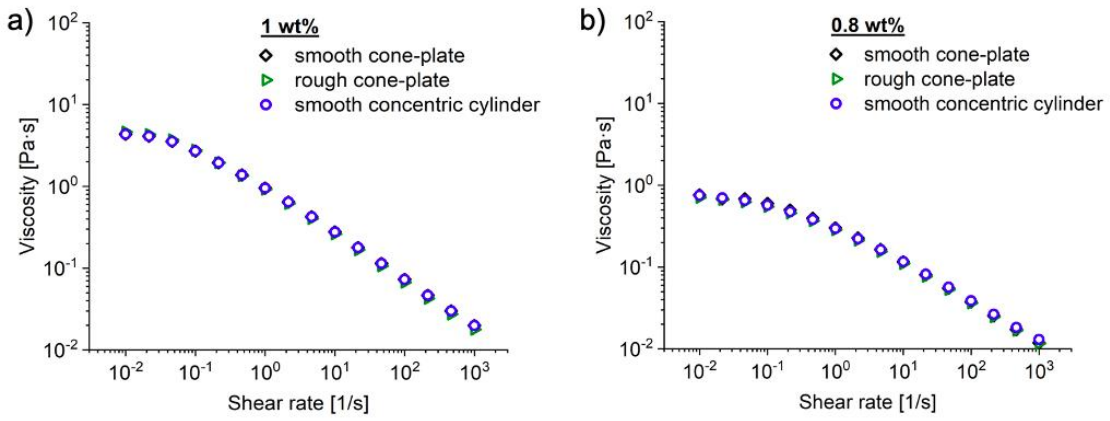

Figure 3.11 Flow curves of TEMPO-CNF (pressure homogenized at 25000 psi for 7 passes) measured using three different geometries. The three flow curves overlap indicating that the wall-slip is negligible.

Wall slip has not been raised as a major issue in the field of CNC rheology, which makes sense because of the colloidal dimensions of the CNC particles. There is no evidence in literature that this is a significant issue. Using smooth concentric cylinders, and smooth and rough parallel plates, Xu et al found negligible differences between the flow curves measured by the three geometries.[95] Flow curves of the 5.8 wt% CNC samples were measured using the same three geometries that were used to check wall slip in the TEMPO-CNF samples (smooth concentric cylinders, and smooth and rough cone-plate geometries). **Figure 3.12** shows that CNC does not exhibit wall slip; the small differences in magnitude of viscosity are due to slight sample-to-sample variations.

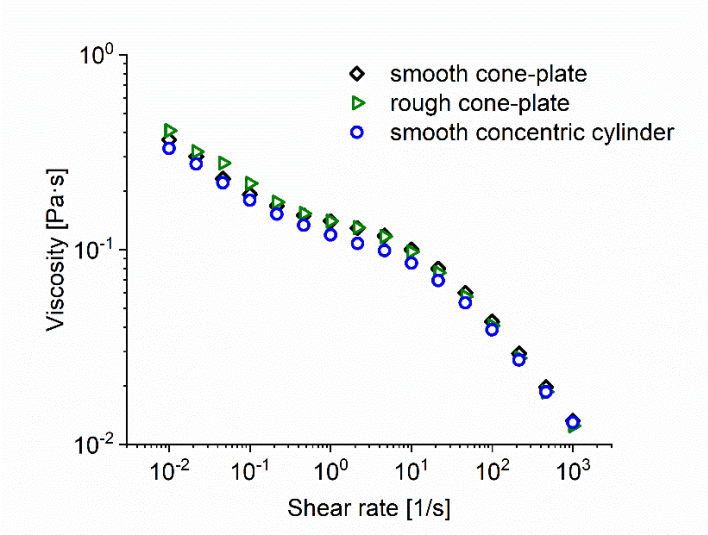

Figure 3.12 Flow curves of 5.8 wt% CNC measured using three different geometries. No wall-slip for CNC either, and the small differences of viscosities are due to slight sample-to-sample variation. Each flow curve represents an average of three interval and is not done in triplicate to address such variations.

Time-dependent behavior is observed for TEMPO-CNF suspensions after dilution from stock. As an example. the viscosity at 0.1 s^{-1} and G' at 1.1 rad/s were tracked over five hours for samples at 0.90 wt% and 0.45 wt%, and the values of these parameters gradually decrease until plateaus were reached after about 4 hours. (**Figure 3.13**) The decrease indicates that the fibrils are becoming less aggregated and mixing the TEMPO-CNF water suspension for extended time reduces heterogeneity. Thus, consideration and standardization of mixing time are necessary when preparing diluted TEMPO-CNF samples.

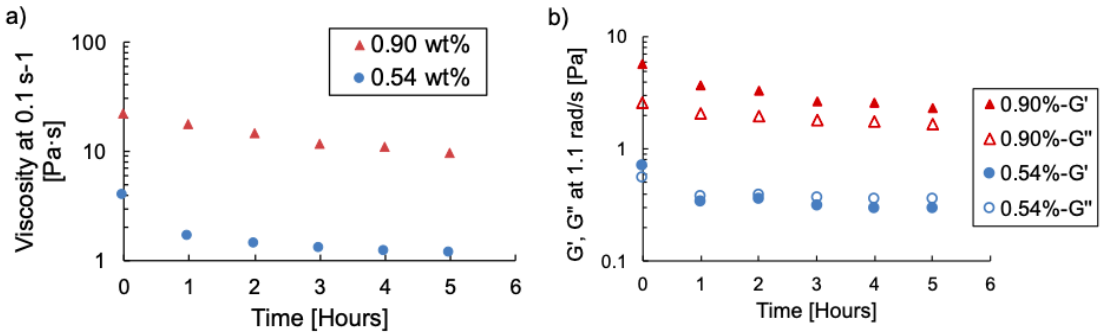

Figure 3.13 The viscosity at (a) 0.10 s^{-1} and (b) G' at 1.1 rad/s for TEMPO-CNF suspensions after dilution to 0.9 wt% and 0.45 wt% as a function of mixing time, showing gradual decrease and reaching plateau after about 4 hours. Thus, 4-hour was selected as mixing time to redisperse fibrils homogenously after dilution with water to achieve desired concentrations.

3.4.6 Salt Effects on CNC Suspensions

CNC particles are negatively charged, and the surrounding double layer is affected by the ionic strength, which can be modulated by adding salt to the suspension. The purchased CNC from University of Maine may contain residual salt, which affects the viscosity of the CNC suspension. Thus, we measured the viscosity of salt-free CNC (dia-CNC-1) to study the flow curve across concentrations. **Figure 3.14** shows a series of viscosity data of dialyzed CNC from 0.75 wt% to 9.0 wt% with increments of 0.75 wt%. At low concentrations (0.75 - 2.25 wt%), the suspension first shows a constant viscosity then starts shear thinning. At intermediate concentrations (3.0 and 3.75 wt%), the viscosity of the suspension has slight shear thinning at low shear rates, then plateaus followed by another shear thinning. Similar to the as-received CNC, the initial shear thinning region results from the alignment of domains or clusters, and the second shear thinning region is due to the alignment of individual particles at high shear. Dialysis removes salt from the CNC, leading to less aggregation. Thus, the slope of the first shear thinning region is smaller than that of the as-received CNC.

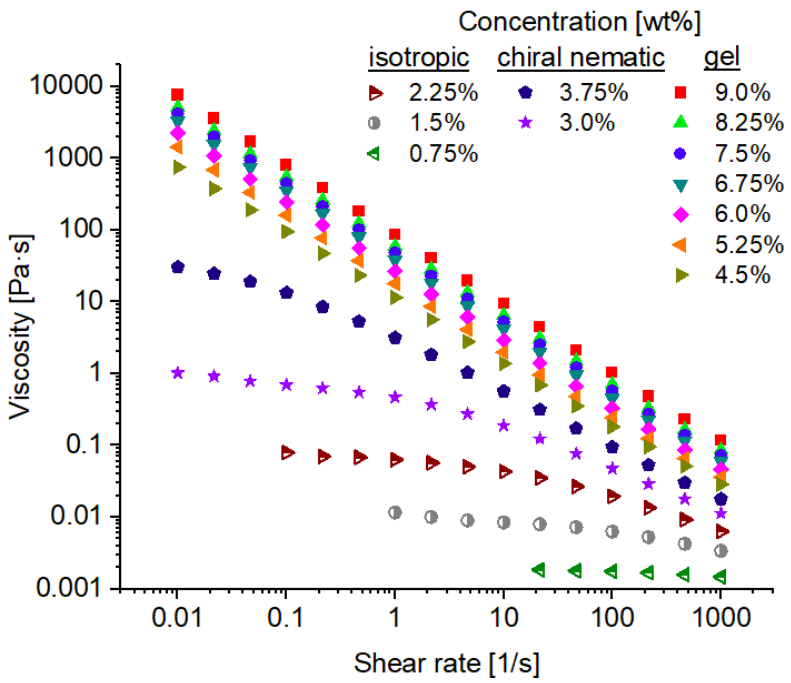

Figure 3.14 Flow curves of dialyzed CNC denoted as dia-CNC-1. 0.75-2.25 wt% are in isotropic phase, 3.0 wt% and 3.75 wt% are in chiral nematic phase, and 4.5%-9.0% are in gel phase.

The dialyzed CNC is not intrinsically different from the as-received CNC. The viscosity at 1, 10 and 100 s^{-1} for both as-received CNC and dia-CNC-1 forms a master curve at each shear rate by shifting the concentration of the dialysis CNC curve to twice its original value. (**Figure 3.15**) This confirms that dialysis will not change the intrinsic properties of the CNC particles.

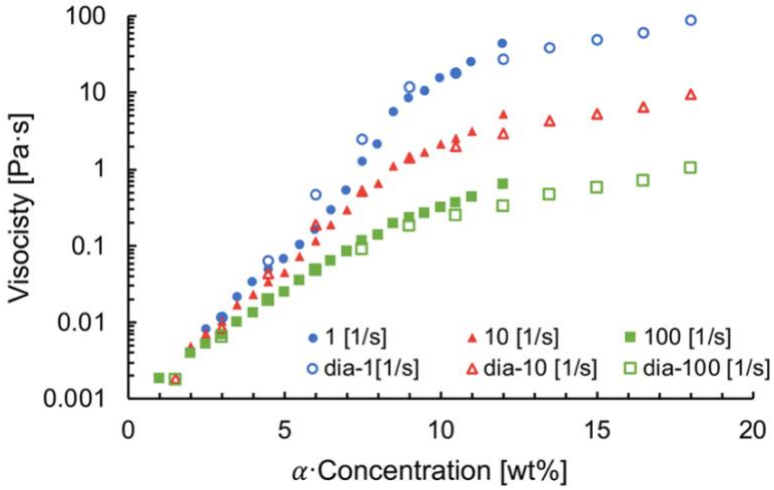

Figure 3.15 The viscosity of dia-CNC-1 and as-received CNC at shear rates of 1, 10 and 100 s^{-1} plotted in the same figure. The concentrations of dia-CNC-1 are shifted to twice the original values to form a master curve for each shear rate: α = 1 for as-received CNC and α = 2 for dia-CNC-1.

Additionally, NaCl is added to both the as-received CNC and dialyzed CNC (dia-CNC-2) at 4.0 wt% to form suspensions at various ionic strength. **Figure 3.16a** shows the flow curves of dia-CNC-2 after adding NaCl. At low ionic strength, the viscosity is greatly reduced. The flow curve plateaus at low shear rates followed by shear thinning. The flow curve turns into a single shear thinning when the ionic strength is further increased. **Figure 3.16b** shows the viscosity at 1 s^{-1} at various ionic strengths. Without adding NaCl, the viscosity of dia-CNC-2 (7.4 Pa·s) is much higher than the as-received CNC (0.033 Pa·s), indicating that dialysis removes enough residual salt to have a strong effect on electrostatic interactions. The viscosity of both as-received and dialyzed CNC decreases upon adding NaCl, reaching a minimum at around 20 mM ionic strength. The phase transition happens at 40 mM, where the three intervals of the viscosity test no longer overlap, indicated by the larger standard deviation. Further addition of NaCl induces gelation, leading to a rapid viscosity increase and more pronounced thixotropy. This trend follows what previously

reported in the literature.[133, 137, 138, 140] The divalent salt $CaCl_2$ was also added to dia-CNC-2 to study the viscosity change compared to the monovalent NaCl. The viscosity at 1 s^{-1} after adding $CaCl_2$ also decreases at first, reaching a minimum at around 7.5 mM ionic strength (or 2.5 mM $CaCl_2$ concentration), then rapidly increases. (**Figure 3-16c and d**) The viscosities before gelation transition do not fall onto a master curve at low salt concentrations but collapse when plotting against the ionic strength, indicating that ionic strength driving the electrostatic screening effect. Nevertheless, the onset of gelation is 7.5 mM ionic strength for $CaCl_2$, which is an order of magnitude of smaller than 20 mM for NaCl. Previous study found that $CaCl_2$ induces zeta-potential change at a lower salt concentration compared to NaCl and suggests that CNC gelation is induced at lower concentrations of divalent ions.[138] The turbidity measurement of CNC suspensions with NaCl and $CaCl_2$ addition also show that the turbidity values overlap at low ionic strength and starts to increase at a lower $CaCl_2$ concentration. [136] Measuring the viscosity in three intervals is still necessary even the intervals generally overlap for samples from 0.5 mM to 25 mM ionic strength. Adding concentrated salt to CNC suspension will result in local aggregations, which may not be easily broken down by normal vortex or mixing. These aggregations could lead to viscosity discrepancy at low shear rates, and measuring three intervals can help identify these hysteresis effects.

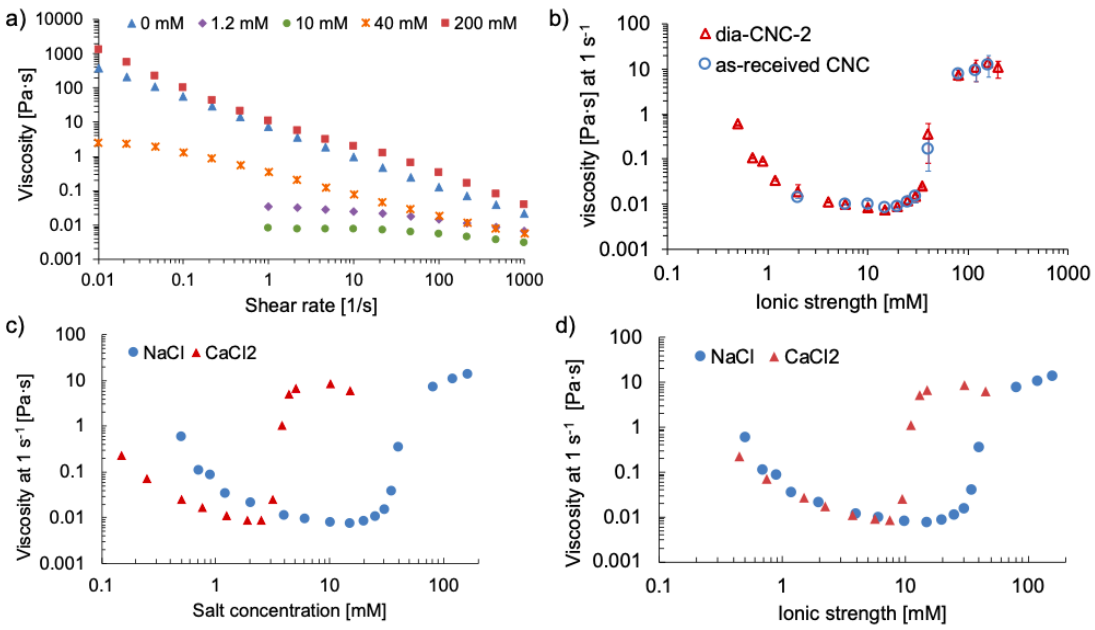

Figure 3.16 (a) Flow curves of dia-CNC-2 at various ionic strengths, modulated by adding NaCl. (b) viscosity at 1 s^{-1} for 4.0 wt% samples of as-received CNC and dia-CNC-2 as a function of ionic strength through addition of NaCl. (c) and (d) comparison of viscosity change at 1 s^{-1} for 4.0 wt% samples of dia-CNC-2 by adding NaCl and $CaCl_2$. The viscosities collapse when plot with ionic strength.

The time-dependent behavior of as-received CNC and salt-added CNC was examined by the recovery test. The test probes the material first under low-shear condition using a small strain, then destructs the material using a large strain, followed by the same strain condition to allow structural regeneration. Same frequency 1 rad/s is used for all three intervals. For as-received CNC, the structural regeneration is almost instantaneous, and G' and G'' in the third interval recovers to similar values as the first interval after it is disrupted by larger shear. (**Figure 3.17a**) The process is reversible indicates that CNC suspensions is thixotropic. The G' and G'' are almost constant in the first and third interval, which suggests that the structural strength does not change over time.

For salt-added CNC, the structural regeneration is also rapid (**Figure 3.17b**) at all the investigated ionic strength. Nevertheless, G' and G'' show different time-dependent

behaviors at different ionic strength, which is related to the salt-induced electrostatic screening and gelation. At 10 mM ionic strength, the G' and G'' are smaller than the G' and G'' of CNC without salt, which suggests that the electrostatic screening dominates the particle interactions. Similar to the decreased viscosity at 10 mM, the electron double layer of the CNC particles are compressed leading to increasing particle mobility. The G' and G'' at 10 mM are also constant over time, indicating that there is no gelation tendency. At 20 mM ionic strength, the G' and G'' at first are also smaller than the moduli of no-salt CNC, but increase slowly over time indicating an early stage of gelation transition. The viscosity test shows that at 20 mM the viscosity is slightly larger than at 10 mM. (**Figure 3.16b**) This slight increase in viscosity confirms that some structural regeneration is already happening at 20 mM. At 25 mM and 30 mM ionic strength, the G' and G'' increases more rapidly. $G' > G''$ in the first interval at 30 mM indicates that the particle interaction has shifted from electrostatic screening to gelation. Overall, the recovery test provides a more in-depth analysis to the salt-induced interactions by probing the time-dependent behaviors. The onset of gelation is at 20 mM as suggested by the recovery test, which is much earlier than at 40 mM suggested by the viscosity test.

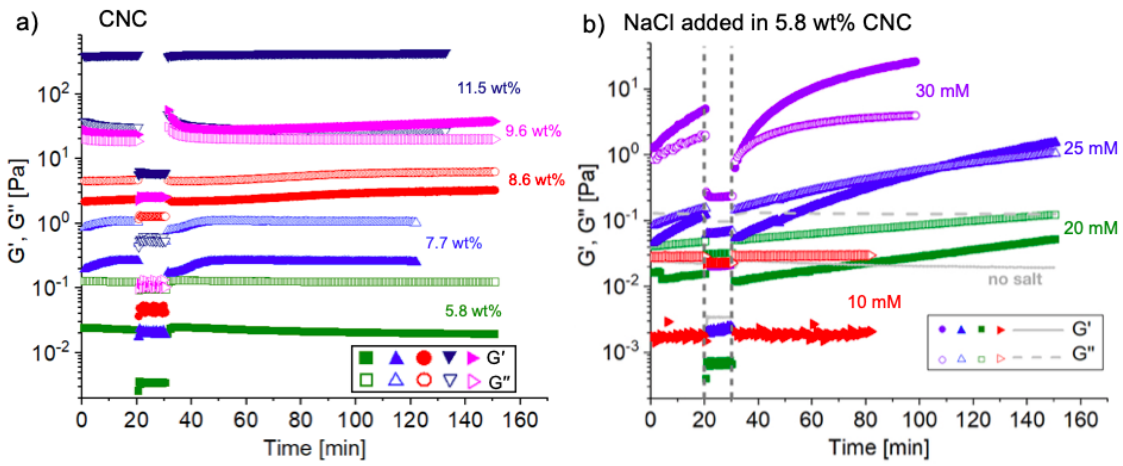

Figure 3.17 The structural reformation is probed by three-interval recovery test for (a) as-received CNC at different concentrations in chiral nematic phase and gel phase and (b) 5.8 wt% as-received CNC of different ionic strength [mM] modulated by adding NaCl.

3.4.7 Temperature Effects on CNC and TEMPO-CNF Suspensions

The viscosities of CNC and TEMPO-CNF suspensions are measured at 25-55 ºC to study the temperature effect. For CNC concentrations in the gel phase (11.5 and 10.5 wt%), the viscosities are almost the same at different temperatures. (**Figure 3.18a**) For concentrations in the chiral nematic phase, the viscosities decrease slightly with increasing temperature at shear rates < 10 s^{-1}. Previous study of temperature effects on CNC have found similar flow curve behavior.[54] Nevertheless, the viscosity difference becomes much smaller when comparing the relative viscosity η_r, which is calculated as $\eta_r = \eta / \eta_{water}$, (**Figure 3.18b**) where η is the measured viscosity and η_{water} is the water viscosity at the corresponding temperature. The η_r difference is more apparent at lower and higher shear rates than at intermediate shear rates. The η_r excludes the effect of water viscosity, thus showing the temperature effect on CNC only.

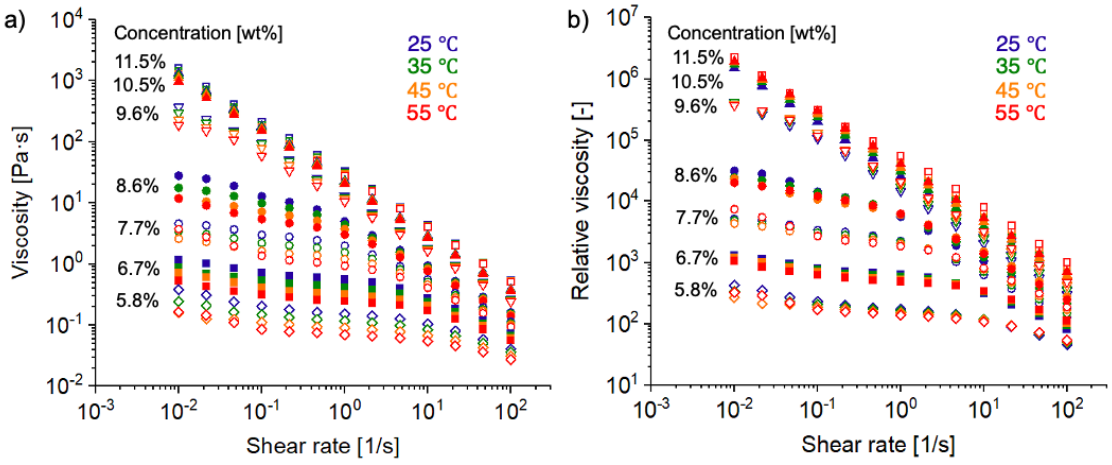

Figure 3.18 (a) Viscosity η and (b) relative viscosity η_r as a function of shear rate for different concentrations of CNC suspensions at different temperatures. The η_r excludes the effect of water viscosity, thus showing the temperature effect on CNC only.

To connect the viscosity change to the CNC interparticle interactions and the shear force, the shear stress versus viscosity is plotted in **Figure 3.19a**. The viscosity difference is again very small at 11.5 and 10.5 wt%, and gradually becomes significant at lower concentrations. However, when η_r is plotted versus shear stress, the η_r collapse onto a single curve at each concentration beyond a shear stress threshold equivalent of 10 s^{-1}. (**Figure 3.19b**) This can be explained by the relative magnitude of intermolecular forces (including charge interaction and hydrogen bonding) and the externally imposed shear force. At low shear stress, where the external force is small, the temperature causes fluctuations of intermolecular interactions, reflected by the viscosity variations at different temperatures. At high shear stress, these fluctuations are diminished by larger shear force, thus η_r variations are reduced and fall onto a single curve.

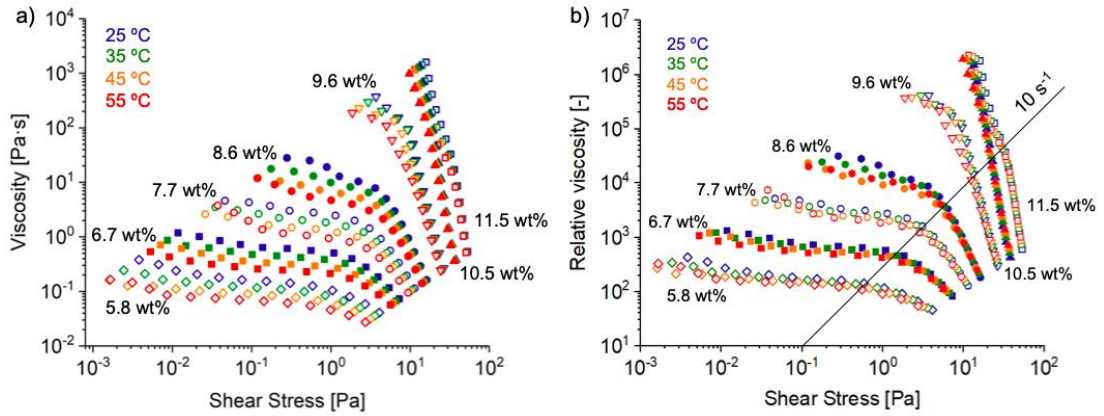

Figure 3.19 (a) Viscosity η and (b) relative viscosity η_r as a function of shear stress for CNC suspensions at different temperatures. The η_r collapse onto a single curve at each concentration beyond a shear stress threshold equivalent of 10 s^{-1}.

The η and η_r of TEMPO-CNF suspensions versus shear stress follow the similar trend. (**Figure 3.20**) The TEMPO-CNF in this temperature study has been pressure homogenized to fibrillate the fibrils, resulting in negative surface charges that help disperse the fibrils to avoid aggregations. The η are different at different temperatures, but all the η_r at different temperatures fall onto a single curve at each concentration. This implies that the intermolecular interactions of the nanofibrils are small compared to the imposed shear force, and are insensitive to the temperature charge when the influence of the water viscosity is excluded. Correlating viscosity with shear stress instead of shear rate has not been explored before at different temperatures for CNC or TEMPO-CNF, but it has been shown to provide an effective scaling for hydroxypropyl cellulose suspension.[128] The study have found that the flow curves at three different temperatures can be reduced to a single master curve when the viscosity is plotted a function of shear stress.

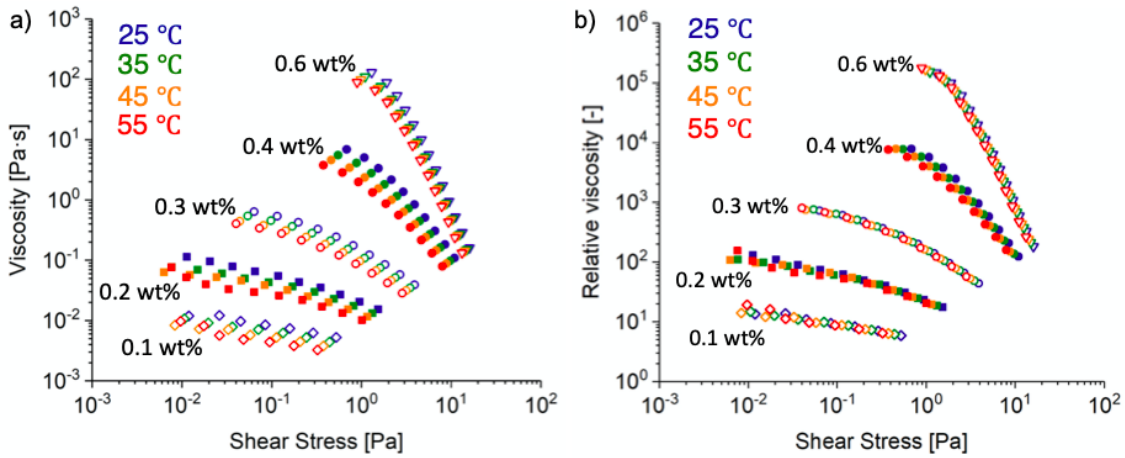

Figure 3.20 (a) Viscosity η and (b) relative viscosity η_r as a function of shear stress for TEMPO-CNF suspensions at different temperatures. All η_r collapse onto a single curve at each concentration.

3.5 Conclusions

In this chapter, we develop detailed preparation and test protocols and measure the rheology of the CNC and TEMPO-CNF suspensions at relevant processing conditions. The protocols ensure accurate and robust rheological results with the ability to distinguish between samples. Both CNC and TEMPO-CNF have higher viscosity at higher concentrations, but the flow curves contain more detailed information about microstructure. When decreasing the concentration, the flow curves of the CNC changes from a single shear thinning in the gel phase, to a three-region shape in the chiral nematic phase, and finally a plateau followed by shear thinning in the isotropic phase. The flow curves of the TEMPO-CNF also show shear thinning at high concentrations, and at intermediate and low concentrations show a Newtonian plateau followed by shear thinning. Frequency sweep are used to identify the phase transition from viscoelastic to gel. Polarized microscopy is used to identify CNC phase transition from isotropic to chiral

nematic, while for TEMPO-CNF the change of scaling of viscosity versus concentration shows the phase transition from isotropic to viscoelastic. The rheology also captures the electrostatic interactions induced by adding external salt. The CNC suspension is very sensitive to the change of the ionic strength modulated by salt. The viscosity first decreases due to electrostatic screening, then increases as attractive forces dominates. Suspensions with monovalent salt NaCl have similar viscosities as the divalent salt $CaCl_2$ before gelation, but the divalent salt induces the gel transition at lower ionic strength. Moreover, the recovery test is able to identify the onset of the gelation more precisely than the viscosity by probing the structure destruction and regeneration. Finally, the temperature effect (25-55 ºC) has insignificant effect on the CNC and TEMPO-CNF viscosities. The test protocols and rheological results in this chapter serve as a reference for the rheological model development and the study on CNM structure-property relationship in the next chapter.

CHAPTER 4. DEVELOPING RHEOLOGICAL MODEL AND PARAMETER FOR QUALITY CONTROL OF CELLULOSE NANOMATERIALS

Parts of the material in this chapter have been published in two manuscripts: J. Liao, K.A. Pham and V. Breedveld, Rheological characterization and modeling of cellulose nanocrystal and TEMPO-oxidized cellulose nanofibril suspensions, *Cellulose* **27** (7), 3741-3757 (2020), DOI: 10.1007/s10570-020-03048-2; and J. Liao, K.A. Pham and V Breedveld, TEMPO-CNF suspensions in the viscoelastic regime: capturing the effect of morphology and surface charge with a rheological parameter, *Cellulose* **28**, 813–827 (2021), DOI: 10.1007/s10570-020-03572-1.

4.1 Introduction

As discussed in Chapter 3.1, a knowledge gap still exists when it comes to translating lab-scale rheological characterization to industry-scale quality control. One challenge is lacking robust rheological test protocols, which are covered in Chapter 3. The other challenge is lacking rheological models and parameters to directly parameterize the results for identification or comparison and will be discussed in this chapter.

Prior studies have used common rheological models to fit the flow curves of cellulose nanocrystal (CNC) at different concentrations, but with limited accuracy in terms of descriptive and predictive power. The power law model has been used to fit the flow curves of CNC concentrations from 1 to 12 wt%. The model fully describes the viscosity behaviors in the gel or Newtonian phase, but it can only capture the shear thinning region

at high shear rates for those in the intermediate concentrations (4 to 9 wt%). [95, 112] Alternatively, the Carreau model has been used to estimate the zero-shear viscosity, but it cannot accurately describe the flow curves with the three-region shape, where shear thinning happens at low shear rates. [101] In spite of the studies relating CNC flow curves to microstructural phases and attempting model fitting, few studies have attempted to address and harness the variability of individual flow curves. In addition to model fitting, viscosity has been used to estimate the aspect ratio (length/diameter) of the CNC particles. The aspect ratio is calculated from the intrinsic viscosity through the Shima equation, with the intrinsic viscosity being estimated through the Fedors equation or the Hugging and Kramer equation. [118, 120, 182] However, concerns have been raised on the validity of using Fedors equation for CNC suspensions. [115] Unfortunately, confirming the accuracy of the aspect ratio estimated from viscosity relative to values measured through other, more direct metrology techniques is challenging. The length and width of CNC particles depend greatly on preparation methods, types of microscopy equipment and human bias, which suffer from large variability. [49]

For TEMPO-CNF rheological studies, in addition to study rheological properties at different concentrations, previous studies have also investigated the effect of morphology and surface charge mainly in either the gel or dilute regime. Here, the gel regime is classified as samples having solid-like behavior, as characterized by $G' > G''$ across a wide range of frequencies. [159, 190, 201, 202] Some previous studies used pressure homogenization to change the nanofibril morphology, and reported that the viscosity of the flow curves increased with higher number of passes through the homogenizer or higher homogenization pressure. [159, 160, 162, 203] Shogren *et al*. reported that G' first

increased until reaching a maximum after the 2nd homogenization pass, followed by decreasing G' as the number of passes was increased further.[163] Changes in surface charge of chemically pretreated CNF also affect its rheology. Specifically, for TEMPO-mediated oxidized CNF (TEMPO-CNF), surface charge has been shown to be correlated with the carboxylate content on the fibril surface, which can be modulated via the amount of oxidation agent and the reaction time. The viscosity (or modulus G') usually decreases with higher carboxylate content. [160, 174] However, the reverse trend has also been reported, [176] and some researchers have reported an initial increase followed by decrease of viscosity as the carboxylate content increases.[190] CNF suspensions in the dilute regime have G' values much smaller than G'' [62] and their steady shear viscosity scales linearly with the concentration. [184] Correlations have been established between the intrinsic viscosity and the aspect ratio of the nanocellulose. [182, 204] Viscoelastic properties of dilute CNF suspensions have also been studied, with G' and G'' used as measures to determine the relaxation time, which in turn can be used to estimate the length of TEMPO-CNF [184] and carboxymethylated CNF fibrils. [161]

However, for CNF in the viscoelastic regime, where it shows liquid-like behavior with $G' < G''$, but also exhibits significant shear thinning in flow curves and power-law scaling of the viscosity (and G') with the concentration, only a few studies have reported rheology data and those studies explored a limited set of concentrations. [154, 161, 173] A systematic investigation on the effect of morphology and surface charge in this regime is lacking. The rheology of CNF in this concentration range is particularly relevant for solution-based processing and applications; for example, CNF suspensions in this concentration range are often used as rheological modifiers and to prepare polymer

composites or hydrogels. Moreover, the current way to report and compare the rheology of CNF at different morphologies or surface charges is not informative. Either the whole data set of many flow curves (viscosity) or oscillatory frequency sweeps (G', G'') across concentrations is presented, which is overwhelming and confusing; or the rheological data is represented by values at only one shear rate or frequency, thus leaving lots of rheological information unused and potentially obscuring important qualitative trends.

In this chapter, we develop a rheological model combining the power law and the Cross model, that accurately captures the viscosities of both CNC and TEMPO-CNF across concentrations and shear rates. One application of this model is that it can be used to estimate the concentration of an uncharacterized CNC or TEMPO-CNF sample by measuring its viscosity relative to a series of characterized samples serving as calibration. The viscosity test is significantly faster than the common gravimetric method to determine the dry content of a suspension, which is relevant for quality control. The model can also fit the flow curves of CNC at different salt concentrations, showing the potential to be used in quality control to estimate the salt concentrations. For TEMPO-CNF of different morphologies and surface charges, we show that the scaling of the model fit parameters and the concentration can be used to define a rheological "flow index" parameter. This index is suitable for effectively distinguishing TEMPO-CNF samples of different morphologies and surface charges, condensing the entire family of flow curves of TEMPO-CNF samples at multiple concentrations into a single parameter value. The flow index thus represents the sample's rheological properties more comprehensively and robustly, and can be considered as a rheological fingerprint of a TEMPO-CNF sample of a specific morphology or surface charge condition. It establishes a clear and concise one-to-one

relationship between TEMPO-CNF rheological properties and fibril characteristics, which can be used for quality control and/or benchmarking of cellulose nanomaterials.

4.2 Materials and Methods

The preparations of samples at various concentrations followed the preparation protocol in Chapter 3.2.3. The rheological measurement followed the test protocol developed in Chapter 3.3, except that the bottom plate insert of 50mm was used the measure the viscosity of low concentration TEMPO-CNF suspensions (< 0.1 wt%). The FE-SEM images were taken followed the procedure in Chapter 3.2.6.

4.2.1 Materials

Cellulose nanocrystals (CNC) at concentration of 12.1 wt%, cellulose nanofibril (CNF) (Lot # U-44) at 3 wt% and TEMPO-CNF (Lot # 2018-FPL-CNF-121) at 1.1 wt% were purchased in slurry form from the Process Development Center at the University of Maine. TEMPO ((2,2,6,6-tetramethylpiperidin-1-yl)oxyl) free radical (98%) was obtained from Alfa Aesar (Ward Hill, MA); sodium hypochlorite (NaClO) (14.5% available chlorine in water) from Beantown Chemical (Hudson, NH), sodium hydroxide (NaOH of 3M concentration), sodium chloride (NaCl), sodium bromide (NaBr), hydrochloric acid (HCl of 1M concentration) and dialysis tubing (14,000 MW cutoff) were purchased from Ward's Science (Rochester, NY). The gold-coated silicon wafer for SEM imaging was obtained from Angstrom Engineering Inc. (Kitchener, Canada) The procedure to obtain dialyzed CNC (dia-CNC-1) was described in Chapter 3.2.4.

4.2.2 Preparation of TEMPO-CNF Samples with Different Morphologies

TEMPO-CNF samples with different morphologies are prepared by pressure homogenizing the purchased TEMPO-CNF suspension without chemical modification in a Mini DeBEE homogenizer (BEE International, South Easton, MA) using a 0.2 mm nozzle. The feeding concentration is kept around 0.5 wt%; fiber suspensions of higher concentration will clog the nozzle. The sample after homogenization is characterized directly without further treatment. The homogenization pressure values for this study were 8000 psi ("low"), 15000 psi ("medium") and 25000 psi ("high"), and samples were homogenized for 1, 2, 3, 5 and 7 passes at each pressure (**Table 4-1**). The size of the fibrils varies greatly, and the length and width of the fibrils are notoriously difficult to measure accurately. For example, microscopy techniques suffer from measurement bias, and many factors during the specimen preparation step such as fibril dispersion, drying, and substrate condition all affect the imaging result. [197, 205] Therefore, in this study the morphology of each sample is represented by its homogenization condition instead of estimates of fibril length and width. Each sample is labeled with pressure and the number of passes to indicate its homogenizer treatment. For example, MP-5 denotes a sample that is homogenized at medium pressure of 15000 psi for 5 passes. The pressures were chosen because 8000 and 25000 psi are the minimum and maximum pressure attainable with the equipment. The surface charge of the TEMPO-CNF after pressure homogenization is quantified by conductometric titration, which is discussed in the following section. The surface charges are around 1.3 ± 0.1 mmol/g for all pressure homogenized samples, slightly higher than the as-received TEMPO-CNF, which has a surface charge of 1.1 mmol/g.

Table 4-1 Nomenclature of TEMPO-CNF samples with different morphologies that were produced by pressure homogenization of the purchased TEMPO-CNF without chemical modification. The carboxylate content of these samples is 1.1 ± 0.1 mmol/g.

	Pressure [psi]	**Number of passes**	**Label**
Low	8,000	1, 2, 3, 5, 7	LP-1, 2, 3, 5, 7
Medium	15,000	1, 2, 3, 5, 7	MP-1, 2, 3, 5, 7
High	25,000	1, 2, 3, 5, 7	HP-1, 2, 3, 5, 7

4.2.3 Preparation of TEMPO-CNF Samples with Different Surface Charges

TEMPO-CNF samples with three different surface charges were produced via TEMPO mediated oxidation of the purchased CNF following a previously reported procedure with slight modifications. [70, 188] 150 g of 3 wt% CNF slurry was diluted with DI water to reach a total mass of 400 g. The mixture was stirred for 30 minutes. TEMPO-CNF of three different carboxyl contents (low, medium high) was produced by adding 0.08 g TEMPO free radical and 0.5 g NaBr, and the pH of the suspension was adjusted to 10.5 by adding 1M NaOH solution. Subsequently, 60 (low), 80 (medium) and 100 mL (high) of NaClO (3 wt% available chlorine) was added dropwise. The suspension pH was monitored and adjusted to remain around 10 by dropwise adding 0.5 M NaOH aqueous solution as needed. The reaction was considered finished once the pH did not change for 10 minutes, and methanol was then added to the suspension to consume excess NaClO. The total reaction time was around 0.8 (low surface charge), 1 (medium) and 6 (high) hours, respectively. The suspension was centrifuged (12,000 x *g*) and washed with DI water three times. The centrifuged samples were then diluted with water to reach around 0.5 wt% and pressure homogenized at 25000 psi for 7 passes to ensure similar morphologies to the

samples described in the previous section. After homogenization, the chemically modified TEMPO-CNF samples have relatively low viscosities, making it difficult to further dilute the sample and still study viscosity at multiple concentrations in the viscoelastic regime. Thus, the samples were concentrated through rotatory evaporation at low temperature (35 °C) to around 1.5 wt%. A known problem of rotary evaporation is that it can cause irreversible fibril aggregation. Nevertheless, by using relatively low evaporation rates, the negative impact of evaporation was found to be greatly reduced, as indicated by good reproducibility and absence of visible large aggregates. The surface charge was determined by the conductometric titration [77] and quantified in terms of the carboxylate content: 1.4 ± 0.1 (low), 1.6 ± 0.1 (medium), and 2.0 ± 0.1 (high) mmol/g.

4.3 Results and Discussions

4.3.1 Rheological Model Capturing Viscosities of CNC Suspension

Previous studies have used the power law model ($\eta = a\dot{\gamma}^{-b}$) to capture only the shear thinning part of the flow curve at each concentration. [95, 112], but are not able to capture the complete shape of the curve. Furthermore, the arbitrariness of determining which data points to include, especially in the case of the three-region flow curves, affects the accuracy and reproducibility of the reported power-law parameters. The Cross model ($\eta = \eta_\infty + \frac{\eta_0 - \eta_\infty}{1+(\lambda\dot{\gamma})^m}$) has been used to capture the flow curves in the isotropic and the chiral nematic phase, [101] but the model fails to capture the shear thinning at low shear rates for samples in the chiral nematic phase. Therefore, a model is needed to accurately capture the flow curves across the full range of shear rates and concentrations.

We propose that the viscosity behavior of CNC at all concentrations can be described by a model that combines the power law and the Cross model, which each describe its viscosity behaviors at different shear rates (*i.e.* timescales):

$$\eta = a\dot{\gamma}^{-b} + \eta_\infty + \frac{\eta_0 - \eta_\infty}{1+(\lambda\dot{\gamma})^m} \quad (4\text{-}1)$$

In Equation 1, $\dot{\gamma}$ is the shear rate and η the viscosity. For the power law term, a represents the magnitude of the viscosities, and b the extent of shear thinning (acceptable values of b are between 0 and 1). For the Cross model term, η_0 is the viscosity at zero shear rate. η_∞ represents the viscosity in the limit of very high shear rate (fixed at 0.00089 Pa·s, the water viscosity at 25 °C), [206] m is the slope of the curve in the shear thinning region, and λ is associated with the ruptured of structural linkages[207] with $1/\lambda$ indicating the characteristic shear rate of the onset of shear thinning. All parameters (a, b, η_0, λ, m) are fitted using OriginLab with a weighing factor of $1/y^2$ using the Levenberg-Marquardt algorithm. The weighing factor $1/y^2$ is chosen because the viscosity at higher shear rates is inherently more reliable than those at lower shear rates, as indicated by the smaller standard deviations of the viscosity data points. For the flow curves in the gel phase, the power law term alone in the combined model can capture its single shear thinning behavior; for those in the isotropic phase, the Cross model term can describe the plateau followed by shear thinning. In the chiral nematic phase, both terms are needed to describe the three-region shape. The terms in the combined model that are needed to properly fit the data can be selected through an automated model choice procedure, which is discussed the section below.

4.3.1.1 Model Fitting for As-received CNC Suspensions

The viscosity data points with the fitted curves across all concentrations are shown in **Figure 4.1**. The fit parameter values for all concentrations are listed in **Table 4-2**. The standard deviation of most parameters is within 20% across concentrations. The combined model accurately captures the complex behaviors across the concentrations and shear rates, and it holds rheological meaning. Different regions of one flow curve are all accurately described by a single model, and this combined model works for all concentrations ranging from isotropic to gel phase.

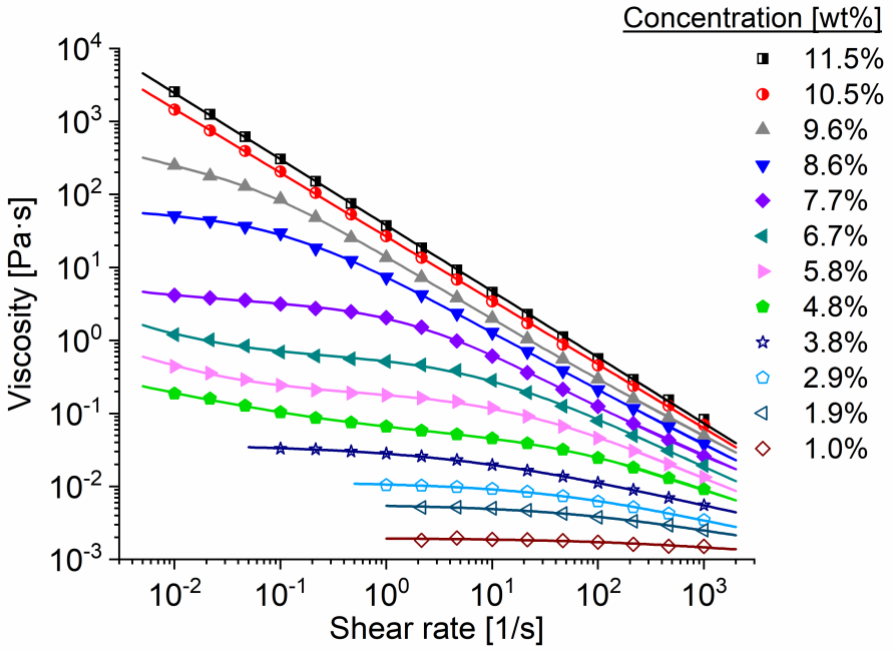

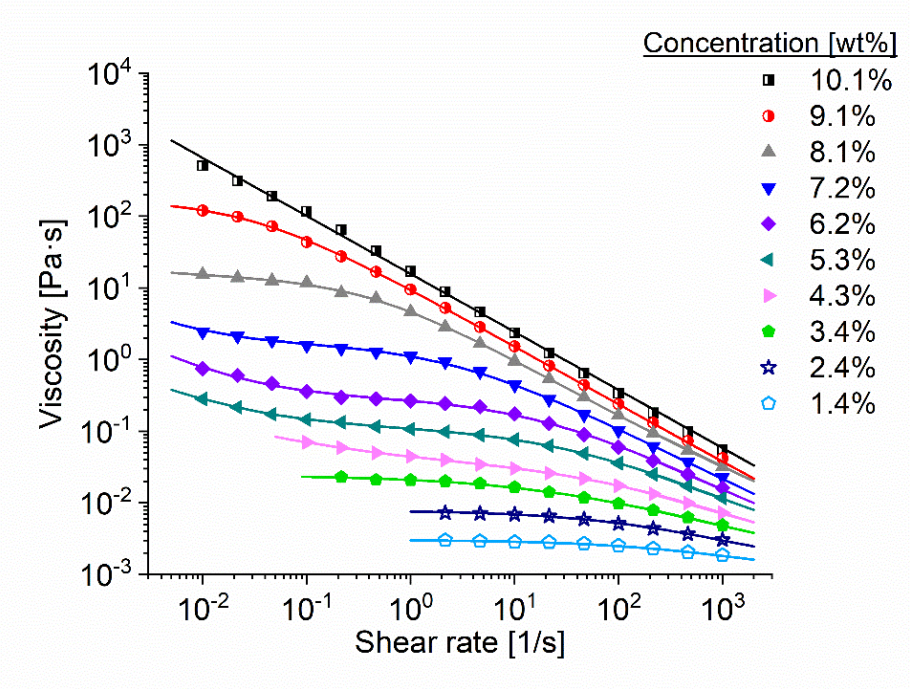

Figure 4.1 Flow curves of CNC from 1.0 to 11.5 wt% with model fitting results (solid lines) using the power law model, the combined model and the Cross model. The data is presented in two figures for clarity.

Table 4-2 Parameter values obtained by fitting the combined model (Equation 1) to the flow curves for all investigated CNC concentrations.

Concentration [wt%]	*a*	*b*	η_0	λ	*m*
1	/	/	$(1.97 \pm 0.06)\cdot10^{-3}$	$(0.60 \pm 0.18)\cdot10^{-3}$	0.61 ± 0.20
1.4	/	/	$(3.07 \pm 0.05)\cdot10^{-3}$	$(1.49 \pm 0.14)\cdot10^{-3}$	0.57 ± 0.05
1.9	/	/	$(5.44 \pm 0.15)\cdot10^{-3}$	$(1.53 \pm 0.20)\cdot10^{-3}$	0.58 ± 0.07
2.4	/	/	$(7.95 \pm 0.16)\cdot10^{-3}$	$(4.34 \pm 0.44)\cdot10^{-3}$	0.56 ± 0.03
2.9	/	/	$(11.45 \pm 0.21)\cdot10^{-3}$	$(9.02 \pm 0.90)\cdot10^{-3}$	0.52 ± 0.02
3.4	/	/	$(24.36 \pm 0.54)\cdot10^{-3}$	$(26.3 \pm 3.4)\cdot10^{-3}$	0.48 ± 0.02
3.8	/	/	$(37.73 \pm 0.40)\cdot10^{-3}$	$(89.8 \pm 5.7)\cdot10^{-3}$	0.432 ± 0.005
4.3	0.013 ± 0.003	0.45 ± 0.06	0.033 ± 0.003	0.013 ± 0.003	0.59 ± 0.02
4.8	0.026 ± 0.003	0.38 ± 0.02	0.042 ± 0.004	0.012 ± 0.002	0.69 ± 0.04
5.3	0.009 ± 0.001	0.64 ± 0.03	0.111 ± 0.003	0.034 ± 0.002	0.635 ± 0.009
5.8	0.013 ± 0.005	0.65±0.07	0.19 ± 0.01	0.056 ± 0.008	0.67 ± 0.02
6.2	0.017 ± 0.009	0.74 ± 0.12	0.28 ± 0.02	0.064 ± 0.014	0.70 ± 0.03
6.7	0.024 ± 0.021	0.69 ± 0.16	0.61 ± 0.06	0.14 ± 0.03	0.71 ± 0.02
7.2	0.03 ± 0.02	0.80 ± 0.31	1.64 ± 0.14	0.40 ± 0.07	0.73 ± 0.01
7.7	0.20 ± 0.02	0.41 ± 0.01	2.92 ± 0.12	0.57 ± 0.05	0.84 ± 0.02
8.1	0.27 ± 0.12	0.46 ± 0.04	13.55 ± 2.47	2.47 ± 0.36	0.84 ± 0.02
8.6	0.43 ± 0.40	0.53 ± 0.08	52.59 ± 7.85	9.72 ± 1.94	0.83 ± 0.02
9.1	/	/	172.78 ± 34.52	34.53 ± 3.57	0.81 ± 0.01
9.6	3.86 ± 0.98	0.69 ± 0.02	191.66 ± 21.05	21.05 ± 5.15	0.95 ± 0.03
10.1	15.71 ± 0.48	0.81 ± 0.01	/	/	/
10.5	26.50 ± 0.28	0.87 ± 0.003	/	/	/
11.5	37.92 ± 0.43	0.90 ± 0.003	/	/	/

The combined model parameterizes the viscosity dataset, condensing a flow curve to a few parameters. One can compare different flow curves using the parameters, rather than selectively picking viscosity values at specific, arbitrary shear rates. Among the parameters, η_0 and λ scale strongly with the CNC concentrations, covering both the Cross model and the combined model (**Figure 4.2**). The error bars of the fit parameters η_0 and λ

are small, and two regimes are observed for η_0 and λ with a threshold of 4.3 wt%, where the model switches from the Cross model to the combined model. Both η_0 and λ increase monotonously within each regime as the concentration increases. 4.3 wt% is also the critical concentration from isotropic to chiral nematic phase. (**Figure 3.4 in Chapter 3**) In a previous study, the CNC viscosity at various shear rates was plotted from 0.5 to 8 wt% and that study showed two regimes where the transition happened at around 3 wt%.[105] A linear fit can be used to correlate $\log_{10} \eta_0$ and $\log_{10} t$ to the concentration in each regime (**Figure 4.2)**, with the equations summarized in **Table 4-3**. These equations can be used to estimate concentrations of unknown CNC suspensions, as discussed in the following section. The data points of $\log \eta_0$ and $\log \lambda$ versus concentration have been attempted to fit with 2nd order polynomial equations. Although the polynomial curve visually looks better than the linear fit, all three fitted parameters have standard deviations at least 50% of the fitted values, with one parameter having the value of standard deviation larger than the fitted value. Thus, fitting with 2nd order polynomial equations cannot be justified.

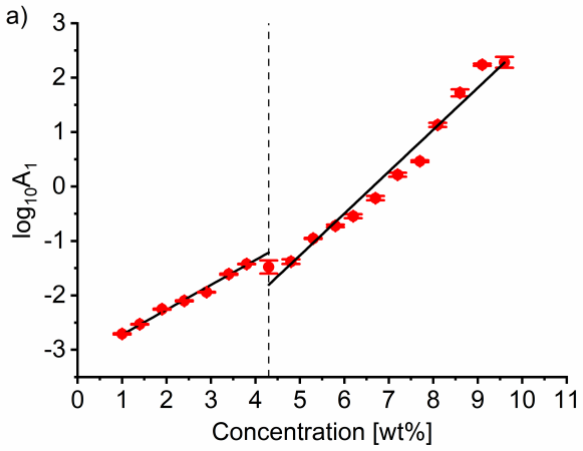

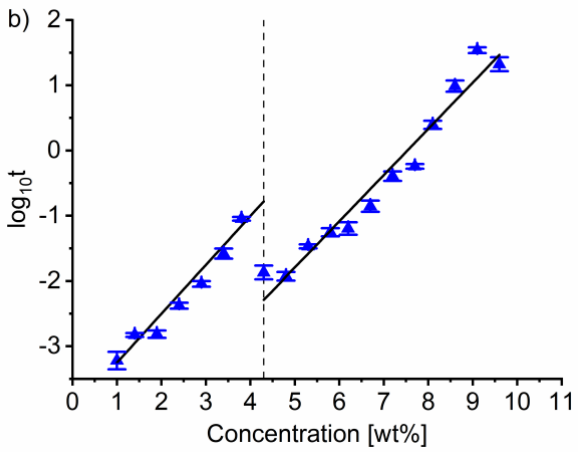

Figure 4.2 Linear fit of a) *log* η_0 and b) *log* λ versus concentration in two regimes: 1.0 to 4.3 wt% and 4.3 to 9.6 wt%. The transition happens at 4.3 wt%.

Table 4-3 Linear correlations of *log* η_0 and *log* λ versus concentration (abbreviated as conc) for CNC.

Concentration	Model	η_0	λ
1.0 - 4.3 wt%	Cross	$log\ \eta_0 = 0.457 \cdot conc - 3.177$	$log\ \lambda = 0.749 \cdot conc - 3.999$
4.3 - 10 wt%	Combined	$log\ \eta_0 = 0.770 \cdot conc - 5.115$	$log\ \lambda = 0.709 \cdot conc - 5.359$

Combing the power law and Cross model into one model is not common in the rheological literature, but precedent exists in the small-angle neutron scattering (SANS) literature. The intensity curves observed for peptide hydrogels have similar three-region shapes, and the empirical equation ($I(Q) = A/Q^n + C/[1 + (QC)^m] + B$) has successfully been used to fit the intensity curve across a wide range of length scales; that equation is intrinsically the same as our combined viscosity model.[208] The two terms in the SANS model quantify the hydrogel network morphology at two distinct length scales. The first term A/Q^n is similar to Porod-like scattering in either X-ray or neutron small-angle scattering, dominating the larger length scale.[209] The $C/[1 + (QC)^m] + B$ term, a Lorentzian function, reflects the polymer/solvent interaction at smaller length scale. Both

length scales match what is observed in CNC, where large length scale relates to the domains of CNC particles, and small length scale to the individual CNC particles. Moreover, the shear-induced microstructural change is investigated using RheoSANS by Haywood *et al.* on CNC in biphasic concentrations.[104] SANS of various CNC concentrations also show similar three-region curves, and both shear thinning regions are more apparent in SANS than in viscosity measurement, confirming the underlying microstructural change. RheoSANS measurements show that the order parameter increases at low and high shear rates, while plateaus at intermediate shear rates. This suggests that viscosity change per shear rate is due to the alignment of the CNC particles, consistent with the hypothesis from previous viscosity studies.[54] Moreover, the onset of the second shear thinning can be calculated as $1/\lambda$ from the λ in the Cross model term. The values of $1/\lambda$ compared with the ones listed in Haywood's study are of similar magnitude. The difference may be because they use the freeze-dried CNC in D_2O, while this study uses never-dried slurry CNC in DI H_2O, which will result in different flow curves, thus different λ at the same concentrations.

Another concern is that the number of viscosity data points to fit the model is too small. It may be argued that fitting a model with 5 unknowns using 16 points or fitting a model with 3 unknowns using 10 points runs the risk of underfitting. To test this concern, the flow curves at 4.8 wt% and 2.9 wt% are fitted with a total number of points of 26 and 16 data points, respectively. When constants η_0 and λ are derived from flow curves with 26 points the standard deviation does not differ from flow curves with 16 points, indicating that decreasing the number of data points does not affect the quality of the data fitting. Hence, the proposed combined model not only accurately captures the viscosity behaviors

throughout concentrations and across shear rates, but also holds rheological meaning with regards to microstructural changes.

4.3.1.2 Model Fitting for Dialyzed CNC Suspensions

We measured the viscosity of salt-free CNC (dia-CNC-1) to study the flow curve across concentrations in Chapter 3 (**Figure 3.12**). Here, we investigated whether the model fitting and viscosity analysis procedure of the as-received CNC discussed in the previous section still apply to the dialyzed CNC. **Figure 4.3** shows the same set of flow curves as in **Figure 3.12** and these curves can also be fitted by the combined model. At low concentrations (0.75 - 2.25 wt%), the flow curves can be fitted using the Cross model term; at intermediate concentrations (3.0 and 3.75 wt%), fitted by both terms in the combined model and fitted by the power law term at high concentrations (4.5 – 9.0 wt%). For the flow curves that could be fitted with the power law, the fitted parameter a and concentrations show a strong linear correlation (a = 13.1 • concentration – 49.3, R^2 = 0.99). The correlation shows its potential to use power law to accurately estimate unknown concentrations for CNC highly concentrated, which fill the gap as the as-received CNC have few concentrations that are fitted by power law.

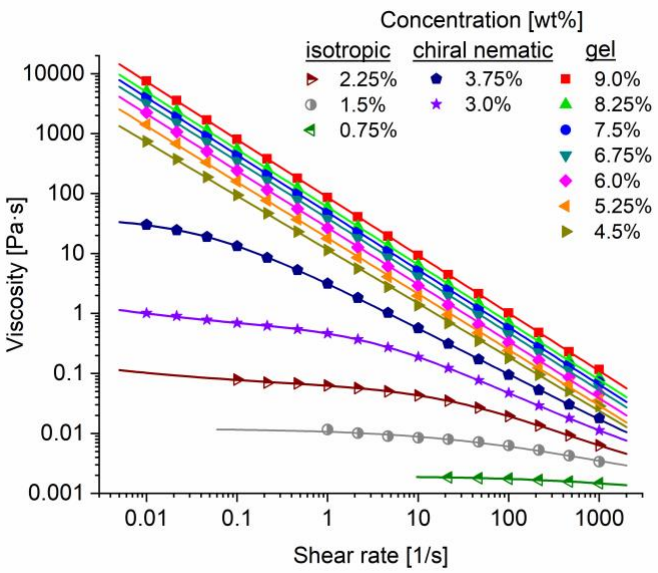

Figure 4.3 Flow curves of dialyzed CNC denoted as dia-CNC-1. The solid lines represent model fitting results using the power law model, the combined model and the Cross model.

4.3.2 Application of the Combined Model: Estimating Concentrations of Unknown CNC Samples

The gravimetric method is commonly used to determine the dry content of a nanocellulose sample. Oven drying time typically takes at least 3 hours, which is not ideal for quality control requiring rapid feedback. Meanwhile, a rheology test usually can be done in 30 minutes or less, depending on the shear rate range and the number of acquisition points. Thus, it would be useful to have a rheology-based method to determine the dry content of CNC samples for quality control purposes. A procedure (**Figure 4.4**) is established to estimate the concentration of an unknown CNC sample by only measuring its shear viscosity. First, the viscosity of a given sample is measured following the test protocol. Then, the appropriate viscosity model is chosen either by visually observing the shape of the flow curve, or more objectively, by following a decision tree. The latter

approach will be discussed shortly. Next, the flow curve is fitted with the proper terms of the combined model by OriginLab to obtain η_0 and λ. Finally, the concentration is calculated from η_0 and λ separately using the correlations in **Table 4-3**, and the final concentration reported for the sample is the average of these two calculated concentration values.

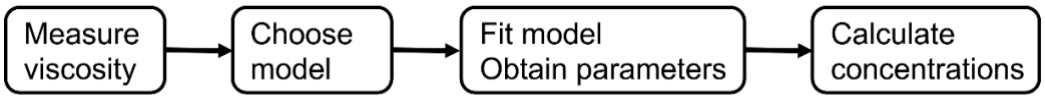

Figure 4.4 Flow chart of the general steps used to determine the concentration of a given CNC sample based on viscosity measurement.

Choosing the proper terms in the combined model to fit the flow curve would be easy if the curve has the shape of a single shear thinning (high concentrations), or almost flat across shear rates (low concentrations): the former can be fitted by the power law, and latter one by the Cross model. The difficulty lies in choosing the Cross model term or both terms at intermediate concentrations. Thus, a decision tree is proposed to guide the model choice process without subjective operator interference. (**Figure 4.5**) The flow curve of *m* data points is first fitted to equation $y = k \cdot x^{-n}$, obtaining parameters k_1 and n_1. Then, the last viscosity data point (the viscosity at the highest shear rate) is eliminated from this flow curve. The remaining *m-1* points are fitted again to $y = k \cdot x^{-n}$, obtaining the second sets of the parameters k_2 and n_2. The procedure is repeated, each time eliminating the last data point of the curve and fitting the remaining flow curve to $y = k \cdot x^{-n}$ to obtain k_i and n_i, until 6 points left. In this way, a list of *k* and *n* values are generated for each concentration. The maximum and minimum values of *k* and *n* at each concentration are noted as k_{max}, k_{min}, n_{max}, and n_{min}. The values of *k* and *n* remain almost unchanged for samples in the gel phase,

as eliminating points will not affect the slope and pre-exponent value of a power-law shear thinning curve. For samples in the chiral nematic phase, however, *k* will keep increasing with fewer number of points, as the viscosity is higher at lower shear rates, while *n* will first decrease with the elimination of the second shear thinning region, then increases as the first shear thinning region dominates. For samples in the isotropic phase, *k* will keep increasing, and *n* decreasing, then both *k* and *n* approach a plateau, as the shear thinning is eliminated and left with the plateau region. The relative values of *k* and *n* at different concentrations also indicate the different phases that the flow curves belong to. Since *k* either increases or remains the same for each concentration, k_{max} reflects the highest level of viscosity it can reach. As a result, samples in the gel phase will have the largest k_{min}, and samples in the isotropic phase will have the smallest k_{max}.

Based on the trends of *k* and *n* for CNC from 1.0 to 11.5 wt%, a decision tree is generated to guide choosing the proper terms in the combined model to fit the flow curve. If the maximum value of *k* is smaller than 0.04, then the viscosity data should be fitted with the Cross model. Otherwise, if the minimum value of *k* is smaller than 10, it should be fitted with the combined model. If neither condition is met for *k*, the difference between the maximum and minimum of *n* is calculated. If the difference is smaller than or equal to 0.2, then the viscosity data should be fitted with the power law term. Otherwise, it should still be fitted with the combined model.

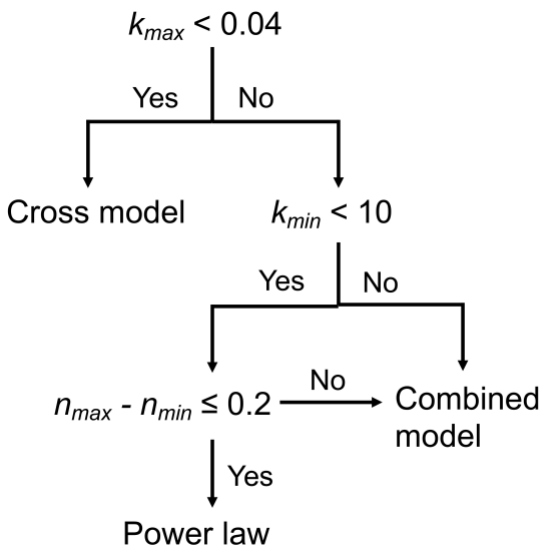

Figure 4.5 Decision Tree to Guide the Model Choice for Data Fitting of the CNC Flow Curves.

Table 4-4 shows the actual concentrations and the estimated concentrations (in wt%) with standard deviations based on fitted values of η_0 and λ following the outlined procedure. The first two columns show η_0 and λ obtained from the model fitting. The third and fourth columns are the estimated concentrations based on η_0 and λ. The fifth column is the average estimated concentration calculated from the average of the third and the fourth column. The errors in preparing the actual samples through dilution from the stock are less than 0.003 wt%, which is negligibly small. The estimated concentrations are very close to the actual concentrations. This implies that the sample preparation, viscosity measurement, model choice procedures and data analysis are reliable. Once calibration curves of η_0 and λ versus concentrations are established for a CNC product, one can use this method to quickly check whether the concentration of CNC deviates from the normal value in a quality control test.

Table 4-4 Estimated CNC concentrations (in wt%) based on parameters η_0 and λ from the combined model and the Cross model; the "actual" concentration value in the final column is based on dilution from the well-characterized stock solution.

η_0	λ	wt%, estimated from η_0	wt%, estimated from λ	wt% Average	wt% Actual
0.048 ± 3E-4	0.013 ± 0.002	2.88 ± 0.05	2.84 ± 0.17	**2.9 ± 0.1**	**3.0**
0.048 ± 0.001	0.120 ± 0.016	4.07 ± 0.05	4.11 ± 0.17	**4.1 ± 0.1**	**4.0**
0.091 ± 0.003	0.026 ± 0.003	5.29 ± 0.04	5.30 ± 0.15	**5.3 ± 0.1**	**5.5**
0.237 ± 0.024	0.063 ± 0.015	5.83 ± 0.13	5.83 ± 0.34	**5.8 ± 0.2**	**5.9**
0.999 ± 0.074	0.241 ± 0.041	6.64 ± 0.10	6.66 ± 0.24	**6.7 ± 0.2**	**6.9**
5.914 ± 0.282	1.193 ± 0.105	7.67 ± 0.06	7.65 ± 0.12	**7.7 ± 0.1**	**7.9**

Predicting the concentration becomes challenging if the concentration falls near the transition concentration (4.3 wt%) or above 9.6 wt%. This would be resolved by applying a known dilution step to the original sample and measuring the diluted sample again. For example, if the measured flow curve has a single shear thinning shape or the power law model is indicated by the decision tree to fit the data, this implies that the sample concentration lies above the upper concertation in the calibration and requires dilution. Such a procedure would remove any ambiguity that may arise from the non-monotonic shape of the flow curves. One way to estimate the concentration is to use the parameter *a* from the power law to interpolate. Although the result is reasonably good, with a predicted concentration of 10.0 ± 0.1 wt% versus an actual concentration of 10.2 wt%, few points (10.1, 10.5 and 11.5 wt%) are available to construct a linear fit between parameters *a* and *b* and sample concentration. Hence, another sample is prepared by diluting the original 10.2 wt% to 5.1 wt%. The same procedure is followed to predict the diluted sample, leading to a predicted concentration of 4.8 ± 0.2 wt%. This leads to a predicted original concentration of 9.6 ± 0.4 wt% versus actual 10.2 wt%. The difference might be caused by error propagation during the dilution step. Although the correlations and the corresponding concentration range are materials-specific, the generic procedures will still work. Using

fewer concentrations to establish a correlation between η_0 or λ versus concentration will not reduce the prediction accuracy, but the correlation will be less robust, as one error will affect the fit more significantly with fewer points.

Moreover, the same criteria in the decision tree (**Figure 4.5**) can be used to choose the appropriate model. This implies again that dialyzed CNC is not intrinsically different from the as-received CNC.

4.3.3 Application of the Combined Model: Estimating Salt Concentrations in CNC Samples

The viscosity change induced by adding NaCl to the CNC suspensions is discussed in Chapter 3.4.6. The viscosity reaches a minimum at around 20 mM ionic strength and the phase transition to gel happens at around 40 mM where the viscosity increases significantly. The Cross model is used to fit the flow curves at ionic strength of 0.5 mM to 25 mM, where the electron double layer is compressed but the suspension not yet reaches gelation. **Figure 4.6** shows the fitting result of η_0 and λ versus ionic strength for the dia-CNC-2 samples. Both parameters decrease at first, reach the minimum at 20 mM, and then increase following the same trend as the viscosity. Though this trend could not easily be parameterized by a simple model fit like is done in **Figure 4.2**, the data could still be useful in quality control to estimate the salt concentration in CNC suspensions.

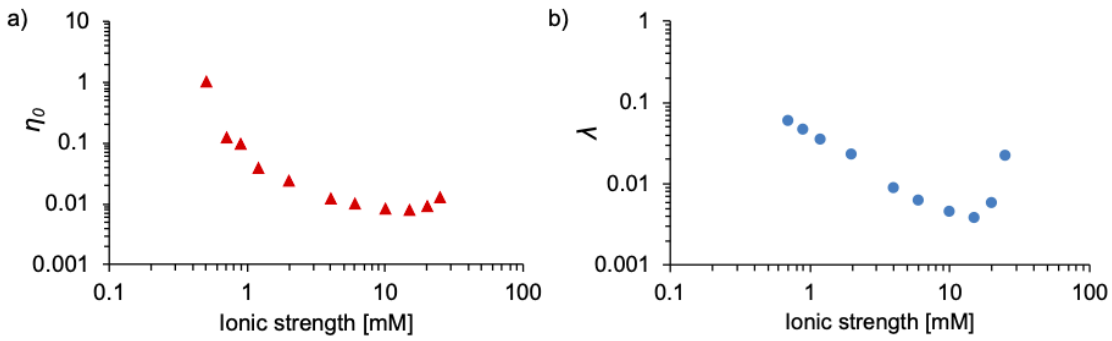

Figure 4.6 Values of parameters c) η_0 and d) λ obtained from the Cross model for 4.0 wt% dia-CNC-2 at various ionic strengths before phase transition occurs.

4.3.4 Rheological Model and Concentration Estimation for TEMPO-CNF

To investigate the applicability of the combined model to other nanocellulose materials, TEMPO-CNF (pressure homogenized at 25000 psi for 7 passes) is chosen to perform viscosity measurements. **Figure 4.7** shows TEMPO-CNF viscosity for concentrations from 0.2 to 2.4 wt%. Every data point on the flow curve is calculated by averaging the three intervals of each test as specified in the Methods section. No significant sign of wall slip is observed (**Figure 3.11**). The flow curve of 2.4 wt% is fitted with the power law ($\eta = a\dot{\gamma}^{-b}$), and the Cross model ($\eta = \eta_\infty + \frac{\eta_0 - \eta_\infty}{1+(\lambda\dot{\gamma})^m}$) is used to fit the flow curves of the remaining concentrations. Similarly, η_0 is the viscosity at zero shear rate; η_∞ is fixed at 0.00089 Pa·s; m represents the slope of the curve in the shear thinning region, and λ is the characteristic time. Since TEMPO-CNF consists of flexible fibers, no chiral nematic region is observed, so there is no shear thinning at the low shear rates prior to gelation. Thus, the Cross model term in the combined model sufficiently captures the concentrations where viscosity plateaus at low shear rates followed by shear thinning at high shear rates. This shape of TEMPO-CNF flow curves is rarely seen in previous studies, [190, 194] probably because the TEMPO-CNF used in this study has high surface charges

(1.6 ± 0.1 mmol/g) and was pressured homogenized, where stronger repulsion between fibrils improves the dispersion.

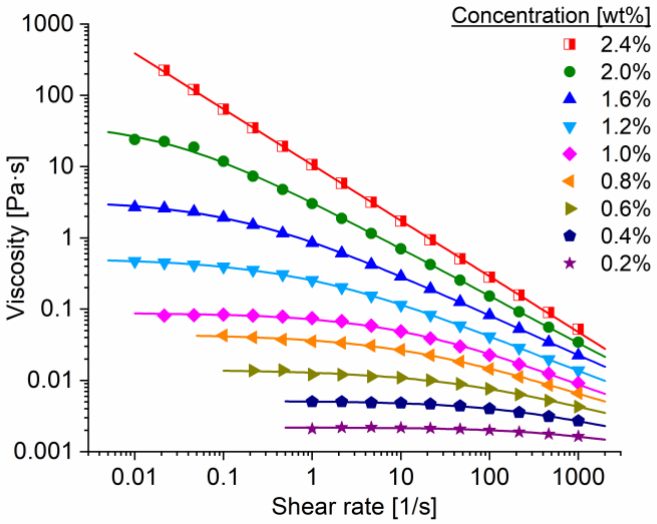

Figure 4.7 Viscosity of TEMPO-CNF suspensions. The solid lines represent model fitting to the power law model (for half-closed symbols) and the Cross model (for closed symbols).

The same procedure presented in Chapter 4.3.2 is used to obtain the fitting parameter values of η_0 and λ, so that a linear fit can be performed to get the correlations between log η_0 and log λ versus concentration (**Figure 4.8**), which are summarized in **Table 4-5**. The viscosities of 0.9 and 1.4 wt% TEMPO-CNF samples are then measured separately. The estimated concentrations from both η_0 and λ are almost identical to the actual concentrations, as shown in **Table 4-6**. This implies that the model also provides an accurate way to estimate the concentration of TEMPO-CNF samples based on viscosity measurements, which may be expanded to use for other cellulose nanomaterials.

Table 4-5 Linear correlations of *log* η_0 and *log* λ versus concentration for TEMPO-CNF.

Concentration	Model	η_0	λ
0.2 - 2 wt%	Cross	$log\ \eta_0 = 2.389 \cdot conc - 3.247$	$log\ \lambda = 2.765 \cdot conc - 3.689$

Table 4-6 TEMPO-CNF concentrations (in wt%) determined from Cross model parameters, estimated concentrations based on η_0 (the third column), estimated concentrations based on λ (the forth column); the "average" concentration is the average of concentrations estimated from η_0 and λ; the "actual" concentration value in the final column is based on dilution from well-characterized stock solution.

η_0	λ	**wt%, estimate from η_0**	**wt%, estimate from λ**	**wt% average**	**wt% actual**
0.06 ± 0.002	0.06 ± 0.01	0.85 ± 0.01	0.89 ± 0.04	**0.87 ± 0.03**	**0.9**
1.73 ± 0.021	3.75 ± 0.17	1.46 ± 0.005	1.54 ± 0.02	**1.50 ± 0.01**	**1.4**

4.3.5 TEMPO-CNF of Different Morphologies

The morphology of TEMPO-CNF is changed by passing the 0.5 wt% suspension through the pressure homogenizer. This specific concentration is chosen to prevent clogging the nozzle of the pressure homogenizer during the process, and allows us to readily measure viscosity at multiple lower concentrations by further diluting the homogenized sample. **Figure 4.8** shows the SEM images of samples subjected to high pressure 25000 psi homogenization for 0, 1, 3 and 7 passes. Without homogenization, the majority of the fibrils are less than 5 μm in length. The unhomogenized suspension contains some larger non-fibrillated fragments (**Figure A.2 and A.3** in Appendix A); however, the aggregates are not large enough and not concentrated enough to affect the rheological measurements in the cone-plate geometry. After 1 pass, most of the fibrils were reduced to around 3 μm length and the samples appear more homogenous. (Also see **Figure A.4** for

optical microscope images compared with the unhomogenized TEMPO-CNF) After 3 passes, most of the fibrils were less than 1 µm long with a few aggregated fibrils, and the majority of CNFs becomes fine fibrils after 7 passes.

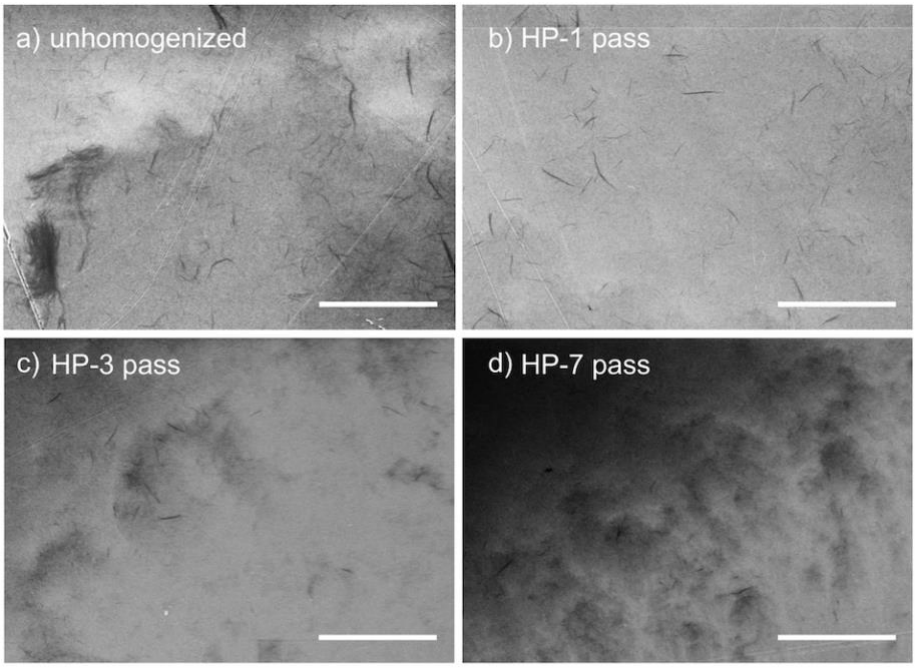

Figure 4.8 SEM images of TEMPO-CNF a) without pressure homogenization, and pressure homogenized at 25000 psi for b) 1 pass (HP-1), c) 3 passes (HP-3) and d) 7 passes (HP-7). The scale bar is 10 µm for all images.

The steady-state shear viscosity was measured for TEMPO-CNF homogenized at different processing conditions. **Figure 4.9** shows the flow curves of the samples homogenized at 25000 psi for 0, 1, 3 and 7 passes, i.e. the same conditions as in **Figure 4.8**. All flow curves show constant viscosity at low shear rates followed by shear thinning. The viscosity is the largest for the sample without homogenization, and decreases with higher number of passes. To compare the effect across all pressures and number of passes, we first choose the viscosity of the most concentrated sample (0.40 wt%) at 2.7 s^{-1} (**Figure 4.10a**); the methodology of comparing viscosity values at a single shear rate in the most

sensitive range of the flow curves is commonly used in literature, even though it only uses a fraction of the data available in **Figure 4.9**. It can be seen in **Figure 4.10a** that at each pressure, the viscosity decreases with increasing number of passes, and gradually plateaus after 5 passes. For the same number of passes, the viscosity decreases with increasing pressure. The only exception to this trend is the 1st pass, after which the viscosity is higher at 25000 psi than 15000 psi, probably because of insufficient shearing at such high pressure where the fibrils might clog the nozzle. Homogenizing the fibrils through multiple stages of pressure from low to high can avoid clogging and can fibrillate the fibrils more efficiently.[158, 160] Some previous studies report higher viscosities when samples are homogenized at higher pressure or more number of passes.[160, 162, 203] This difference can be explained by the fact that the fibrils used in this study have a higher surface charge (1.1 mmol/g), whereas literature values are more commonly reported in the range of µmol/g. Higher surface charges help to repel fibrils upon pressure homogenization, reducing inter-fibril flow friction under shear, resulting in smaller viscosities. It is also possible that the fibrils are homogenized at around 0.5 wt% in the viscoelastic regime, where fibrils are less aggregated. When the concentration of the fibrils is homogenized in the gel regime, the fibrillation caused by high pressure shearing are more likely to cause fibril entanglements, leading to higher viscosities.

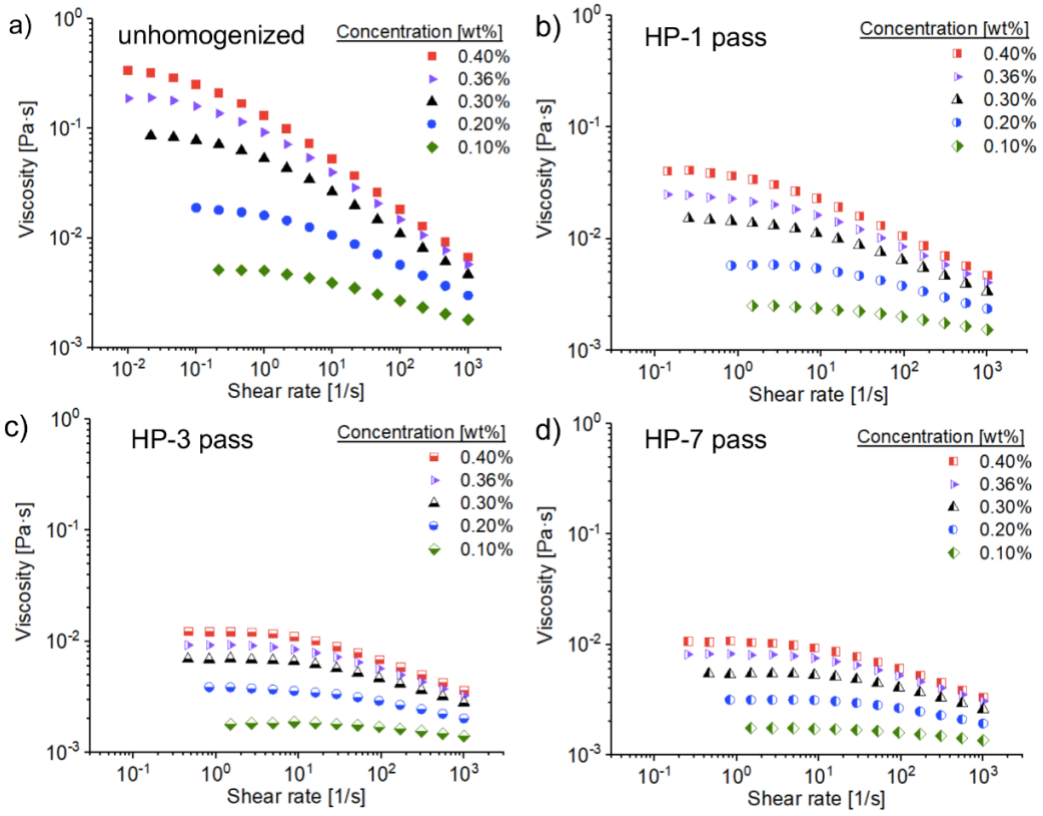

Figure 4.9 Steady-state shear viscosity measurement of TEMPO-CNF a) without pressure homogenization, and pressure homogenized at 25000 psi for b) 1 pass (HP-1), c) 3 passes (HP-3) and d) 7 passes (HP-7. For comparison, the same concentrations are chosen, and all y-axis are set at the same scale.

If the viscosity for sample comparison and probing the effect of homogenization is chosen at a lower sample concentration of 0.2 wt%, but still at the same shear rate 2.7 s^{-1}, the trend is notably different (**Figure 4.10b**). At each pressure, the viscosity still decreases with increasing number of passes, but it reaches a plateau more quickly, after 3 passes. The samples homogenized at 25000 psi have the smallest viscosity at all passes, and the difference between viscosities are smaller compared to viscosities at 0.40 wt% and 2.7 s^{-1}. Since the viscosity of TEMPO-CNF depends on both the concentration and the shear rate, one viscosity value at a fixed shear rate and a concentration is clearly insufficient to fully summarize the rheological behavior for a specific homogenization condition. Although this

method is widely adopted in studies comparing different TEMPO-CNF, a more objective and comprehensive rheological parameter that includes viscosity data at different concentrations and across shear rates is desired to describe TEMPO-CNF samples more robustly.

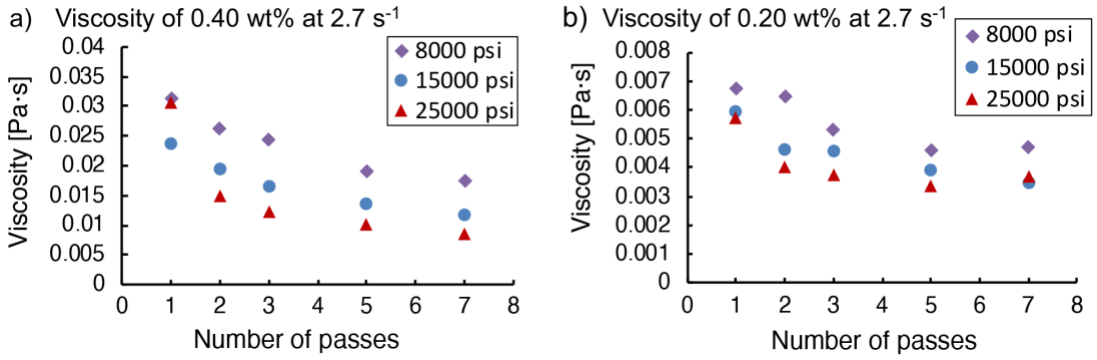

Figure 4.10 The effect of morphology on the TEMPO-CNF rheology based on viscosities at two conditions: a) Viscosity of 0.40 wt% samples at 2.7 s^{-1} and b) at 0.20 wt% and 2.7 s^{-1}. The y-axes of both graphs are plotted on the same scale to facilitate comparison.

4.3.6 Development of a Rheological Flow Index Parameter

The purpose of developing a flow index is to compare the rheology of TEMPO-CNF not just by using a single viscosity value at a somewhat arbitrarily chosen shear rate, but summarizing the viscosities across a wide range of shear rates and at several concentrations. The first step to determine a flow index is to determine the zero-shear viscosity η_0 by fitting the Cross model to the flow curves for all concentrations, as discussed in Chapter 4.3.1:[210]

$$\eta = \eta_\infty + \frac{\eta_0 - \eta_\infty}{1 + (\lambda\dot{\gamma})^m}$$

where η_∞ is the known water viscosity at 25 °C; η_0 is the suspension viscosity in the limit of zero shear rate; λ is the characteristic time scale of the system, and m is the shear-thinning index.

Figure 4.11a shows the viscosity data and the model fit for TEMPO-CNF without homogenization as an example. Once the η_0 values are obtained at various concentrations, the flow index k is extracted as the slope of the linear fit

$$log_{10}(\eta_0) = k \cdot c - log_{10}(\eta_{water})$$

where c is the suspension concentration (in wt%). The intercept is fixed at the value of $log_{10}(\eta_{water})$, i.e. the $\log_{10}$ value of the viscosity of pure water at the measurement temperature. Here the fixed value is -3.05 (water viscosity is 0.00089 Pa·s at 25 °C), as shown in **Figure 4.11b**. Fixing the intercept restricts the fit, but the limit of viscosity at zero concentration should be well defined and the linear fit works well in all cases. The slope of the linear fit, 6.66 in **Figure 4.11b** is defined as the rheological "flow index" for this sample. This single index condenses information of the entire family of flow curves in **Figure 5a** with many viscosity data points into a single parameter, which serves as a "rheological fingerprint" of the sample, i.e. TEMPO-CNF without homogenization.

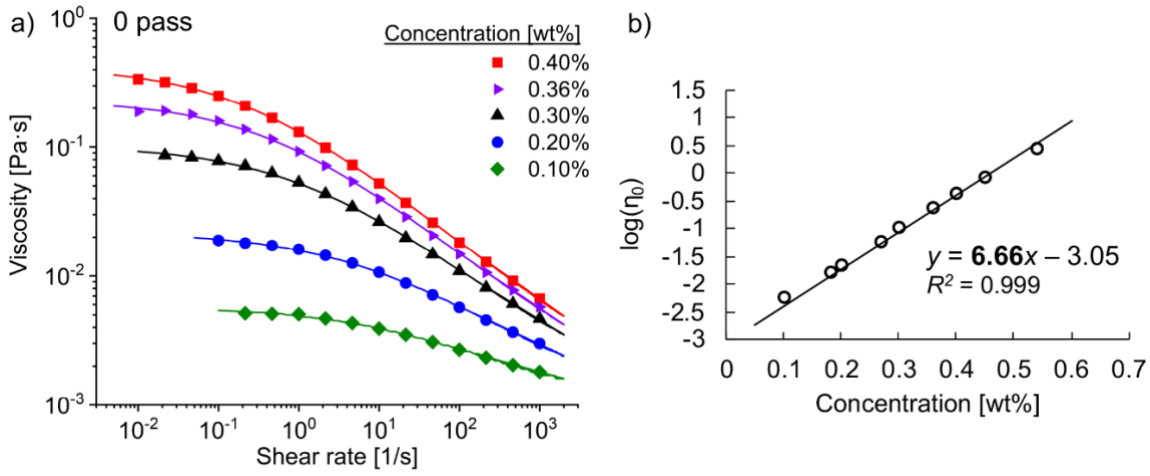

Figure 4.11 a) The flow curves of TEMPO-CNF without homogenization at different concentrations are fitted with the Cross model to obtain η_0. b) Linear fit of $log(\eta_0)$ versus concentration with intercept fixed at -3.05 (pure water); the fitted slope is defined as the flow index.

The robustness of the flow index is demonstrated by comparing the flow index values obtained from linear fitting $log_{10}(\eta_0) = k \cdot c - log_{10}(\eta_{water})$ using a different number of η_0 points. Using η_0 from flow curves of nine concentrations ranging from 0.1 wt% to 0.54 wt% leads to a flow index value of 6.66 ± 0.07 (**Figure 4.11b**). Using fewer η_0 data points will cause slightly larger standard error in estimating the flow index, but the index values are not statistically different (95% confidence) from the 6.66, which uses all nine η_0. (**Table 4-7** and **Figure 4.12**) This indicates that regardless of the exact choice of concentrations, as long as the concentrations are in the viscoelastic regime. Using the flow index is also more robust than using a single viscosity value. If there is data fluctuation during a measurement, the flow index will be less affected as it averages multiple viscosities at different shear rates and concentrations. The procedures to define the flow index minimize subjective decisions with regards to the choice of shear rates and concentrations used for rheological characterization.

Table 4-7 The flow index values, and their fitting error values obtained by linear fitting different number of η_0 data points; R^2 is close to 1 indicating that the log(η_0) scales linearly with the concentrations.

Number of η_0 values used in the linear fit	5	6	7	8	9
Flow index	6.65	6.64	6.65	6.65	6.66
Standard error	0.13	0.10	0.09	0.08	0.07
R^2	0.99	0.99	0.99	0.99	0.99

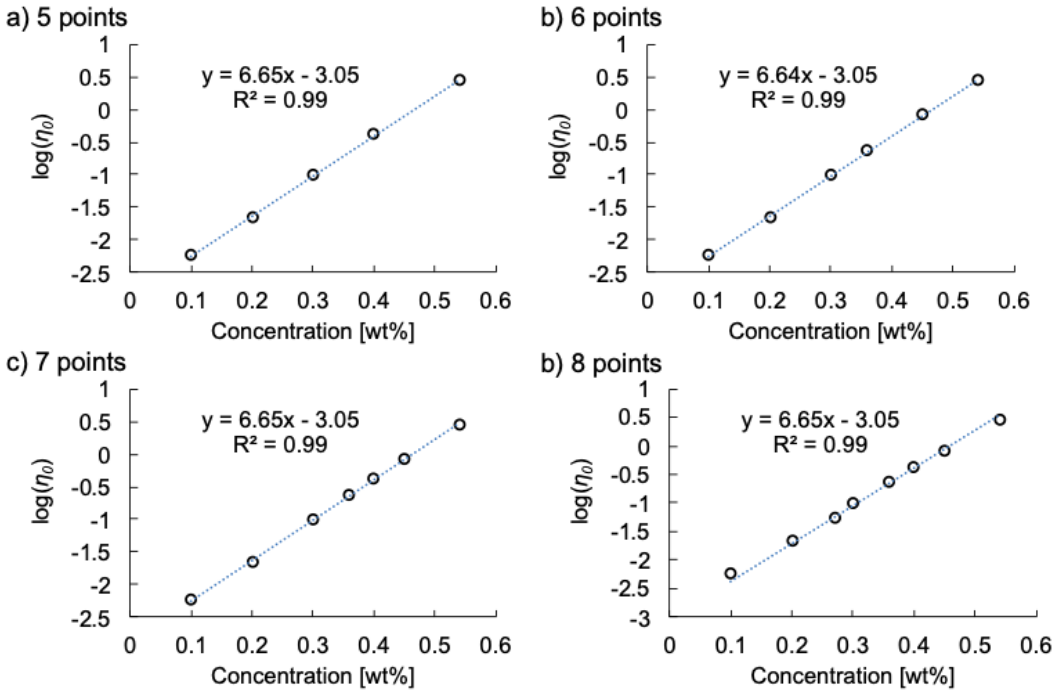

Figure 4.12 Linear fit $\log_{10}(\eta_0) = k \cdot c - \log_{10}(\eta_{water})$ using different number of η_0 points (in support of data presented in Table 4-7 and associated discussion). The intercept is fixed at -3.05 (0.00089 Pa·s at 25 °C).

Fixing the intercept at the value of $\log_{10}(\eta_{water})$ is an important step in determining the flow index, which leads to a single fingerprint parameter that varies from sample to sample. Previous studies have shown that the viscosity at a specific, somewhat arbitrarily chosen shear rate is linear dependent on concentration on a double logarithmic plot (i.e. power-law dependence, $\eta \sim c^{\alpha}$), and comparisons are usually made using the power-law

exponent α. [157, 211] Nevertheless, since both the slope and the intercept change with those fits, comparing different samples using only the slope is less conclusive and clear. Another study defined the flow index as the power law exponent *n* where $\eta = K \cdot \dot{\gamma}^{n-1}$ is used to fit only the shear thinning part of CNF flow curves. [212] The parameter *n* is found to have a power law dependency on concentration based on the viscosity data from 17 literature studies. Although this flow index *n* summarizes the flow curve across shear rates, its value is still concentration dependent. Moreover, selecting the part of the flow curve that can be represented well by the power-law model is often subjective. Some studies have also found that *G'* has a power law dependence on the fibril concentrations ($G' \sim c^{\alpha}$), and sample comparisons are made using the exponent α*.[154, 156, 158, 161, 211, 213]* Nevertheless, for TEMPO-CNF suspensions in the viscoelastic regime, *G'* significantly depends on the frequency. Therefore, *G'* at different frequencies will have different exponent α values. In contrast, this study aims to establish a robust, well-defined rheological parameter that enables the direct comparison of various CNF samples.

In chapter 4.3.1.1, we have shown that the logarithm of the characteristic timescale in the Cross model, $\log_{10}(\lambda)$, also scales linearly with concentration. [210] However, as the concentration approaches zero, the characteristic shear rate $1/\lambda$ approaches infinity, resulting in an undefined value for $\log_{10}(\lambda)$. Hence, we only considered η_0 when developing the flow index.

4.3.6.1 Flow Index of TEMPO-CNF of Different Morphologies

We determined the flow index for all samples that are homogenized at different pressures and number of passes as summarized in **Figure 4.13**; note that each data point in

this figure represents a full set of flow curves similar to **Figure 4.11a**. The sample without homogenization has an index value of 6.66, much higher than the indices of the homogenized samples. All samples that were homogenized for 1 pass have similar index values, likely because the shearing force during the first pass is limited by the nozzle and the thick fibril bundles are not effectively fibrillated. Starting from the 2nd pass, the effect of pressure becomes apparent: the index becomes smaller for samples that were homogenized at higher pressures. At each pressure, the index decreases with increasing number of passes.

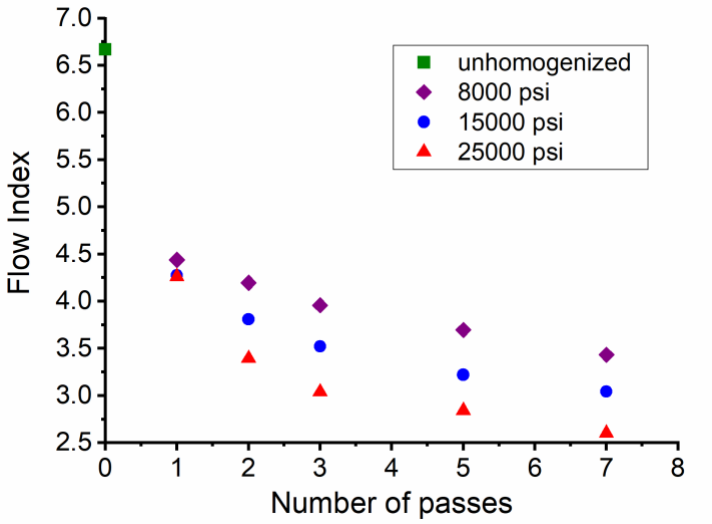

Figure 4.13 Flow index values for TEMPO-CNF homogenized at three different pressures as a function of the number of passes through the homogenizer; the value for the unhomogenized sample is provided as reference.

We also studied the morphology changes related to the energy level of the pressure homogenization. Previous studies estimated total homogenization energy starting with the general energy balance. [214] With some assumptions, the equation simplifies to energy E = *pre-factor* x p x n, where p is the homogenization pressure and n is the number of homogenizer passes. The *pre-factors* are related to the specific material to be homogenized,

the configuration of a specific pressure homogenizer, and the units chosen.[203, 214] In our study, we further simplify the total energy input to the scaling of $E \sim p \times n$, and the homogenization energy at each processing condition is approximated by the product of the pressure and the number of passes.

The flow indices of all samples collapse onto a single curve when plotted versus the total energy input for each condition. (**Figure 4.14a**; note that the units of the horizontal axis of this graph (kpsi) are somewhat arbitrary due to the chosen scaling). The only exception is the data point for unhomogenized TEMPO-CNF. This indicates that it is the total energy input that changes the TEMPO-CNF morphology when the fibrils pass through the pressure homogenizer. Similar morphologies can be obtained using a lower pressure with more homogenization passes. The same conclusion was reached for pressure homogenization of carboxymethylated CNF in a previous study despite the fact that they observed that the viscosity increasing with increasing homogenization energy. [203] When the flow index of the unhomogenized sample is ignored, a power-law relationship can be used to correlate flow index and energy input (**Figure 4.14b**); this correlation can be used to estimate the energy input needed to achieve a desired morphology and rheological behavior. The R^2 from this power law fit can be used to assess the accuracy and robustness of using the flow index compared to using individual viscosity points from the flow curves. (**Table 4-8**) Four sets of viscosity points were chosen to study the variations caused by choosing different concentrations or shear rates. 0.40 wt% and 0.20 wt% are among the high and low of the concentrations used for samples at each homogenization condition, and 2.7 s^{-1} and 169 s^{-1} are for small and large shear rates of the overall range.

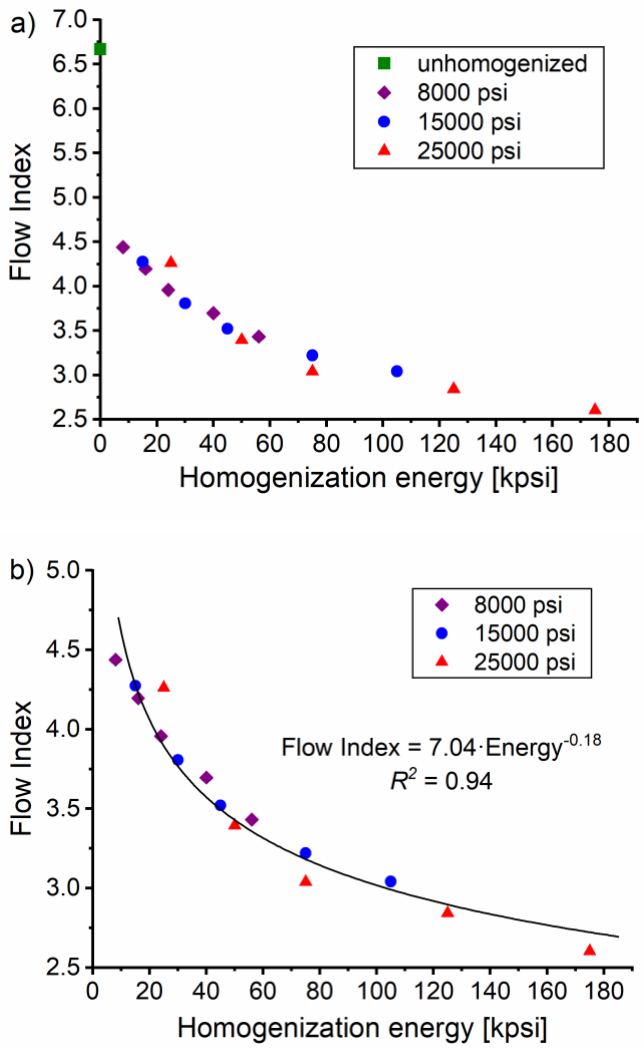

Figure 4.14 Flow index versus homogenization energy (kpsi) approximated by the product of pressure (kpsi) and number of passes. a) Flow index collapse on to a single curve (except for the data point without pressure homogenization). b) The power law describes the relation between flow index and homogenization energy on the TEMPO-CNF.

Table 4-8 R^2 of the power law fit of rheological parameters versus homogenization energy input: use of flow index or single viscosity points at fixed concentration and shear rate. Using the flow index results in the largest R^2, indicating the best fit.

	Flow index	Viscosity			
Conditions		0.4 wt%, 2.7 s^{-1}	0.2 wt%, 2.7 s^{-1}	0.4 wt%, 169 s^{-1}	0.2 wt%, 169 s^{-1}
R^2	**0.94**	0.91	0.86	0.89	0.93

The R^2 of the power law fit using the flow index is the largest, indicating it has the smallest variation of the points and the model fits the data the best. Using different viscosities at fixed concentration and shear rate results in different R^2 ranging from 0.85 to 0.93. The highest R^2 using the viscosity points is at 0.2 wt% and 169 s^{-1}. However, at such low concentration and high shear rate, the viscosity change is very small at different pressures and number of passes. (**Figure 4.15**) Despite its high R^2, the correlation is insensitive to the morphology change, thus unable to show the effect of homogenization on the TEMPO-CNF morphology. The flow index provides a much more meaningful correlation.

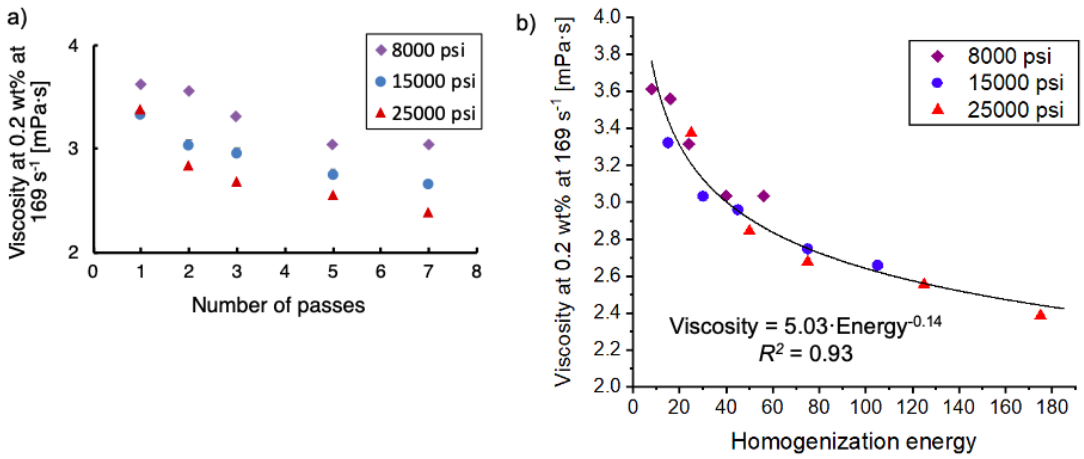

Figure 4.15 a) The viscosity for TEMPO-CNF samples at 0.20 wt% and 169 s^{-1} as function of homogenization conditions, and b) scaling of viscosity with homogenization energy (c.f. Figure 4.14); the energy is approximated by the product of pressure and number of homogenization passes. Note that the viscosity data are on a linear scale (in mPa·s), so the changes with homogenization conditions are small; although the correlation has a high R^2 value, viscosity changes are not very sensitive to homogenization parameter changes.

4.3.6.2 Flow Index of TEMPO-CNF of Different Surface Charges

The flow index can also be used to reflect variations in surface charge among TEMPO-CNF samples. In this study, samples with three different surface charges were prepared and were all pressure homogenized at 25000 psi for 7 passes. From the morphology study, we find that further homogenization lead to minimum viscosity change (**Figure 4.16**), indicating that the changes of fibril morphologies is insignificant between these samples. **Figure 4.17** shows the flow curves measured at four concentrations for all three samples. At each concentration, the TEMPO-CNF with higher surface charge has lower viscosity. Higher surface charge results in stronger repulsion forces between the fibrils, reducing their entanglement and aggregation, making it easier to flow under shear force during the viscosity measurement. Similar trend has been observed in the previous studies.[160, 174]

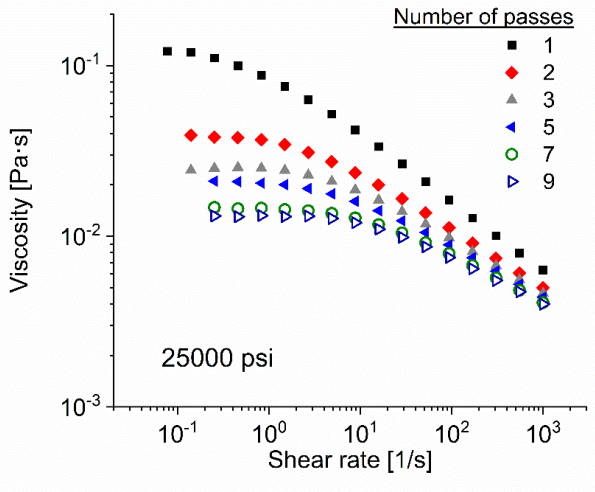

Figure 4.16 Flow curves for TEMPO-CNF samples that were pressure homogenized at 25000 psi for 1, 2, 3, 5, 7 and 9 homogenization passes at fixed concentration of 0.48 wt% for all passes. The viscosity drop from 7 to 9 passes was small, indicating little morphology change.

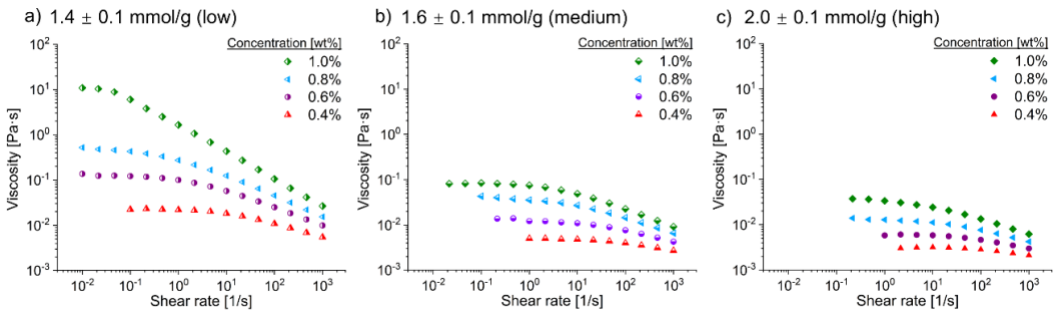

Figure 4.17 Flow curves of TEMPO-CNF of three surface charges. The *y*-axes are set on the same scale for facile comparison.

The data in the **Figure 4.17** can be used to determine the flow index for these three samples according to procedures outlined above (**Figure 4.18**). **Figure 4.19** clearly shows that the flow index decreases when the fibrils have higher surface charge. A single flow index number summarizes viscosities across shear rates and multiple concentrations, presenting a clear and concise relationship between TEMPO-CNF surface charge and its rheology.

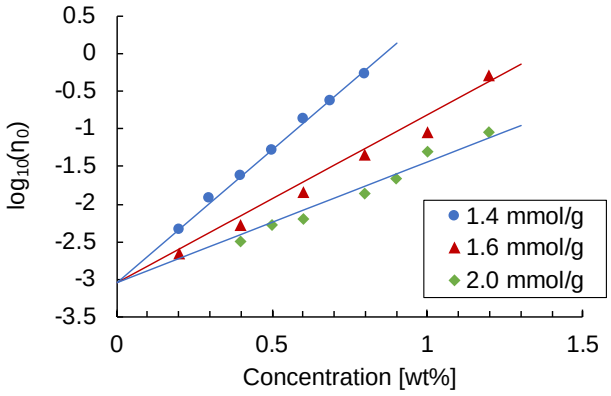

Figure 4.18 Linear fit $\log_{10}(\eta_0) = k \cdot c - \log_{10}(\eta_{water})$ to determine the flow index for TEMPO-CNF samples with different surface charges. The flow index value is 1.61 for low surface charge sample (1.4 mmol/g), 2.24 for medium charge sample (1.6 mmol/g) and 3.55 for high charge sample (2.0 mmol/g).

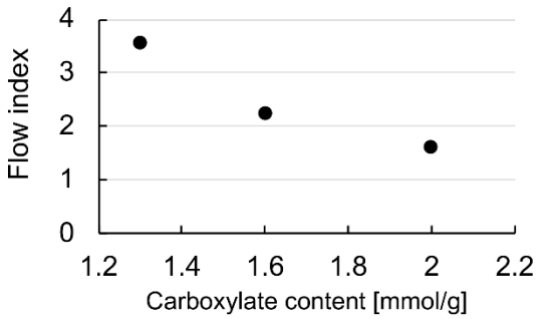

Figure 4.19 Flow index representation of TEMPO-CNF samples with three different surface charges.

In summary, the flow index defined above is a useful parameter that captures the rheology of TEMPO-CNF viscoelastic suspensions. Since the viscosity of TEMPO-CNF is concentration dependent and has shear thinning behavior, it is inconclusive to use a single viscosity value to compare TEMPO-CNF at different morphologies or surface charges. The flow index solves this problem combining the viscosity information across concentrations and shear rates. Its value is determined from linear fit $\log_{10}(\eta_0) = k \cdot c - \log_{10}(\eta_{water})$. The flow index can be viewed similar to the exponent factor α of the concentration related scaling $\eta_0 \sim c^{\alpha}$, which can be rewritten as $\log_{10}(\eta_0) \sim \alpha \cdot \log_{10}(c)$. This scaling, together with the scaling of specific viscosity, $\eta_{sp} \sim c^{\alpha}$. has been extensively studied for chitosan suspensions, where $\eta_{sp} = (\eta_0 - \eta_s)/ \eta_s$ and η_s is the solvent viscosity. [215-217] The values of α is related to the number of interactions, including hydrogen bonding and hydrophobic interactions, between the chitosan chains. [215] Larger α indicates larger number of interactions. α is also related to the extent of entanglements, where large α indicates sufficient chain entanglements.[217] Moreover, some studies on cellulose nanofibril use the scaling of $G' \sim c^{\alpha}$, where the exponent α is related to the structural properties of the suspension. [156, 211, 213] Higher α values indicate a more rigid network structure. [211] Similarly, the flow index in our study reflects the overall fibril network

structure of a TEMPO-CNF suspension in the viscoelastic regime, including the interactions of hydrogen bonding and Van der Waals forces. Smaller fibrils generated by pressure homogenization have fewer fibril entanglements and thus weaker Van der Waals interactions, as indicated by the smaller flow index. Samples with higher surface charge have stronger hydrogen bonding interactions among the fibrils, but also stronger electrostatic repulsion between the fibrils, which reduces the fibril entanglement. This leads to weaker overall fibril structure, as indicated by the smaller flow index.

4.4 Conclusion

We developed a rheological model that combines the power law and Cross models to parameterize the flow curve at each individual concentration. This combined model accurately describes the flow curves across the full range of the shear rates and for all concentrations for both CNC and TEMPO-CNF. The two most sensitive parameters in this model, $log(\eta_0)$ and $log(t)$ linearly correlate with the suspension concentration, which can be used to estimate the concentration of an unknown sample with an error less than 0.2 wt% for CNC and an error less than 0.1 wt% for TEMPO-CNF. The model can also be used to estimate the salt concentration because the addition of salt does not fundamentally change the rheological characteristics of the sample until the threshold is reached at which aggregation and phase separation occur. Both applications are relevant to quality control. Moreover, the combined model is used to study the TEMPO-CNF structure-property relationships where the morphology and surface charge of the TEMPO-CNF are varied. Pressure homogenization is used to modify the TEMPO-CNF morphologies by varying the pressure and the number of passes. Higher pressure and a larger number of passes defibrillate and shorten the fibrils, resulting in smaller fibrils of more uniform size

distribution. The morphology change is captured by the rheology where at the same concentration the viscosity is the largest for the sample without homogenization. The viscosity decreases with higher pressure or higher number of passes. For TEMPO-CNF with different amounts of surface charge, the viscosity is lower when the surface charge is higher. To use the full data across shear rates and concentrations effectively, a rheological flow index k was developed according to the scaling relation $\log_{10}(\eta_0) = k \cdot c - \log_{10}(\eta_{water})$, where η_0 is the zero-shear viscosity determined by the Cross model and c the suspension concentration in the viscoelastic regime. To obtain the flow index, TEMPO-CNF suspensions in the viscoelastic phase are diluted to several concentrations and the flow curves are measured for all samples and fit to the Cross model. A linear fit is then performed on $log_{10}(\eta_0)$ versus c, so that the many viscosity points in the multiple flow curves are condensed into a single parameter, establishing a one-to-one relationship between the TEMPO-CNF of a specific condition and its rheology. The flow index is related to the fibril network structure. Higher homogenization pressure, higher number of passes, or higher surface charges all lead to smaller flow index. Moreover, the flow index of all homogenized samples collapse onto a single curve, having a power law scaling with the cumulative homogenization energy. This indicates that the morphology is changed by the total energy input. The flow index summarizes the viscosity information across the concentrations and the shear rates, which is a more objective and comprehensive rheological parameter to describe and compare the TEMPO-CNF suspensions in the viscoelastic regime. The flow index can be used for quality control and/or benchmarking of the cellulose nanomaterials, and can guide the selection of optimum processing conditions.

CHAPTER 5. CHARACTERIZING THE VISCOSITY OF CELLULOSE NANOCRYSTAL SUSPENSIONS VIA VISCOMETER

5.1 Introduction

The rheological measurements in Chapters 3 and 4 were all performed using an advanced rheometer. The high sensitivity of this instrument and well-defined measuring geometries enable accurate detection of small changes in rheological properties. Also, the rheometer is able to perform oscillatory and steady shear experiments, which enables measurements of dynamic moduli in addition to viscosity. By performing rheological characterizations and developing a new rheological model and a new characteristic rheological parameter, we have established that rheology has the potential to be used for quality control of manufacturing cellulose nanomaterials. Nevertheless, due to the high equipment cost and the expertise required for operation, the advanced rheometer is not ideal for use in an industrial manufacturing setting. [218] An industrial-grade viscometer that is low-cost and easy to operate is preferred, especially if the device -unlike the rheometer- is compatible with inline viscometry.

Previous studies have used two types of industrial-grade viscometer: a rolling-ball viscometer and the well-known Brookfield viscometer.[114] Gonzalez-Labrada *et al.* measured the viscosity of dilute aqueous cellulose nanocrystal (CNC) suspensions at several concentrations using the rolling-ball viscometer at different tilt angles to obtain zero-shear viscosity, η_0, by extrapolation to vanishing shear rate. [219] In their study, the authors used η_0 to determine the intrinsic viscosity [η] via the Fedors equation and Huggins

equation in order estimate the aspect ratio of the CNC particles; as discussed in section 2.1.2, this is a common estimation method. Mohtaschemi *et al.* characterized suspensions of fibrillated cellulose at concentrations of 1.0 to 2.3 wt% using a Brookfield viscometer with bucket-vane geometry. [192] Due to the wide gap and complex shape of the geometry, a correction factor is needed to translate the rotational speed of the viscometer (in units of *RPM*) to a shear rate in the standard units of s^{-1}. Without a meaningful shear rate value, it is nearly impossible to quantitatively assess the rheological properties for non-Newtonian fluids, which the cellulose nanomaterial suspensions in this thesis are. Moser *et al.* used a Brookfield viscometer with various spindles to measure the flow curves of enzyme- and TEMPO-pretreated cellulose nanofibrils that were homogenized for different numbers of homogenizer passes. [220] However, only one viscosity value was reported from each flow curve to represent the fibril characteristics, and the authors reported that stable viscosity values were difficult to obtain because the samples were inhomogeneous.

Although these studies explored the feasibility of using industrial-grade viscometers to characterize suspensions of cellulose nanomaterials, many challenges remain. For example, there is still a need for detailed preparation and test protocols that can be easily followed by a person without extensive knowledge in rheology. Moreover, the apparent viscosity variations that can occur when measurements are performed with different viscometer spindles on the same non-Newtonian sample have not been investigated sufficiently. Finally, sample-to-sample variation in measurements must be addressed explicitly for complex samples like cellulose nanomaterials. As a result, it is unclear if and how data from such viscometers can be used to perform analyses similar to the work described in previous chapters.

In this chapter, we investigate the possibility of using a Brookfield viscometer to obtain reproducible flow curves for CNC suspensions that can subsequently be used for quantifying its rheological properties across multiple concentrations. Preparation and test protocols were developed to obtain reliable viscosity results for CNC samples ranging from 3.6 wt% to 10.9 wt%, which includes the concentration range with the most complex rheological behavior as observed with the advanced rheometer (e.g. Fig 3.5 in Section 3.4.3). The samples were measured using different spindles with different stress ranges in order to cover the full shear rate range and to study the non-Newtonian behavior. Moreover, the effect of mixing on viscosity was studied and the combined model developed in Section 4.3.1 is used to fit the CNC flow curves that exhibit three-regime shape.

5.2 Materials and Method

5.2.1 Viscometer and Spindles

A standard Brookfield viscometer (DV-E type) (**Figure 5.1**) and a set of spindles (RV type; **Figure 5.2**) were used to measure the viscosity. This viscometer measures torque (expressed as % of full range) as a function of rotational speed (unit *RPM*); this data can be converted into viscosity (unit *cP*) based on conversion factors, but due to the complex flow field, the conversion is challenging, in particular for non-Newtonian fluids. According to the instrument manual, one should record the viscosity data only when the measurement is steady (viscosity value stops flashing on the screen) and when the torque percentage is between 10% and 100% of full range. To satisfy the torque requirement, different spindles may need to be used to measure a sample at different rotational speeds (i.e. shear rates). No universal equation is available to convert *RPM* to s^{-1} for disk-type

spindles (#1 to #6), whereas for the cylindrical spindles (#7 and #61) the *RPM* can be converted to s^{-1} via the empirical equations 1 s^{-1} = 0.209 *RPM* (spindle #7), and 1 s^{-1} = 0.22 *RPM* (spindle #61).

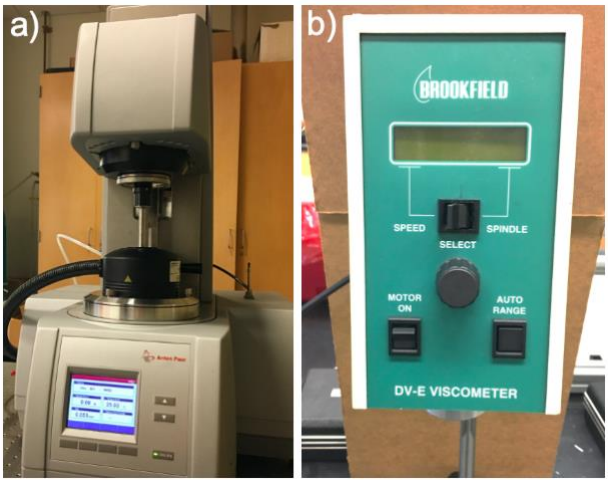

Figure 5.1 a) The rheometer used in chapter 3 and 4 and b) the viscometer used in Chapter 5.

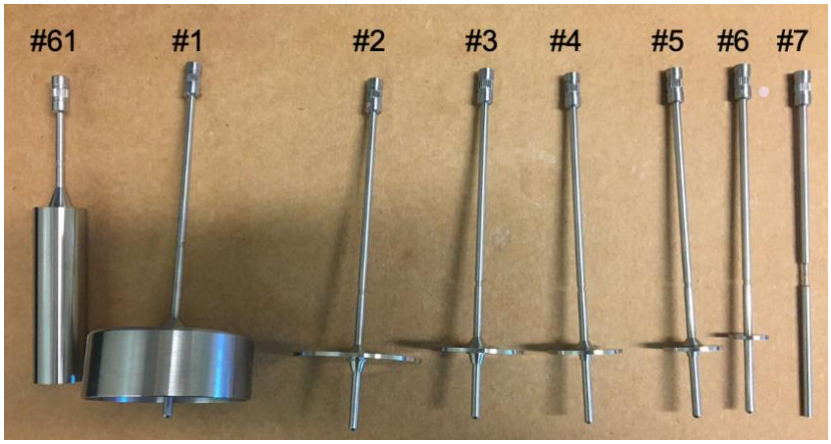

Figure 5.2 Brookfield spindles of RV type (#1 to #7) and LV type (#61) as used in this chapter. Spindles #61 and #7 are cylindrical, while #1-6 are disk-type spindles.

5.2.2 Materials and Preparation Protocols

CNC (lot # 2018-FPL-CNC-117) was purchased from the processing center of University of Maine. The is a different batch of CNC that were used in Chapter 3 and 4. The stock concentration is 10.9 wt%, which was determined by oven-drying and equilibrating in the temperature-controlled room (for description of method see Section 3.4.1). CNC suspensions at lower concentrations were prepared by mixing the stock with DI water. CNC samples at 10.9 wt% and 9.1 wt% were prepared in 30 ml vials to accommodate the shape of the spindle #7. The samples were mixed using a vortex mixer (Fisher vortex) at speed setting 8 for at least 60 seconds until the sample looked homogenous. Only spindle #7 was used to measure samples at these two higher concentrations. CNC suspensions between 3.6 wt% and 7.2 wt% were prepared at suspension volume of 400 ml in a 500 ml beaker. These suspensions were mixed by stirring for 1 hour with a stir bar; the stir speed was set at the highest speed possible, which varied for different concentration due to viscosity variations. For example, stir speed of 420 RPM was used for 7.2 wt% and 580 RPM was used for 5.4 wt%. 7.2 wt% and 5.4 wt% samples were also homogenized using a disperser (IKA T25 digital ULTRA-TURRAX) at 12,000 RPM for 15 minutes to study effects of high-speed mixing on viscosity.

5.2.3 Test Protocols

To mimic the time-averaged viscosity reported by the rheometer in previous chapters and to ensure that the viscosity was in steady state, at least three viscosity values were recorded for each shear rate larger than 1 RPM during the steady-state measurement. Though in steady state, multiple different viscosity values are shown as the spindle rotates,

especially at high shear rates. For shear rates larger than 1 RPM, the viscosity values were recorded after the spindle makes at least two full rotations. Each viscosity point in this chapter represents an average of several viscosity values recorded following the above protocol.

5.3 Results and Discussion

5.3.1 Accuracy and Sensitivity of the Viscometer

To check the accuracy and sensitivity of the viscometer, the flow curves of a Newtonian fluid, glycerol, were measured using different spindles to cover the whole range of the shear rates. (**Figure 5.3**) The viscosity is plotted on a linear scale to better visualize the difference. The viscosity, 0.55 ± 0.001 Pa·s measured by the rheometer is almost constant, which is expected for a Newtonian fluid. The viscosity values measured by the viscometer using different spindles at different rotational speeds are slightly larger, ranging from 0.59 to 0.72 Pa·s. That is the difference of 8% to 24% compared the 0.55 Pa·s value measured by the rheometer as a reference, well above the measurement errors one would expect for the rheometer when measuring a viscous Newtonian fluid. Moreover, the viscosity measured by the viscometer has a larger variation and the average is 0.68 ± 0.04 Pa·s. It also shows larger viscosity at higher rotational speed, especially for spindles #5 and #6.

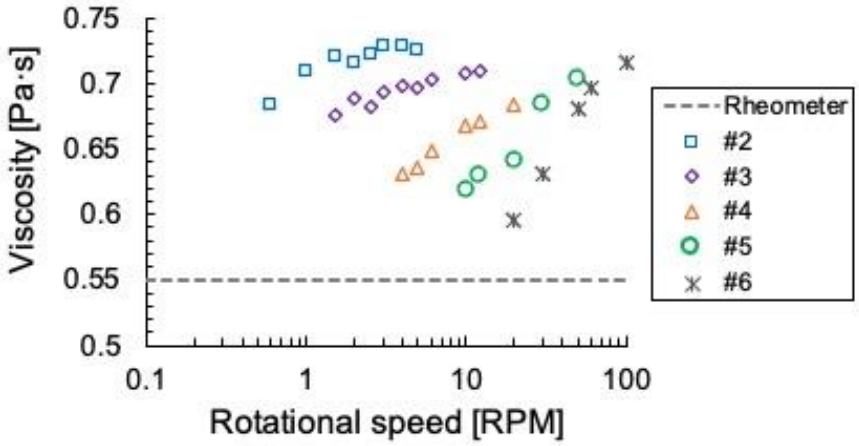

Figure 5.3 Glycerol viscosity measured using different Brookfield spindles (RV, disk-type), and using the rheometer with cone-plate geometry. The viscosity measured by the rheometer (0.550 ± 0.001 Pa·s) serves as reference.

The above results show accuracy and reproducibility limitations of the viscometer. Though easier to operate, it is less accurate than the advanced rheometer and suffers from larger viscosity variations at different shear rates, especially when multiple spindles must be used to cover a wide range of shear rates. The glycerol measurements establish the range of the accuracy and sensitivity, which is useful when analyzing and interpreting viscosity data for cellulose nanocrystals in the following sections.

5.3.2 Unit conversion of Deformation Rate

The viscometer uses rotational speed of the spindle (*RPM*) to describe the deformation rate of the sample, which is different from the shear rate (s^{-1}) that is used for the well-defined geometries of the advanced rheometer. For cylindrical spindles #7 and #61, empirical factors have been established to convert *RPM* to s^{-1}. The disk-type spindles, however, lack a standard conversion factor because of the complex flow field of a spinning disk. A prior study proposed a method to converts the rotational speed in *RPM* to shear rate

in s^{-1} for disk-like RV spindles in non-Newtonian. [221] A flow curve is first measured using a single spindle: both the viscosity and the torque percentage are recorded at each shear rate. The torque percentage is then converted to an average stress value by multiplying with an empirical factor proposed in the study. A linear fit is then imposed on the log(stress) versus log(*RPM*) data in order to extract the slope of the fitted line, which quantifies how non-Newtonian the fluid is. Based on this slope value and the spindle number, a conversion factor from rotational speed *RPM* to shear rate s^{-1} is determined from tabulated values in the paper.

A CNC suspension at 7.2 wt% is shown below as an example: the viscosity is first measured with multiple Brookfield spindles, and subsequently the rotational speed is converted to shear rate following the method described above. The viscosities measured using different spindles at the same rotational speed yield very similar viscosity values, and the flow curves of individual spindles overlap and form a reasonable master curve. (**Figure 5.4a**) As the viscosity covers two decades, it is plotted in log-scale, which compresses the viscosity difference of using different spindles compared to **Figure 5.3** where the y-axis is in linear scale.

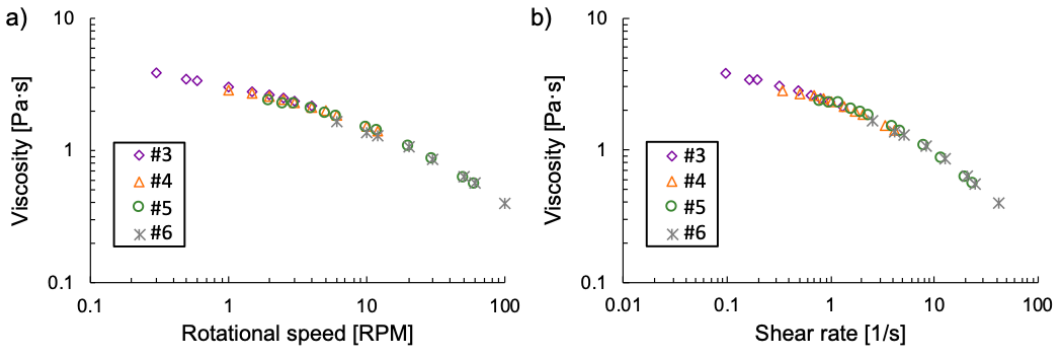

Figure 5.4 CNC of 7.2wt% is measured by viscometer using different spindles (#3 to #6). The rotational speed is converted to shear rate following the procedure outlined in a previous study by Mitschka. [221]

After converting the units to shear rate, the flow curves overlap slightly better. (**Figure 5.4b**) Nevertheless, the unit conversion methodology is not straightforward. Moreover, as Mezger has pointed out, even if an approximate correlation can be found between the results obtained with a Brookfield spindle and a standardized measuring system like those used in the rheometer, the conversion only applies to these two systems, and only for this specific sample with its particular non-Newtonian behavior. [222] As a result, one needs to repeat the process for every flow curve to determine a conversion factor, which is laborious and thus unfavorable for a quality control process. Hence, analysis of the CNC viscosity data presented in this chapter is limited to comparing samples of different concentrations within the Brookfield viscosity system, without trying to assess its accuracy by comparing to the rheometer measurements.

5.3.3 Brookfield viscosity of cellulose nanocrystal suspensions

Additional cellulose nanocrystal (CNC) suspensions at two other, intermediate concentrations were measured using multiple Brookfield spindles to cover the whole deformation rate range from 0.3 to 100 *RPM*. **Figure 5.5** shows the viscosity of 6.3 wt%

and 5.4 wt% suspensions as a function of rotational speed. Note that each viscosity point is an average of several recorded viscosity values as specified in the test protocol in section 5.2.3. These results indicate that the viscosity variations are acceptably small on a logarithmic when using different spindles to measure the same non-Newtonian sample.

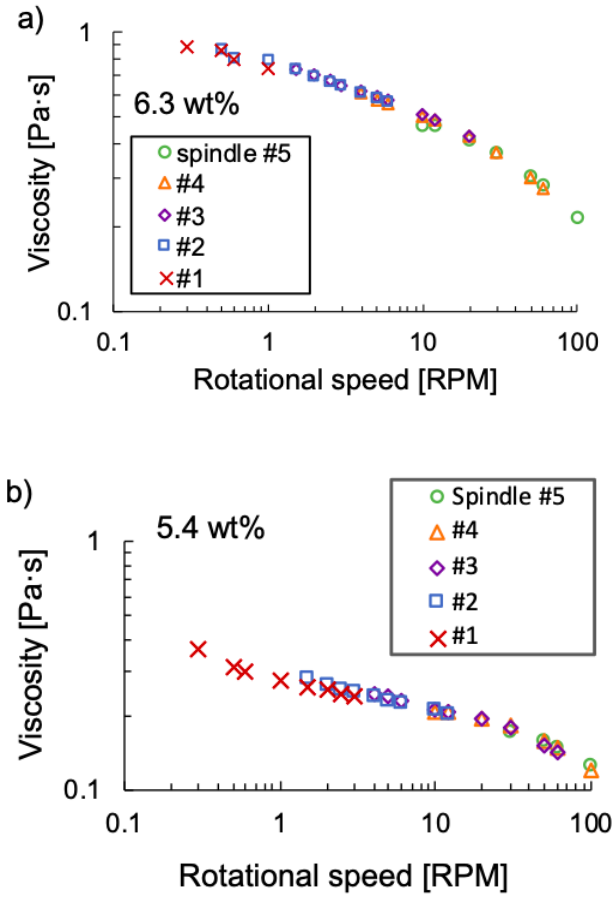

Figure 5.5 Viscosity of a) 6.3 wt% and b) 5.4 wt% CNC suspensions measured using different disk-shaped spindles on a Brookfield viscometer.

Based on **Figure 5.5**, a compound viscosity curve as function of rotational speed can be defined by using data from different spindles. If multiple data points are available at a given rotational speed, the average viscosity value is used; if only one spindle is available at a specific rotational speed, then the value for that spindle is used as the overall

viscosity. **Figure 5.6** shows the viscosity data that was thus collected for several CNC concentrations from 3.6 wt% to 10.9 wt%. At 10.9 wt% and 9.1 wt%, the viscosity is shear thinning over the whole shear rate range. At 5.4 wt%, 6.3 wt% and 7.2 wt%, the viscosity curves show a plateau at lower shear rates, followed by slight shear thinning at higher shear rates. At 3.6 wt%, the viscosity is almost constant, indicating a Newtonian fluid; its viscosity values at higher shear rates increase slightly, but this is likely caused by flow instabilities, thus defining the lower detection limit for viscosity of the viscometer. Flow curves at concentrations below 3.6 wt% were not measured as the accuracy of the data cannot be guaranteed.

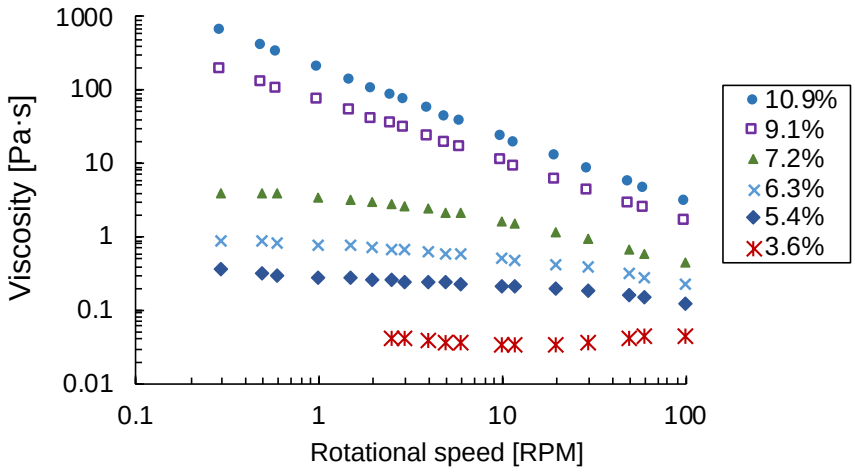

Figure 5.6 Flow curves of CNC concentrations 3.6 wt% to 10.9 wt% measured by the Brookfield viscometer.

The sample-to-sample variation was investigated for 10.9 wt% and 5.4 wt%, with three separate samples measured at each concentration. (**Figure 5.7**) The flow curves are in good agreement, with variations that are typical for rheological measurements of multiphase non-Newtonian fluids, ~10% deviation in viscosity values. Thus, the sample-

to-sample variation is acceptable as long as the samples are prepared following the same protocol.

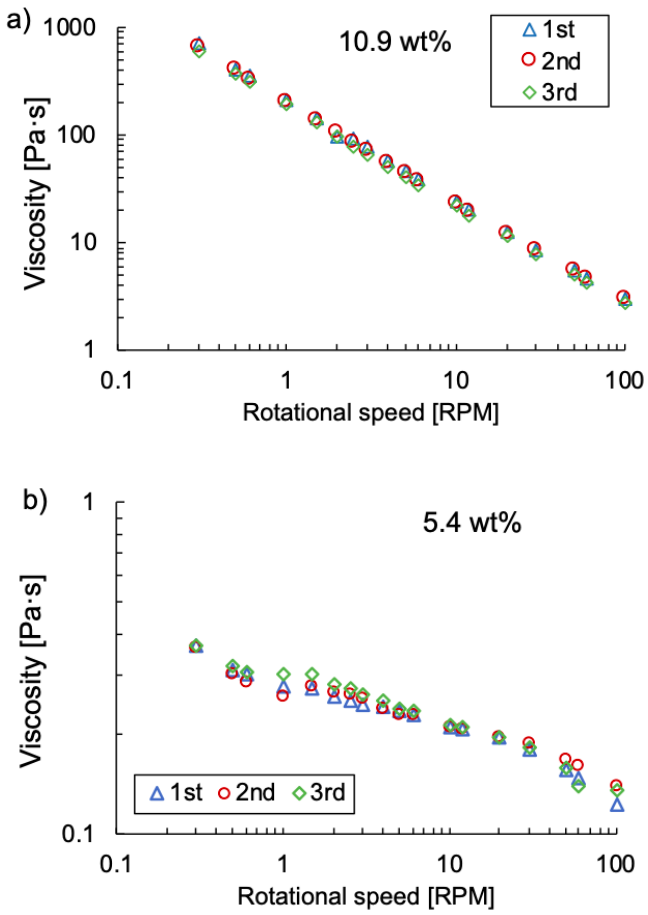

Figure 5.7 Flow curves for three separate samples measured at a) 10.9 wt% and b) 5.4 wt% show small sample-to-sample variation, as indicated by the overlapping flow curves.

Preparing samples at multiple concentrations involves mixing the stock CNC suspension with water. It is expected that different mixing methods will affect the final viscosity. Section 3.4.2 shows that sonication reduces viscosity significantly compared to vortex mixing. Here, the effect of mixing is compared between stirring versus homogenization in order to assess how important that aspect of an industrial measuring protocol would be. Homogenization greatly reduces the viscosity, and after

homogenization the flow curves for both 7.2 wt% and 5.4 wt% show three regions. (**Figure 5.8**) The viscosity first decreases at lower shear rates, then plateaus at intermediate shear rates, finally followed by shear thinning at high shear rates. The three-regime flow curve is not observed for the samples that are mixed by stirring, likely because the mixing forces are not strong enough to break up aggregated domains into primary particles. Thus, at lower shear rates, where the shear force is also small, different domains are not aligned under flow.

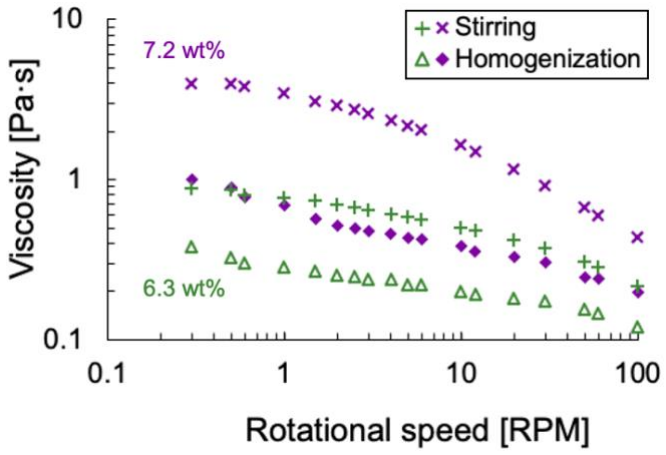

Figure 5.8 Effect of mixing protocol on viscosity measurements in viscometer; homogenization (12,000 *RPM*) reduces the viscosity compared with stirring; the stir speed was 450 *RPM* for 7.2 wt% and 580 *RPM* for 6.3 wt%.

In section 3.4.3, a combined rheological model was presented that accurately captures the full flow curves of CNC suspensions measured with the rheometer. In similar fashion, a combined model can be used to describes the viscosity η as a function of rotational speed Ω:

$$\eta = a'\Omega^{-b'} + \eta'_{\infty} + \frac{\eta'_0 - \eta'_{\infty}}{1+(\lambda'\Omega)^{m'}} \tag{6-1}$$

This equation was used to fit the flow curves of the samples that were mixed by homogenization. (**Figure 5.9**) The parameters from this fit are summarized in **Table 5-1**. **Figure 5-9** shows that the model accurately describes the viscosity across shear rates at concentrations of 6.3 wt% and 7.2 wt%. Though viscosity points of a narrower range of the rotational speed are fitted compared to the **Figure 4.1**, the quality of the fit is not comprised.

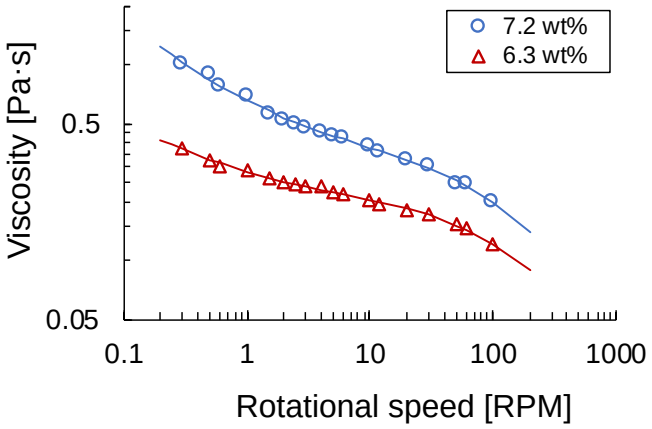

Figure 5.9 Flow curves of homogenized 7.2 wt% and 6.3 wt% CNC suspensions measured by the Brookfield viscometer. The solid lines represent fitted lines using the combined model (Equation 6-1).

Table 5-1 Parameter values obtained from fitting the combined model to 7.2 wt% and 6.3 wt% samples that were mixed by homogenization.

Concentration [wt%]	a'	b'	η_0'	λ'	m'
6.3	0.092 ± 0.032	0.54 ± 0.16	0.19 ± 0.03	0.0067 ± 0.0012	0.87 ± 0.23
7.2	0.33 ± 0.072	0.63 ± 0.12	0.33 ± 0.072	0.0084 ± 0.0023	0.92 ± 0.29

5.4 Future Work

In section 5.3.2, we have shown that the rotational speed can be converted to shear rate, and the flow curves measured by different spindles form a master curve. (**Figure 5.4**) Nevertheless, it is unclear how different the viscosity values are compared to the ones measured by the advanced rheometer. To study the viscosity difference, preliminary results were obtained for 10.9 wt% and 5.4 wt%. The flow curves are measured by cylindrical spindles #7 (for 10.9 wt%) and #61 (for 5.4 wt%) were compared to the same sample measured with the rheometer. (**Figure 5.10**) Only these two spindles are used as they have well-defined conversion factors that convert the rotational speed (in units *RPM*) to shear rate (in s^{-1}), without going through the lengthy process of determining the conversion factors. The flow curves measured by the viscometer overlap with the flow curves measured by the rheometer, although the viscometer with a single spindle can only cover a portion of the range of shear rates achievable with the rheometer. This preliminary result indicates that the viscosity measured by the less-advanced, industrial-grade viscometer is accurate, although the range of shear rates is limited. Follow-up experiments must be performed to assess the accuracy of the viscosity measured by the disk-type spindles (#2 to #6) using conversion method outlined in Section 5.3.2 by Mitschka. [221]

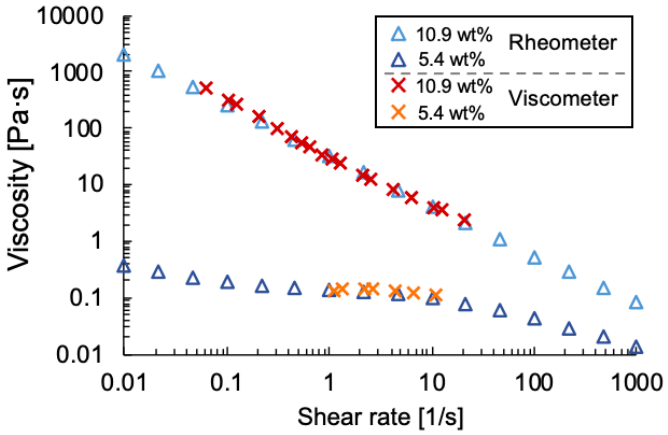

Figure 5.10 The viscosity measured by the rheometer (Anton Paar MCR-302) compared with the viscometer (Brookfield DV-E). The 10.9 wt% sample was measured with spindle #7 (RV type cylindrical spindle, 1 s^{-1} = 0.209 *RPM*), and the 5.4 wt% was measured with spindle #64 (LV type cylindrical spindle, 1 s^{-1} = 0.22 *RPM*).

Regardless of the conversion outcome, the viscosity analysis via model fitting can still be performed using the viscometer viscosity data as a function of rotational speed. We have shown that the combined model accurately captures the flow curves at two intermediate concentrations. (**Figure 5.9**) More work remains to be done to fit the model for other concentrations to extract the parameters. Following the same idea as outlined in Section 4.3.2, the parameters can then be used to establish calibration curves, which can estimate the concentrations of an uncharacterized CNC sample. Similar characterization and analysis can also be performed for TEMPO-CNF suspension. If the method can be successfully implemented, it will increase the potential of using rheology for quality control for cellulose nanomaterials. Not only because the rheology method is rapid and accurate as discussed in 4.3.2, but also because of the low-cost and easy operation using an industrial-grade viscometer.

5.5 Conclusion

The viscosity as a function of rotational speed of CNC suspensions at multiple concentrations were measured using the Brookfield viscometer. Sample preparation and viscometer test protocols were developed to obtain reliable, reproducible flow curves. Small viscosity variations have been found when measuring the same sample using different spindles at the same rotational speed, and when measuring different samples at the same concentration. The flow curves of higher concentrations (10.9 wt% and 9.1 wt%) are shear thinning across the shear rates. At lower concentrations (3.6 wt%), the viscosity is constant and increases slightly at higher shear rates, a sign of flow instabilities. At intermediate concentrations (7.2 wt% to 5.4 wt%), the flow curves plateau followed by shear thinning. The flow curves show three-region shape, which is the typical shape of CNC at intermediate concentrations as discussed in Section 3.4.2. (**Figure 3.4**), after the samples are homogenized at higher shear rates breaking down aggregates. Moreover, the flow curves can be accurately captured by the combined model $\eta = a'\Omega^{-b'} + \eta'_\infty + \frac{\eta'_0 - \eta'_\infty}{1+(\lambda'\Omega)^{m'}}$, which is the same combined model in Section 4.3.3 (Equation 4-1) except that the rotational speed Ω is used instead of the shear rate $\dot{\gamma}$. The capability of accurately measuring the CNC viscosity by an industrial-grade viscometer further enhances the potential of using rheology as a quality control tool in the manufacturing setting.

CHAPTER 6. DEWATERING CELLULOSE NANOMATERIAL SUSPENSIONS AND PREPARING CONCENTRATED POLYMER COMPOSITE GELS VIA REVERSE DIALYSIS

6.1 Introduction

As discussed in Section 1.3, cellulose nanomaterials (CNMs) are typically first produced in aqueous suspensions at low concentrations, because key processing steps, such as fibrillation through pressure homogenization, cannot be performed at higher concentrations due to low gelation concentrations 1-3 wt% for cellulose nanofibril (CNF), 10 wt% for cellulose nanocrystal (CNC)). [63, 83] Subsequent dewatering or drying is therefore necessary to reduce storage and transportation costs, or as a pre-processing step for the many applications that require higher concentrations in CNM feedstock.

Methods to efficiently dewater CNM suspensions to reach high concentrations while maintaining good redispersibility are currently lacking. Ultrafiltration is the current industrial standard for purifying and dewatering CNM suspensions in manufacturing. [166, 223] Irreversible aggregation, however, is a major concern, and although tangential flow configurations reduce aggregation somewhat, this remains a major limitation. In addition, the dewatering flow significantly slows down as the viscosity increases. [223, 224] In current processes, concentration is only increased to around 5 wt% for CNC and 0.5 wt% for TEMPO-CNF. [166, 225] Evaporation is another common dewatering method, which can be used to dewater suspensions all the way to the dry state, if desired. However, evaporation is energy intensive and known to cause aggregation at the vapor-liquid

interface where water is removed, especially for nanofibril materials due to their large surface area and hydrogen bonding. [83, 86] Such aggregates are formed while the overall CNM concentration is still fairly low and they often persist during redispersion, which greatly reduces the benefits and applicability of the CNM. Full redispersion of cellulose nanofibrils without surface modification or using additives is challenging and often requires extensive mechanical forces such as prolonged high shear mixing that can damage the nanofibrils. [90, 91] Other dewatering techniques that avoid vapor-liquid interfaces include centrifugation, filtration and pressing, which have been used to dewater CNM and microfibrillated cellulose (MCF), [83] but have the common challenge that large driving forces cause macroscopic concentration gradients and hard-to-reverse aggregation. Osmosis and reverse dialysis are less prone to causing heterogeneities and aggregates because they rely on more distributed molecular driving forces and diffusive redistribution of solvent and these methods have been used to dewater nanoparticles, [226] biologics, [227] silk fibroin solutions, [228] and even CNM in preliminary studies. [229, 230] However, prior studies did not directly address the primary concern associated with CNM dewatering: aggregation and redispersion.

In this chapter, we show that reverse dialysis is suitable for dewatering cellulose nanomaterials without compromising redispersibility, as well as for producing polymer/CNM composite gels with well-dispersed nanocellulose at concentrations that are otherwise hard to achieve. We report the dewatering kinetics at different PEG concentrations to highlight an understanding of the underlying processes. TEMPO-CNF suspensions were dewatered and redispersed without using additives or extensive shearing; rheology was used to probe the homogeneity of these samples and to quantify

redispersibility. The generalizability of the reverse dialysis method is demonstrated with suspensions of CNC, chitin nanofiber (ChNF), and polyvinyl alcohol (PVA)/TEMPO-CNF composites. We show that reverse dialysis offers unique opportunities for preparing polymer composite gels with high loadings of well-dispersed nanomaterials and report the operational limitations of this approach.

6.2 Materials and Method

6.2.1 Materials

Suspensions of cellulose nanocrystal (CNC; lot # 2018-FPL-CNC-117) at 10.9 wt% and TEMPO oxidized cellulose nanofibril (TEMPO-CNF; lot # 2018-FPL-CNF-121) at 1.08 wt% were purchased in slurry form from the Process Development Center at the University of Maine, and stored at 4 °C. Chitin nanofiber (ChNF) suspension at 0.5 wt% solids loading was obtained from the lab of Prof. Carson Meredith at Georgia Tech after pressure homogenization. [46] Dialysis tubing (14,000 MW cutoff) was purchased from Ward's Science (Rochester, NY). Polyvinyl alcohol (PVA) of molecular weight 89,000-98,000 (99+% hydrolyzed) and polyethylene glycol (PEG) of molecular weight 35,000 were obtained from Sigma-Aldrich (St. Louis, MO). All TEMPO-CNF used in this study was pressure homogenized (25,000 psi, 7 passes) as described in detail in a previous publication. [231] Two TEMPO-CNF batches were prepared around the maximum operating concentration of 0.5 wt% of the homogenizer: 0.48 wt% (for rotary evaporation experiments) and 0.54 wt% (for reverse dialysis).

6.2.2 Reverse Dialysis

Figure 6.1 shows the reverse dialysis setup used in this study. The material to be dewatered is placed inside the dialysis bag, which is immersed in the polyethylene glycol (PEG) solution. The molecular weight cut-off of the dialysis bag is lower than both the polymer on the outside of the bag and the nanomaterials inside, allowing only water and other small molecules (e.g. salts) to cross the membrane. A previous study has shown that PEG will not diffuse into the dialysis bag if the molecular weight cut-off is correctly chosen. [232] The stir bar (120-200 *RPM*) mixes the surrounding PEG solution to minimize external mass transfer effects; all dialysis experiments were performed at room temperature. Around 15 g of TEMPO-CNF suspension was used for each experiment. The initial volume of PEG solution was 500 mL at concentrations varying from 0 to 30 wt%. Although the PEG solution is diluted slightly by water leaving the sample in the bag, experimental conditions are such that the PEG concentration does not vary by more than 3% during dialysis; for example, the 10 wt% PEG solution remains above 9.7 wt% even if the sample inside the bag is completely dewatered. The total mass of the dialysis bag (bag plus suspension) was tracked during the dewatering process until reaching equilibrium. Before each measurement, the exterior of the bag was drained, rinsed with water and wiped dry using a paper towel. For the dialysis studies of PVA/CNM composite suspensions, a 20 wt% PEG solution was used. The concentrations of the dewatered TEMPO-CNF, CNC and ChNF, and the total solids loadings of PVA/CNF composites were determined by oven-drying. [210] The concentrations of individual components in the PVA/CNF composites were calculated based on the total solids loadings after dialysis and the known mass ratio of TEMPO-CNF to PVA before dialysis.

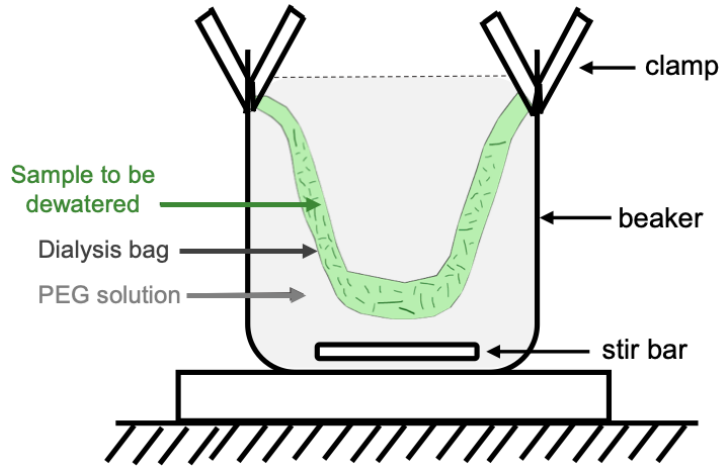

Figure 6.1 Schematic of the reverse dialysis setup in this study; the sample to be dewatered is inside the dialysis bag immersed in the PEG solution; water is transported across the dialysis membrane due to osmotic pressure differences.

6.2.3 Rotary Evaporation of TEMPO-CNF

A rotary evaporator (Heidolph Laborota 4000 efficient, Schwabach, Germany) was used. Two batches of pressure homogenized TEMPO-CNF sample at 0.48 wt% were dewatered at 40 °C to reach 2.05 wt% and 1.45 wt%, respectively, in a two-stage process: 200 mL of the original suspension was placed in a 1 L round bottom flask, and once the sample volume was reduced to less than 100 mL the partly dewatered suspension was transferred to a 250 mL flask to allow for better mixing during final evaporation stages. Under these mild temperature conditions, evaporation took 3 to 4 hours.

6.2.4 Rheological Characterization

Rheological measurements were performed following the procedures described in detail in Section 3.3 on characterization of CNM, using a rotational rheometer (MCR 302,

Anton Paar) with cone-plate geometry, Peltier temperature control (25°C) and an evaporation blocker. [210, 231]

6.2.5 Redispersing TEMPO-CNF After Dewatering

Dewatered TEMPO-CNF samples obtained through reverse dialysis (3.54 wt%, 2.49 wt% and 1.73 wt%) and rotary evaporation (2.05 wt% and 1.45 wt%) were diluted in water (total sample mass 6 g) to the same concentration as the original non-dewatered suspensions (0.54 wt% before reverse dialysis and 0.48 wt% before rotary evaporation); 30 seconds of vortex mixing was used to redisperse the samples. Flow curves were measured at 0, 2, 6 and 26 hours after redispersion to track viscosity changes over time. Before each measurement, the sample was vortexed for 30 seconds to ensure consistent shear history.

6.2.6 Preparing PVA/CNF Composite Gels

PVA solutions at desired concentrations were prepared by dissolving PVA powder in DI water at 95 °C and stirring for at least 1 hour until the solution became transparent and homogeneous. The solution was then cooled to around 40 °C. Two methods were used to prepare the PVA/CNF composite gels with component concentrations of 3.42 wt% PVA and 1.14 wt% TEMPO-CNF. The first method was conventional direct mixing of a 2.49 wt% TEMPO-CNF sample in gel form with the freshly prepared 6.30 wt% PVA solution. This composite is labeled 3.42PVA/1.14CNF_{dial}, with the numerical values referring to mass concentrations of each component and the subscript label indicating that TEMPO-CNF was dewatered via reverse dialysis. This PVA/CNF_{dial} composite was mixed in a beaker for 3 hours, transferred to a vial, and placed on a slow-roller to mix for another 24

hours. The second method was preparing a dilute polymer/CNF suspension first, followed by composite dewatering via reverse dialysis. For example, homogenized 0.54 wt% TEMPO-CNF was added to PVA solution to reach component concentrations of 0.75 wt% PVA and 0.25 wt% TEMPO-CNF. The dilute composite suspension was mixed for 1 hour, transferred to a dialysis bag, and immersed in 20 wt% PEG solution to dewater; the final component concentrations were 3.42 wt% PVA and 1.14 wt% TEMPO-CNF; this sample is abbreviated as $(3.42PVA/1.14CNF)_{dial}$ to indicate that the whole suspension was concentrated using dialysis. Composite gels at other concentrations are all prepared using the second method; the nomenclature for these composites is *x*PVA/*y*CNF where *x* and *y* denote the component concentration in wt%.

6.3 Results and Discussion

6.3.1 Reverse Dialysis Dewatering Kinetics

To understand the water removal kinetics from cellulose nanomaterials with reverse dialysis, the homogenized 0.54 wt% TEMPO-CNF suspension was used as the model system. The mass of the dialysis bag was tracked over time for different PEG concentrations in the dialysis medium. (**Figure 6.2a**) The mass decreases steadily, and eventually reaches an equilibrium plateau. Higher PEG concentrations lead to faster water removal. The mass decreases very slowly at 3 wt% PEG; at 0 wt% PEG, when the dialysis bag is immersed in DI water, the water transport reverses the direction and sample mass increases due to the osmotic pressure of the CNM suspension. Higher PEG concentrations also lead to smaller equilibrium masses, because greater osmotic driving forces exist to draw water out. A previous study that used reverse dialysis to dewater

polymer/nanoparticle suspensions at different dextran concentrations observed similar trends but provided an incomplete picture at long times. [226] The kinetics of the dialysis process depend on the magnitude of the driving force (i.e. osmotic pressure difference), and mass transfer rates; in addition to the external PEG concentration, therefore other factors like the TEMPO-CNF starting concentration, PEG solution viscosity, and stir bar speed may also affect kinetics.

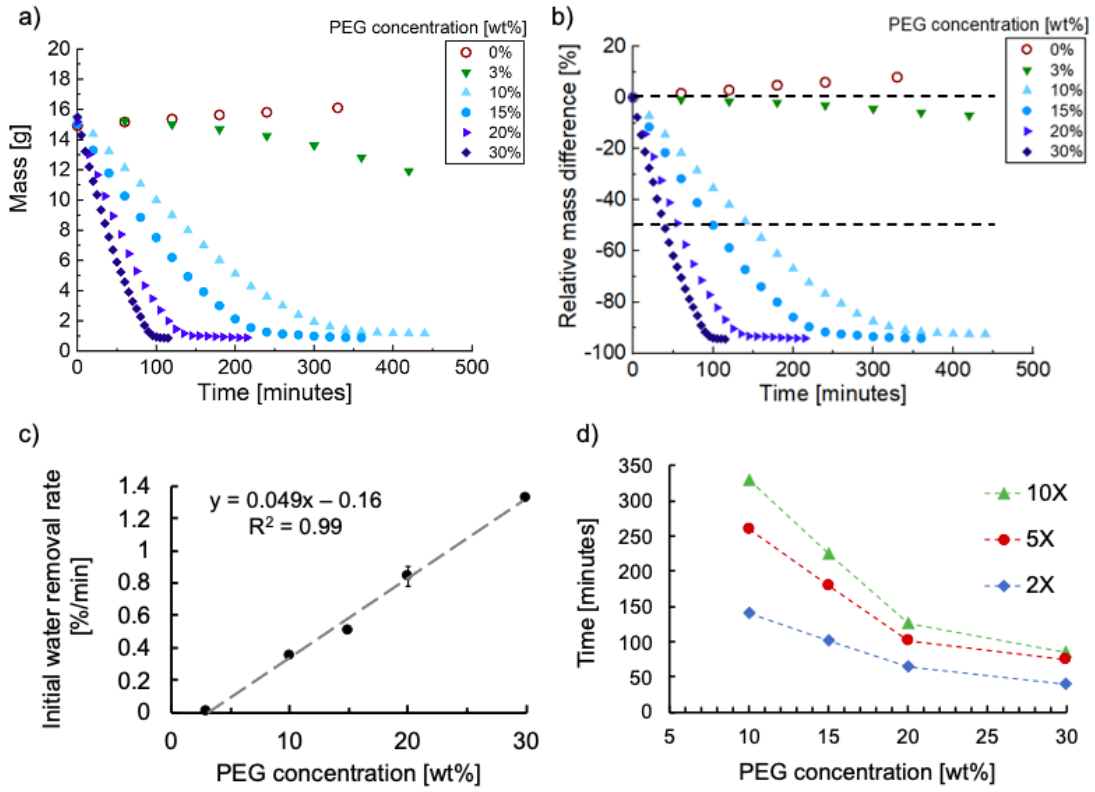

Figure 6.2 Kinetic profiles for dewatering TEMPO-CNF suspension through reverse dialysis against PEG solutions at different concentrations. All suspensions have starting mass of ~ 15g and starting concentration of 0.54 wt%; stir speed is 120 *RPM*. (a) Mass of dialysis bags and samples as function of time with targeted starting mass of 15 g. (b) Relative mass difference as function of time. (c) Initial water removal rates as function of PEG concentration, including linear fit. (d) Time needed to reach 2, 5 and 10-fold concentration increase at different PEG concentrations. The lines connecting the data points are provided to guide the eye.

To facilitate comparison of samples with slightly different starting masses, the relative mass difference was compared which was calculated as $(m_t - m_{t_0})/\, m_{t_0}$, where m_t is the time-dependent mass during the dialysis, and m_{t_0} is the initial mass. (**Figure 6.2b**) Reverse dialysis can remove more than 90% of water from the initial TEMPO-CNF suspension, increasing the concentration by more than 10 times. Unlike ultrafiltration, the dewatering rate is preserved even when over 60% of the water is removed. To quantify the initial water removal rates, a linear fit to the data points between 0 and -50% was used to extract the initial water removal rate (**Figure 6.3**, for data fit). **Figure 6.2c** shows the water removal rates as a function of PEG concentration. The experiment at 20 wt% PEG was performed in triplicate to assess process variations and the error bar represents the standard deviation. Process variations were found to be small and the initial water removal rate varies linearly with the PEG concentration.

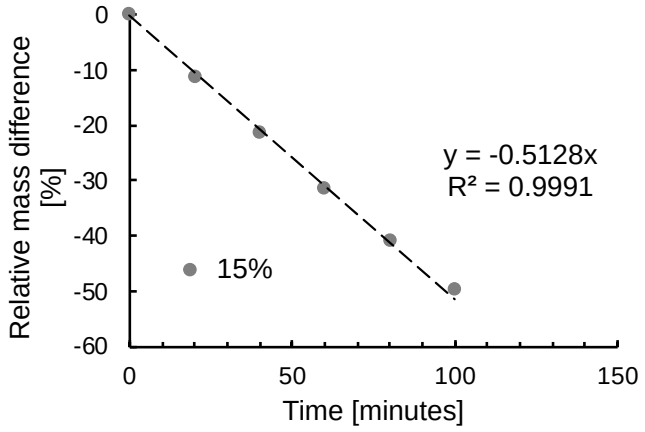

Figure 6.3 The profile of relative mass difference between 0 and -50% for dialysis of 0.54 wt% TEMPO-CNF against 15% PEG; linear fit is imposed with intercept fixed at 0 and the absolute value of the slope, 0.5128 [%/min], is defined as the initial water removal rate.

The kinetics of dialysis depend on the magnitude of the driving force (i.e. osmotic pressure difference), and mass transfer rates. Therefore, in addition to the external PEG concentration, other factors like the TEMPO-CNF starting concentration, PEG solution viscosity, and stir bar speed may also affect the kinetics. Using an initial TEMPO-CNF concentration of 0.27 wt% leads to a slightly larger osmotic pressure difference with the surrounding PEG solution; as compared to the 0.54 wt% sample, the initial water removal rate is similar, and the equilibrium mass loss at the end of the dialysis is slightly larger. (**Figure 6.4a**) In another experiment, it was found that a higher stirring speed of 200 *RPM* does speed up the dialysis process slightly by enhancing external mass transfer, while the equilibrium mass difference is similar. (**Figure 6.4b**) This observation is expected: the stir speed affects external mass transfer coefficient and thus enhances water transport, but the final mass loss is determined by the concentration of TEMP-CNF and PEG, which were unchanged. Overall, it can be concluded from the experiments that the reverse dialysis kinetics is most significantly affected by the PEG concentration, and to much lesser degree by the initial TEMPO-CNF concentration and stir speed, which were therefore not studied in further detail.

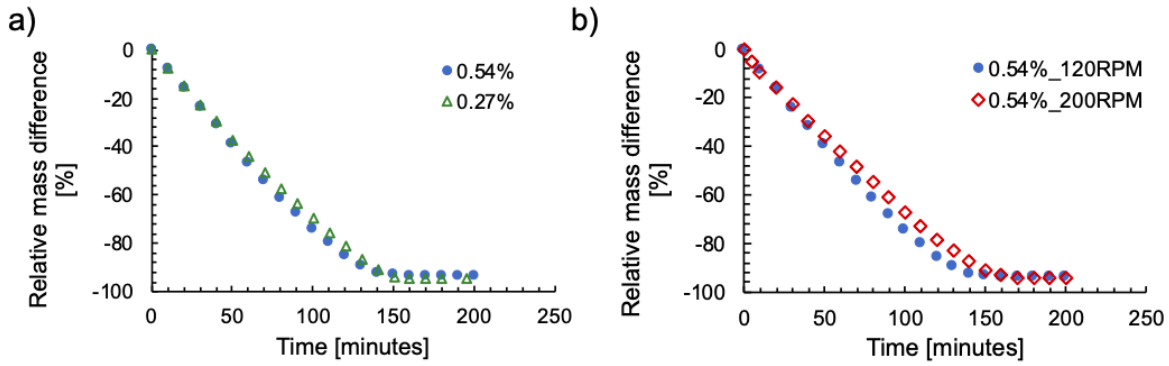

Figure 6.4 Kinetic profiles of reverse dialysis using 20% PEG solutions: a) TEMPO-CNF suspension with initial concentrations of 0.27 wt% and 0.54 wt% 120 *RPM* stir speed. b) TEMPO-CNF of 0.54 wt% at 200 *RPM* and 120 *RPM* stirring speeds. The relative mass difference (same as in the Figure 6.2b) was used to normalize the starting mass, which is calculated as $(m_t - m_{t_0}) / m_{t_0}$, where m_t is the time-dependent mass during the dialysis, and m_{t_0} is the initial mass.

Figure 6.2d summarizes the reverse dialysis data to highlight the time needed to reach 2, 5 and 10-fold concentration increases relative to the starting value (0.54 wt%) using PEG solutions of different concentrations. Although the water removal time depends on other factors, such as the amount of starting material, bag surface area to volume ratio and stirring speed, the figure can guide the design of dewatering processes based on reverse dialysis. For example, using solutions with 20% PEG rather than 10% drastically decreases the water removal time; a further increase to 30% PEG does not decrease the time as significantly, even though a 30% PEG solution has a much larger osmotic pressure than a 20% solution (the osmotic pressure follows a non-linear 3rd order polynomial relationship with the PEG concentration according to van't Hoff's law for non-ideal polymer solutions). [233] The high viscosity of the 30% PEG solution hinders diffusive and convective mass transfer during the dewatering process and counteracts the increased driving force.

6.3.2 Dewatering and Redispersibility of TEMPO-CNF

Reverse dialysis can be used to obtain homogenous samples of high concentrations. In addition to visual inspection, which can detect large aggregates, rheological characterization was performed to assess the homogeneity and redispersibility of the dewatered samples. Rheology measures the bulk properties, and is very sensitive to microstructural changes without the sample size bias associated with, for example, electron microscopy. In contrast to light scattering, rheology can also be applied to samples across a wide range of concentrations. Previous studies have analyzed the redispersibility of dried CNF by measuring the rheological properties, including viscosity and oscillatory moduli. [90-92] **Figures 6.5a and 6.5b** show the rheology of dewatered TEMPO-CNF samples up to very high concentrations. At 0.54 wt% and 0.79 wt% the suspensions are in the viscoelastic regime, with $G'' > G'$ and flow curves that exhibit a low-shear plateau and shear thinning at higher shear rates. At 1.15 wt%, the suspension passes through the gelation transition, with G'' close to G' across the entire frequency range. At higher concentrations, the TEMPO-CNF suspensions are strong gels, with $G' >> G''$ and both moduli nearly constant across the whole frequency range. Good reproducibility and absence of hysteresis during flow curve measurements indicate excellent dispersion in these samples. To further evaluate the microstructural homogeneity of the samples, the scaling of G' and G'' at 1 rad/s with CNF concentration was determined (**Figure 6.5c**). The well-defined power-law scaling across the concentration range are consistent with having well-dispersed samples; if aggregation had occurred at high concentrations, a change in scaling exponent would have been expected. The same relationship was reported in previous studies where CNF samples were prepared by dilution only. [154, 156] These data

indicate that the dewatered samples prepared by reverse dialysis of dilute stock solution have similar homogeneity as those prepared by diluting from concentrated stock solutions that had been treated with significant shear to remove aggregates.

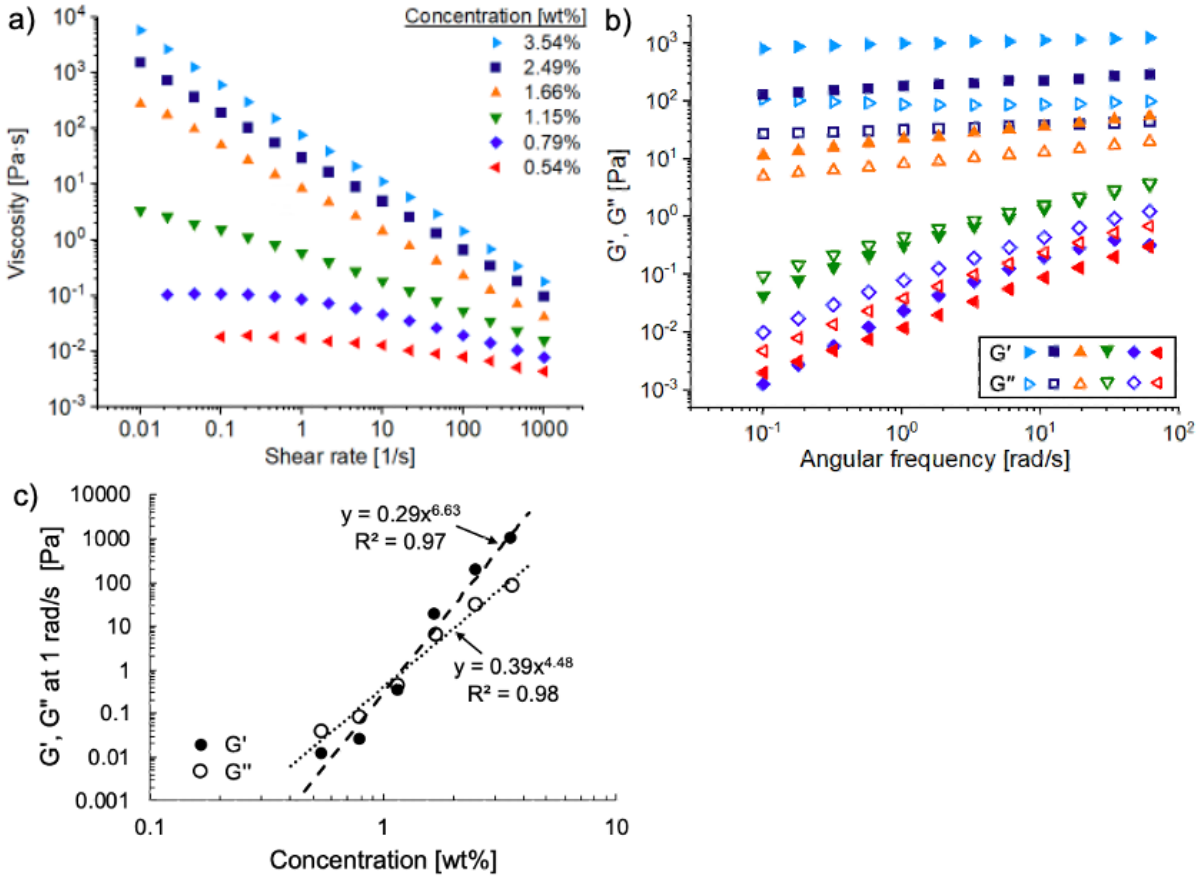

Figure 6.5 The (a) Steady shear flow curves and (b) oscillatory frequency sweeps for TEMPO-CNF suspensions after dewatering via reverse dialysis; the starting concentration before dewatering was 0.54 wt% for all samples. (c) Scaling of G′ and G″ with concentration, showing a well-defined power-law relationship.

Though reverse dialysis can produce well-defined, homogeneous samples, a key concern of using dewatered cellulose nanomaterials is their redispersibility after diluting back with water, as is often needed in applications, as explained in the Introduction section. TEMPO-CNF was chosen as the primary material to study the dewatering and redispersibility, because nanofibrils is particularly prone to aggregation due to its large

fibril surface area. [234] To assess the effects of dewatering on redispersibility, two batches of TEMPO-CNF suspension were pressure homogenized at concentrations of ~0.5 wt% (maximum concentration for homogenization), and then separately dewatered by reverse dialysis and rotary evaporation, respectively. Both methods can remove most of the water from the suspension without fibril losses. The fully dispersed, homogenized samples prior to dewatering serve as the reference for comparison with the samples that are redispersed after dewatering and diluted back to their original concentrations. **Figure 6.6** shows the flow curves of redispersed TEMPO-CNF at several time points for the two methods, presenting the non-dewatered suspensions as reference. Both dewatering methods achieved concentration increases of ~4x (4.6x for reverse dialysis, 4.3x for evaporation); viscosities are highest immediately after redispersion, and much larger than the reference sample values (3-5x increase in low-shear viscosity), which indicates that many fibrils are initially entangled and/or aggregated after redispersion. For the reverse dialysis sample, the redispersed viscosity quickly decreases and is nearly identical to the reference sample after 26 hours. (**Figure 6.6a**) In contrast, for TEMPO-CNF dewatered via rotary evaporation, the viscosity change after redispersion is much slower and never reaches the reference viscosity again; after 26 hours, the low shear viscosity remains ~3x larger than prior to dewatering. (**Figure 6.6b**) These data show clearly that samples dewatered via reverse dialysis require some time for to fully untangle and rehydrate after redispersion, but do not exhibit irreversible aggregation. Dewatering via rotary evaporation, on the other hand, leads to formation of aggregates that cannot be redispersed without the application of prolonged high shear mixing, risking damaging and altering the nanofibrils.

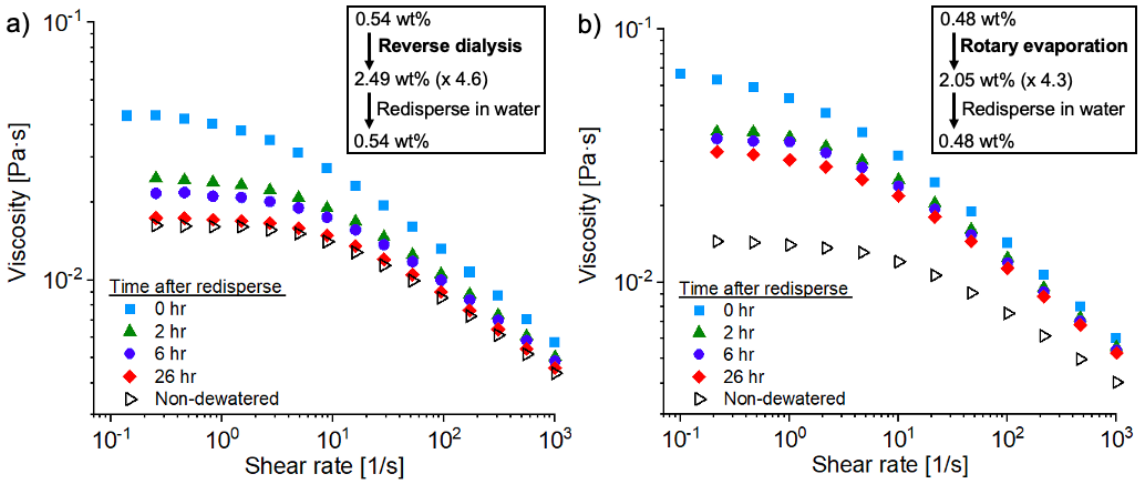

Figure 6.6 Evolution of flow curves of TEMPO-CNF samples after dewatering (~4x concentration increase) and redispersion to their original concentrations via (a) reverse dialysis (0.54 wt%) and (b) rotary evaporation (0.48 wt%); the non-dewatered original TEMPO-CNF suspensions (open triangles) serve as reference for the dewatered and redispersed samples.

To quantify the viscosity differences between the redispersed suspensions and the non-dewatered reference samples, each flow curve is fitted to the Cross model to extract the zero-shear viscosity η_0. The relative difference between η_0 for the redispersed sample and the reference sample $(\eta_0 - \eta_0^{ref})/\eta_0^{ref} \times 100\%$ is an indicator for redispersibility. (**Figure 6.7** and sample calculations). The η_0 is obtained by fitting the Cross model where η_∞ is the known water viscosity at 25 °C; η_0 is the suspension viscosity in the limit of zero shear rate; λ is the characteristic time scale of the system, and m is the shear-thinning index. η_0 at 0 hour of redispersed 0.54 wt% from 2.49 wt% is 0.05047 Pa·s. η_0 of non-dewatered 0.54 wt% reference suspension is 0.01713 Pa·s. The η_0 difference between the redispersed and the reference is thus (0.05047 – 0.01713)/0.01713 x 100% = 194.6%

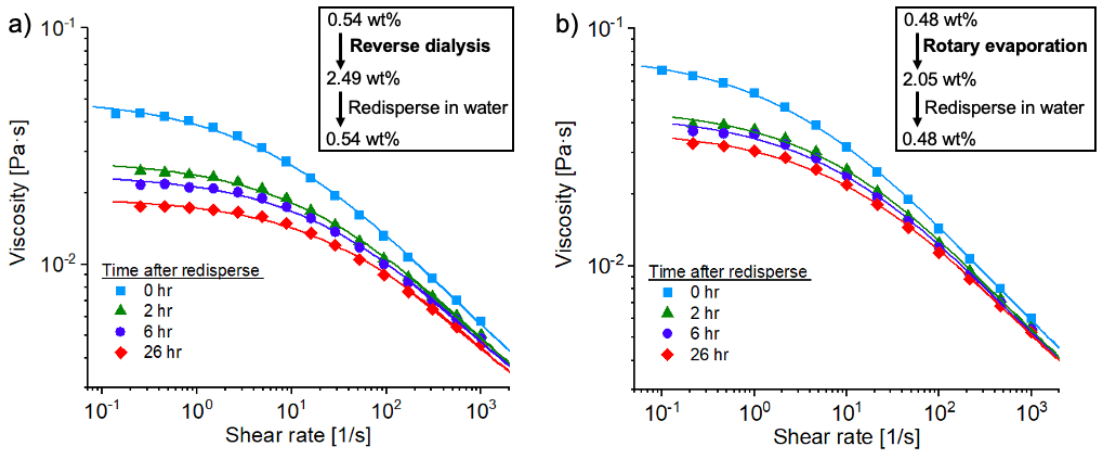

Figure 6.7 Flow curves fitted by the combined model to extract the η_0 and calculate the redispersibility relative to the reference.

Table 6-1 shows these data as a function of time after redilution for four samples: two that were dewatered via reverse dialysis (from 0.54% to 2.49% and 1.73%, respectively) and two that were dewatered via rotary evaporation (from 0.48% to 2.05% and 1.45%, respectively). For dewatering via reverse dialysis, the η_0 difference immediately after redilution is high, but it rapidly decreases. The difference between dewatered-then-rediluted samples and the reference sample is less than 10% difference at 26-hour, which falls within the range of anticipated experimental reproducibility errors of these rheological measurements for viscoelastic samples (~10% variations can typically be expected due to loading effects, etc). Thus, after slightly more than 24 hours, these samples are essentially indistinguishable from the reference, indicating that the TEMPO-CNF fibrils are fully redispersed if given time to rehydrate and untangle. For rotary evaporation, the η_0 differences are much larger and do not fully recover. The final differences are well outside the rheological measurement errors, suggesting that significant aggregation still exist. Note that due to batch-to-batch variations in the homogenization process, the rotary evaporation experiments were performed with a slightly lower initial concentration than

reverse dialysis (0.48 vs 0.54%), which should make redispersion of the rotary evaporation sample slightly easier. In spite of this bias, reverse dialysis was found to prevent irreversible aggregation much better than rotary evaporation.

Table 6-1 Comparing zero-shear viscosity of dewatered-then-redispersed TEMPO-CNF suspensions relative to the homogenized non-dewatered reference samples for two different dewatering processes: reverse dialysis and rotary evaporation; two different levels of dewatering were tested for each method. Experimental error range for rheological characterization of these TEMPO-CNF samples is expected to be ~10%. The starting concentrations of the materials before dewatering were slightly different due to batch-to-batch variations associated with pressure homogenization.

Dewater method	Reverse dialysis		Rotary evaporation	
CNF concentration before dewatering	0.54 wt%		0.48 wt%	
CNF concentration after dewatering	2.49 wt%	1.73 wt%	2.05 wt%	1.45 wt%
Concentration increase	x 4.6	x 3.2	x 4.3	x 3.0
CNF concentration after redisperse	0.54 wt%		0.48 wt%	
Time after dilution [Hour]	Relative difference of zero-shear viscosity η_0 w.r.t. non-dewatered sample			
0	194.6%	111.0%	405%	214.1%
2	55.9%	29.7%	199.2%	121.5%
6	34.6%	25.6%	180.5%	86.5%
26	*5.8%*	*9.3%*	141.3%	78.7%

The excellent redispersibility after dewatering via reverse dialysis may be attributed to the absence of a vapor-liquid interface, which is known to cause irreversible aggregation, and to the more uniform removal of water through osmotic processes. [235, 236] Reverse dialysis could potentially be added as a secondary dewatering step during the

manufacturing of CNM after ultrafiltration reaches its concentration limits, thus enabling further dewatering to increase the solids content. For manufacturing dry powdered CNM, reverse dialysis also has potential benefits: it can be performed prior to the final drying step (e.g. freeze drying) to improve redispersibility of the fully dried CNM samples. A previous study showed that partial dehydration via evaporation followed by freeze drying improved redispersibility of freeze-dried CNF.[89] Based on the advantages that reverse dialysis offers relative to evaporation, further enhancements of redispersibility of fully dried CNM samples may be feasible if reverse dialysis is used to pre-concentrate the suspensions before drying.

For large scale applications, the PEG solution that is used to drive the dewatering process can be recycled using ultrafiltration to remove the absorbed water and bring the PEG concentration back to the initial level. The viscosity of a 20 wt% PEG solution (35k molecular weight) is 0.15 Pa·s, which is easily flowable. Moreover, the highly soluble PEG molecules will not aggregate and block the filtration membrane during the re-concentration process.[237-239] When reverse dialysis is combined with a closed-loop reconcentration process for the PEG solution, the overall process is sustainable in terms of limited PEG material needs. The integrated process also offers the typical energy benefits of membrane-based processes relative to other water removal processes; the reverse dialysis occurs spontaneously, and energy is only required to reject the removed water from the system via PEG ultrafiltration.

Previous studies did not quantify redispersion behavior as rigorously as in this study, but qualitatively it is clear that researchers observed even more significant redispersibility issues than we report here: the viscosity and/or oscillatory moduli of the

redispersed suspensions in some prior studies were smaller than the non-dried reference samples, [90-92] which is contrary to our observation that redispersed suspensions with aggregation issues have larger viscosities. This is likely because our suspensions were only partially dewatered, whereas the other studies used completely dried nanofibrils. Fully dried nanofibrils are much more aggregated and their surface area is greatly reduced. Upon redispersion, these highly aggregated suspensions form fewer entanglements, leading to lower viscosities. Meanwhile, partially dewatered suspensions enhance nanofibril interactions and entanglements, resulting in higher viscosity. The viscosity then decreases as fibrils gradually redistribute themselves upon dilution, unless their aggregation is irreversible, as was found for the samples that were dewatered via rotary evaporation. The slow viscosity decrease in our studies associated with microstructural rearrangements is also observed when the commercial TEMPO-CNF slurry product is diluted. [166, 231]

6.3.3 Reverse Dialysis to Dewater CNC, ChNF and Composite Gels

In addition to TEMPO-CNF, suspensions of CNC and ChNF can be prepared at high concentrations using reverse dialysis. **Figure 6.8a** summarizes the concentrations that were achieved for these other materials and their shear viscosities at 1 s^{-1} as an indicator of rheological properties. The full flow curves and the frequency sweeps for CNC and ChNF are presented in **Figure 6.9** and **Figure 6.10**. It should be noted that the highest CNC concentration in **Figure 6.9a** is 23.1 wt%, which doubles the concentration of the commercially available CNC slurry; even higher concentrations can be achieved with reverse dialysis, but the rheological properties become difficult to measure. For example,

CNC sample of 45.6 wt% becomes clay-like (**Figure 6.11**), so that removing it from the dialysis bag and loading into the rheometer were challenging. Reverse dialysis is clearly suitable for dewatering several cellulose nanomaterials, thus providing more options for processing these materials when redispersibility is critical.

An important advantage of reverse dialysis is that it can also be used to directly prepare well-dispersed polymer/CNM composite gels by dewatering pre-mixed, dilute composite suspensions. In contrast, these systems are usually prepared by either mixing two concentrated components (polymer solution and CNM suspension), or by adding one component in dry form to a suspension of the other component; both options present significant dispersion and mixing challenges. For this study, we selected PVA/TEMPO-CNF as a model system. PVA is a highly water-soluble polymer that is compatible with cellulose nanomaterials and the PVA/nanocellulose composite gels have been produced for various applications, with dispersion of the nanomaterials often being a primary concern. [240-243] TEMPO-CNF was selected because its long fibrils are more challenging to disperse in polymer solutions than the much shorter CNC nanoparticles.

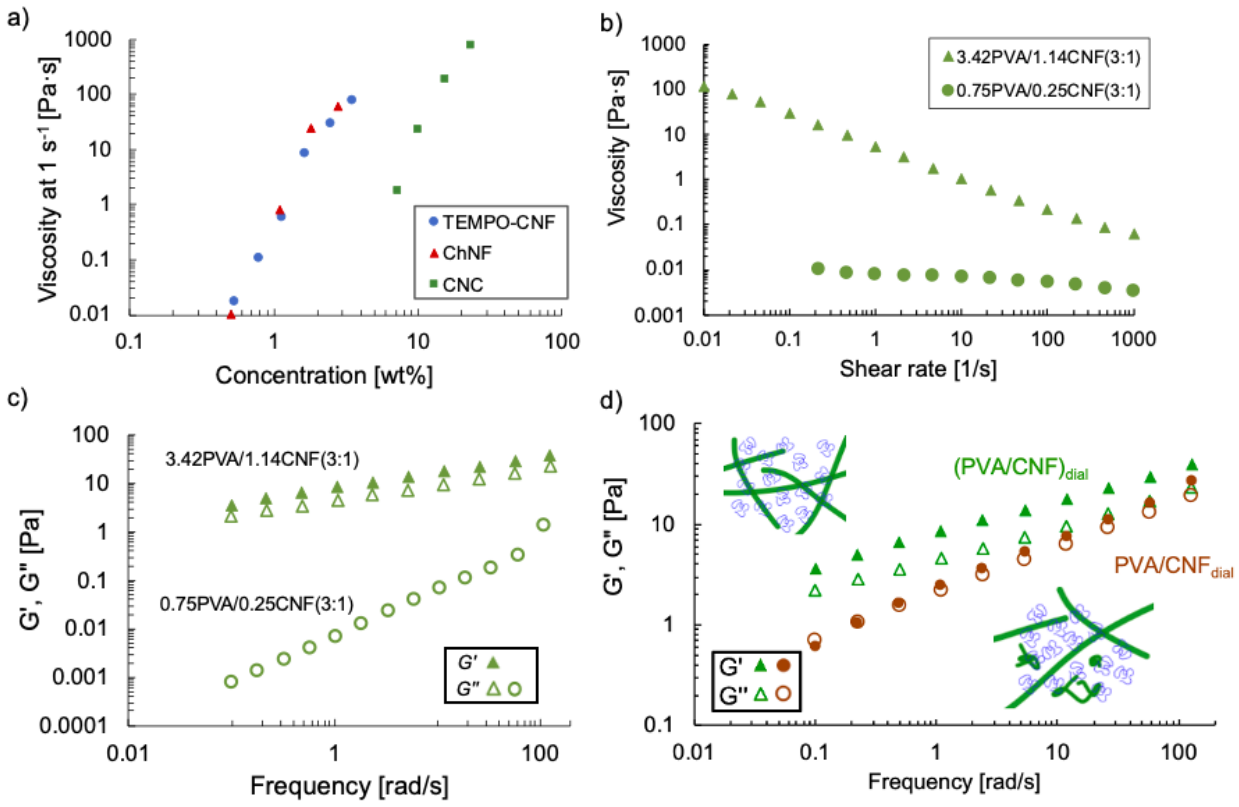

Figure 6.8 (a) Summary of shear viscosity at 1 s^{-1} for TEMPO-CNF, CNC and ChNF as a function of concentration in dewatered sample prepared via reverse dialysis; the upper limits of the concentration ranges represent the maximum for which rheological properties could be measured, and are not the limits of the dialysis process. Flow curves (b) and frequency sweeps (c) of PVA/CNF composite suspensions before reverse dialysis (dilute) and after dewatering (concentrated). (d) Frequency sweep of PVA/CNF composite gels prepared by different methods; reverse dialysis of a dilute composite suspension, $(3.42PVA/1.14CNF)_{dial}$, leads to a stronger, more well-dispersed gel than mixing of individually prepared concentrated components, $3.42PVA/1.14CNF_{dial}$.

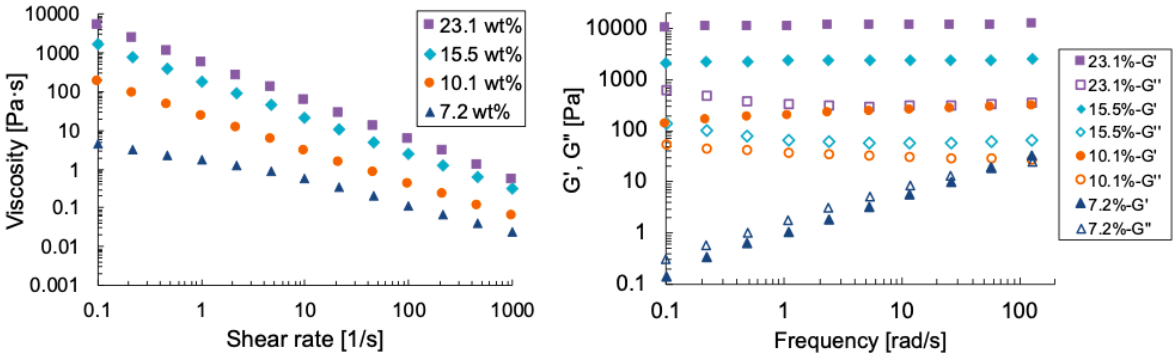

Figure 6.9 CNC flow curves and oscillatory frequency sweeps at higher concentrations for samples dewatered via reverse dialysis.

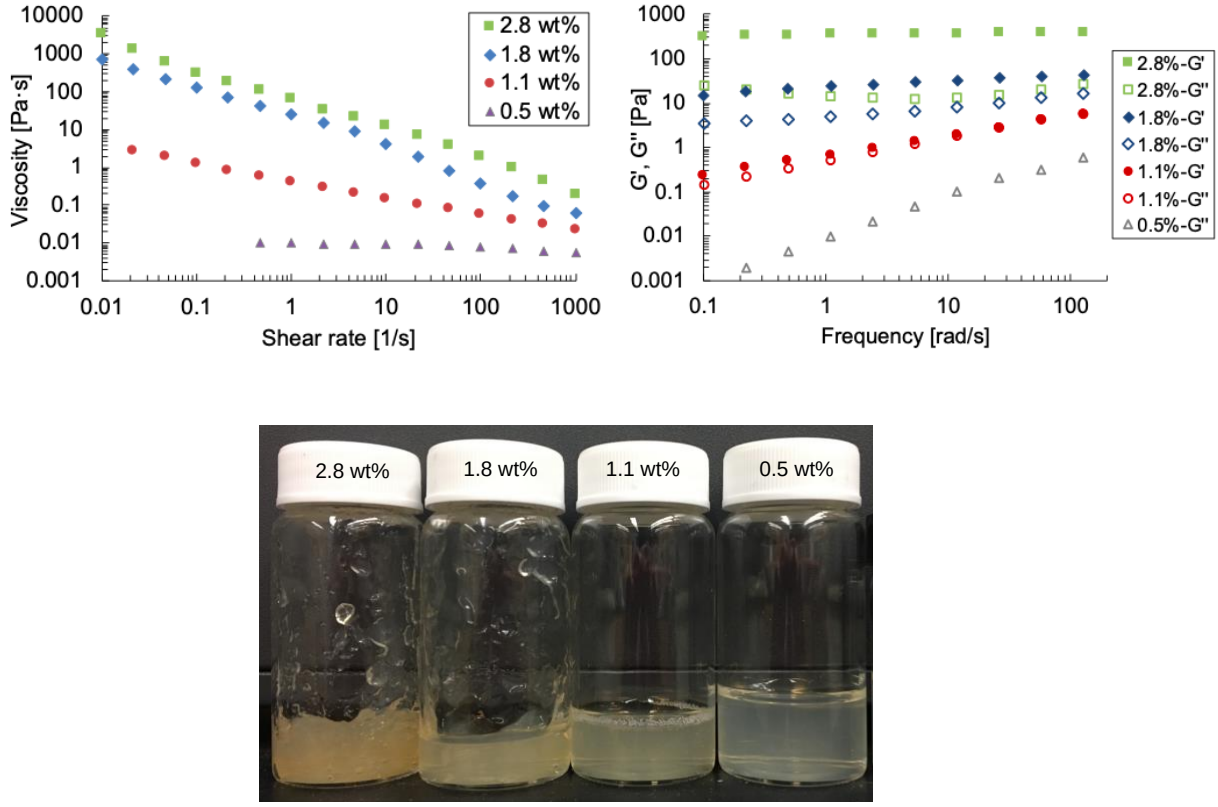

Figure 6.10 ChNF flow curves and oscillatory frequency sweeps at higher concentrations for sample dewatered via reverse dialysis; 0.5 wt% is the original suspension.

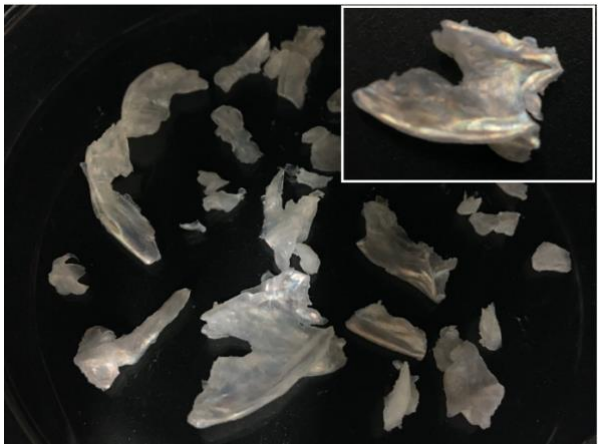

Figure 6.11 CNC suspension of 45.6 wt% is achieved by reverse dialysis. The inset shows the zoomed in view of a small piece of material with birefringent pattern. The images were taken without polarizer.

The suspensions with two different polymer:CNF ratios (3:1 and 1:1.08) were dewatered using the reverse dialysis to prepare composite gels. Before dialysis, both 0.75PVA/0.25CNF (0.75 wt% PVA and 0.25 wt% CNF in water) and 0.5PVA/0.54CNF are Newtonian fluids with constant viscosity and are easy to disperse. (**Figures 6.8b and 6.8c**) Water was then removed from the suspensions to form composite gels. 0.75PVA/0.25CNF was dewatered to 3.42PVA/1.14CNF (4.6x concentration increase); the dewatered sample is in gel phase. 0.5PVA/0.54CNF was dewatered to 1.82PVA/1.96CNF (concentrated 3.6x), which is a very strong gel due to the high CNF loading. (**Figure 6.12**). The gels both looked homogenous and clear with little aggregation; rheological measurements also supported the expectation of excellent dispersion of TEMPO-CNF.

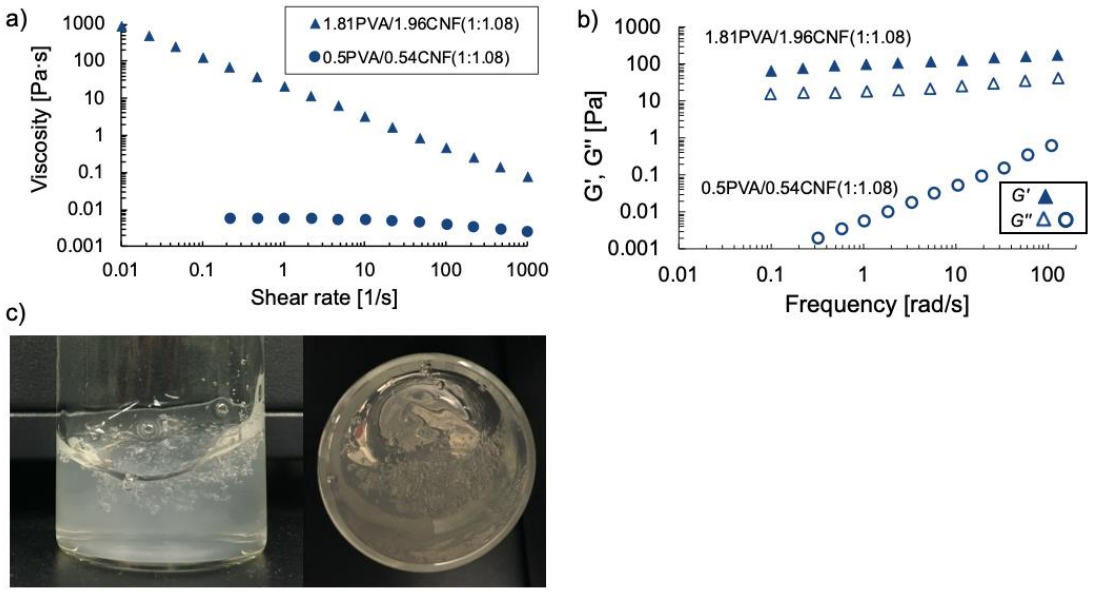

Figure 6.12 Properties of sample that was dewatered from 0.5PVA/0.54CNF to 1.82PVA/1.96CNF via reverse dialysis. The a) viscosity and b) oscillatory frequency sweep data show that the dewatered sample is a strong gel. c) Images of the dewatered sample in the vial show that it is homogenous.

As TEMPO-CNF has a low gelation concentration, preparing PVA/CNF composites with high TEMPO-CNF loading while maintaining good dispersion is extremely challenging. Mixing aqueous TEMPO-CNF and PVA suspensions ensures dispersion, but limits the loading range. [240] Mixing dried TEMPO-CNF in PVA solution can be used to prepare gels of high loading, [243] but dispersion is poor as the aggregates caused by drying persist. To illustrate the contrast in dispersion, 3.42PVA/1.14CNF was prepared via two methods, both involving reverse dialysis. The $(3.42PVA/1.14CNF)_{dial}$ composite gel was prepared by dewatering the whole suspension, while $3.42PVA/1.14CNF_{dial}$ was prepared by directly mixing the PVA solution and a pre-concentrated 2.49 wt% TEMPO-CNF suspension, as described in the Methods section. Though we established in the first part of this paper that the TEMPO-CNF sample at 2.49% has no redispersibility issues, mixing this gel with a viscous PVA solution still causes

significant dispersion problems for composite preparation. **Figure 6.8d** and **Figure 6.13** show that the mixed composite is near the gelation transition ($G' \simeq G''$), whereas the dewatered composite is in the gel phase ($G' > G''$) and stronger. We do not report rheological data for the control experiment in which the composite mixture was prepared by adding dry polymer powder to a 1.14 wt% TEMPO-CNF suspension, because we were unable to prepare samples that looked sufficiently homogeneous to warrant characterization.

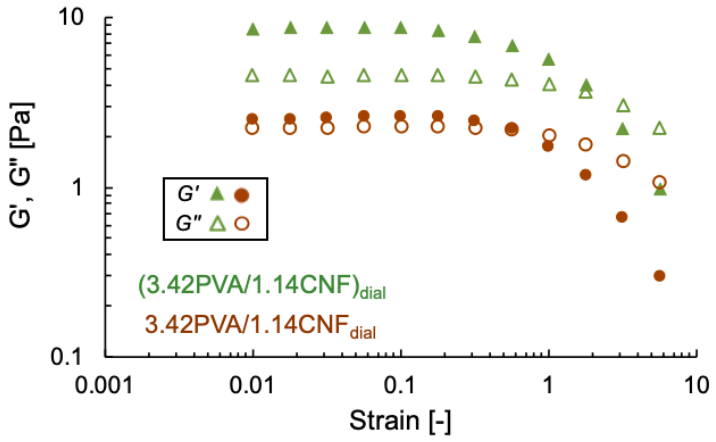

Figure 6.13 Strain sweep of 3.42PVA/1.14CNF$_{dial}$ and (3.42PVA/1.14CNF)$_{dial}$ showing that the G′ and G″ of (3.42PVA/1.14CNF)$_{dial}$ cross-over happens at a higher strain.

Although reverse dialysis is an excellent method to prepare well-dispersed polymer/CNM composite gels at CNM concentrations that cannot readily be achieved with other techniques, there are limitations regarding concentrations and polymer/CNM ratios. The presence of polymer inside the sample reduces the osmotic pressure difference relative to the outside PEG solution, and polymer film formation near the membrane surface can hinder water transport through the dialysis bag. [244] Examples are shown in the Supporting Information. For a high polymer concentration, the water removal slows down

dramatically (for example 4.75PVA/0.25CNF vs 0.75PVA/0.25CNF). (**Figure 6.14**) In highly concentrated polymer solutions, film formation at the surface of the dialysis was observed, both with a pure PVA solution at 4.75 wt% and a 4.75PVA/0.25CNF composite suspension as starting material. The resulting heterogeneity inside the dialysis bag, which is not observed with starting materials at a lower polymer concentration and which is not caused by the nanomaterials or their interactions with the polymer, slows down dialysis processes and leads to macroscopic concentration gradients in the dialyzed sample. (**Figure 6.15**) Further investigation of this phenomenon will be needed if such high polymer concentrations are needed in starting solutions.

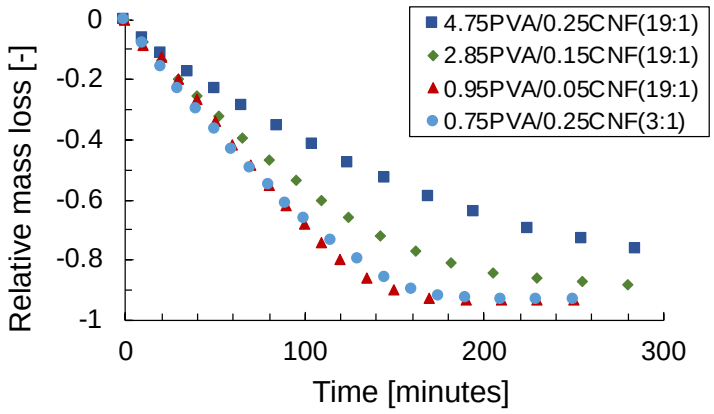

Figure 6.14 Reverse dialysis kinetics profile of dewatering PVA/CNF composite suspensions of different concentrations. Higher PVA concentration slows down the dewatering process as film formation hinders water transport.

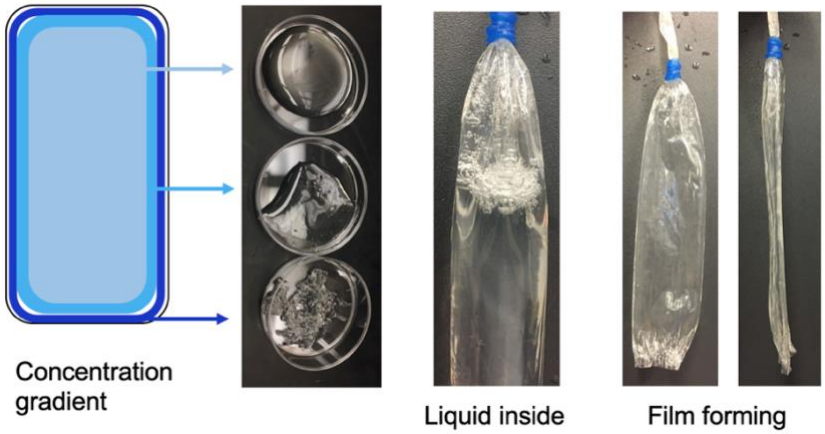

Figure 6.15 Reverse dialysis of 4.75PVA/0.25CNF results in film formation on the outer layer and inside is still liquid suspension.

6.4 Conclusions

A well-controlled dewatering process for cellulose nanomaterials and their polymer composite suspensions is achieved by reverse dialysis, which removes water via liquid-liquid transport through a membrane. The sample to be dewatered is inside a dialysis bag immersed in a concentrated polymer solution (PEG in this study). The dewatering process is driven by the osmotic pressure difference, which is significantly affected by the concentration of the PEG solution. Suspensions of CNC, ChNF and TEMPO-CNF can all be dewatered to high concentrations via reverse dialysis. TEMPO-CNF was chosen to investigate the homogeneity and redispersibility of the dewatered samples in detail as the long fibrils in this material are known to be prone to aggregate during dewatering processes. Rheological measurements show that dewatered TEMPO-CNF samples remain homogenous from 0.54 to 3.45 wt% when reverse dialysis is used. To check redispersibility, the dewatered TEMPO-CNF samples were diluted back to their initial

concentrations prior to dewatering, and the viscosity was measured at different time points to track the redispersion process. The relative difference of zero-shear viscosity η_0 between the dewatered-then-rediluted and the reference samples, was used as an indicator for redispersibility. The difference was very small for samples dewatered via reverse dialysis, indicates that concentrated TEMPO-CNF suspensions prepared via reverse dialysis are fully redispersible if given time to rehydrate and untangle. Dewatering via rotary evaporation, however, leads to much larger and persistent η_0 differences, suggesting that significant irreversible aggregation exist. Thus, reverse dialysis can be potentially added after the ultrafiltration step in CNM manufacturing to produce more concentrated products. The reverse dialysis can also prepare well-dispersed polymer/CNM composite gels by dewatering the pre-mixed, dilute composite suspensions. The PVA/CNF composites gel prepared by dewatering of a dilute composite mixture is shown to be stronger and more flexible than the gel prepared by directly mixing the two concentrated components, indicating that the TEMPO-CNF is better dispersed in the dialyzed composite. Overall, the reverse dialysis is a simple, versatile and well-controlled dewatering method that can be applied to many naturally extracted nanomaterials without compromising redispersibility, and can prepare well-dispersed nanomaterials in polymer composite gels at high concentrations that are otherwise difficult to achieve.

CHAPTER 7. CONCLUSIONS AND RECOMMENDATIONS

This chapter summarizes the motivation, major findings, conclusions and recommendations for future work related to the rheological characterization and modeling of cellulose nanomaterials, the reverse dialysis method, and quantification of nanocellulose redispersibility using rheology.

Cellulose nanomaterial (CNM) is a class of sustainable nanomaterials that increasingly gained interest from both academic research and industrial application in the past 10 to 20 years. It is produced from the abundant cellulose sources such as wood and plant, and it is a high molecular weight biopolymer with hydroxyl groups. Two main types of CNM are cellulose nanocrystal (CNC) – rigid rod-like nanoparticles, and cellulose nanofibril (CNF) – flexible fibrils of larger length and aspect ratio. Because of their sustainability, morphology and tunable surface chemistry, CNM has been used for many applications such as rheological modifiers, hydrogels and composites. In spite of the benefits, one of the key challenges that hinders the commercialization of the CNM is lacking a rapid and reliable characterization method for quality control. Because the key properties of CNM such as morphology and surface charge vary from batch to batch, a robust quality control method is critical to ensure reproducibility and consistent product quality. Rheology can be an alternative quality control method compared to currently used characterization methods such as electron microscopy, which is expensive and time-consuming. The literature has reported rheological studies on the concentration, temperature and ionic strength effect of CNC, and has characterized TEMPO oxidized cellulose nanofibril (TEMPO-CNF) of different morphologies and surface charges.

Nevertheless, there is still a knowledge gap that translates the lab-scale rheological characterization to the industrial-scale quality control. Two challenges that must be resolved are robust test protocols to obtain reliable data, and rheological models and parameters for direct comparison or identification.

7.1 Conclusions

Chapter 3 provides detailed test protocols to ensure obtaining robust and accurate rheological data, which includes sample preparation and viscosity measurement procedures. Vortex mixing was studied to prepare homogenous samples while preserving microstructure, that can be destroyed by alternative methods like high-power sonication and homogenization. To determine the concentration gravimetrically, the sample after oven-drying is equilibrated in a TAPPI standard temperature-controlled room to reduce variations caused by fluctuating temperature and humidity of the surrounding environment. The rheological test protocol includes guidelines on sample loading, pre-shear and interval time setup to ensure measurement reproducibility. A key finding is that when the shear viscosity is probed in three shear intervals, hysteresis provides a valuable indicator on thixotropy and sample homogeneity. Shear viscosity and oscillatory rheology results were then presented for CNC as function of concentration, ionic strength and temperature, and for TEMPO-CNF as function of concentration and temperature. With the protocols used in this thesis, no wall-slip effects were detected; flow curves obtained with different geometries were found to overlap. These rheological results provide new insights about the phase behavior across concentrations, how the electrostatic interactions between particles are affected by temperature for CNC and TEMPO-CNF suspensions, and the role of salt (residual and added) on the interactions (incl. gelation) in CNC suspensions.

In Chapter 4 we developed a new rheological model relevant to quality control based on the rheological data measured in the previous chapter. The model, $\eta = a\dot{\gamma}^{-b} + \eta_\infty + \frac{\eta_0 - \eta_\infty}{1+(\lambda\dot{\gamma})^m}$, which combines the power law and the Cross model, accurately describes the flow curves over the full range of shear rates across concentrations for both CNC and TEMPO-CNF. The model parameterizes the viscosity data for quick comparisons of different flow curves using all data rather than selectively using viscosity values at specific, somewhat arbitrarily chosen shear rates, as is often done in the literature. By using all available viscosity data, a more robust characterization of the material can be made, which also facilitates quantitative comparison of different samples. Key model parameters η_0 and λ correlate well with the suspension concentrations. This model can be used to estimate the concentration of an unknown CNM sample, with errors of less than 0.2 wt% for CNC and less than 0.1 wt% for TEMPO-CNF. The model can also be used to estimate the salt concentration in a sample. Moreover, a rheological "flow index" parameter was developed to compare the effects of morphology and surface charge more robustly by combining the rheological data for samples at different concentrations to obtain a "rheological fingerprint" of a material. Zero-shear viscosity η_0 is first determined from the Cross model, and the flow index k is then defined through the scaling relation $\log_{10}(\eta_0) = k \cdot c - \log_{10}(\eta_{water})$, c being the CNM concentration and η_{water} the water viscosity. The flow index decreases with higher homogenization energy and higher surface charge, and a power law relationship was found between the flow index and the homogenization energy input (Flow Index = $7.04 \cdot \text{Energy}^{-0.18}$). The flow index condenses all viscosity data points of a family of flow curves for the same CNM sample (in this case TEMPO-CNF) at different concentrations into a

single parameter, thus establishing a clear and concise one-to-one relationship between rheology and microstructural characteristics.

Chapter 5 demonstrated the capabilities and limitations of using a Brookfield viscometer, an industrial-grade viscometer, to characterize the CNC suspensions. Similar to the characterization and analysis using the rheometer in the previous chapters, test protocols were first developed to obtain reliable and reproducible viscosity results. Because of the limited torque range of the viscometer, different spindles must be used to cover the full range of rotational speeds from 0.3 to 100 *RPM*. It was found that variations caused by using different spindles were within acceptable error range that is typical for rheometry. Sample-to-sample variations were found to be small as well. Similar to the rheometer, the flow curves measured by the viscometer show shear thinning at all shear rates at high concentrations, while for intermediate concentrations a viscosity plateau at low shear is followed by shear thinning at high shear rates. The three-regime shape, which is typical for CNC flow behaviors at intermediate concentrations in rheometer measurements, was only found in the viscometer after the sample was homogenized with a high-shear dispenser that is capable of breaking down aggregates. At low CNC concentrations, the samples are mostly Newtonian with constant viscosity; increases i viscosity at higher rotational speed are indicative of flow instabilities and represent an artefact of the viscometer design. All flow curves, including those that exhibit the three-regime shape can be accurately described by the combined model $\eta = a'\Omega^{-b'} + \eta'_{\infty} + \frac{\eta'_0 - \eta'_{\infty}}{1+(\lambda'\Omega)^{m'}}$, the same model presented in Chapter 4 but using rotational speed Ω instead of shear rate $\dot{\gamma}$ to avoid complications with converting between rotational speed and shear rate.

Chapter 6 focuses on the dewatering challenge of cellulose nanomaterial (CNM), which is another key barrier towards commercialization. CNMs is typically produced in aqueous suspensions of high water-content (~90 wt% of water for CNC and ~97 wt% for TEMPO-CNF). Thus, dewatering/drying is essential to reduce the transportation cost and for applications that require high concentrations. Nevertheless, the commonly used dewatering methods like evaporation and pressing cause irreversible aggregations and macroscopic concentration gradients that make the dewatered sample inhomogeneous and hard to redisperse, diminishing the advantages these materials offer due to high aspect ratio and nano-scale morphology. As alternative method, reverse dialysis was developed to dewater CNM suspensions to increase their processing range while preserving their beneficial morphological properties. Samples to be dewatered are placed inside a dialysis bag and immersed in polyethylene glycol (PEG) solution. The water removal process is driven by osmotic pressure differences and is most significantly affected by the PEG concentration in the surrounding solution. TEMPO-CNF samples that are dewatered via reverse dialysis are redispersible, if given time to rehydrate, as indicated by the fact that the original viscosity was recovered after subjecting samples to a dewatering-redilution cycle. The generalizability of reverse dialysis is demonstrated by dewatering suspensions of CNC, chitin nanofiber and composites of polyvinyl alcohol (PVA) and TEMPO-CNF. Concentrated and well-dispersed PVA/TEMPO-CNF composite gels can be obtained via reverse dialysis that are difficult to achieve by other methods.

Overall, our work demonstrates that rheology is an effective tool to characterize the cellulose nanomaterials (CNMs) for quality control and processing.

7.2 Future work

7.2.1 Transition from Heterogenous to Homogenous Flow

Flow instability and wall-slip problems caused by heterogenous flow have often been raised as concerns for the rheological measurement of TEMPO-CNF, as they hinder proper interpretation of the rheological results leading to false understanding of microstructural changes in fibril suspensions. By measuring the flow curves and visualizing the flow pattern at the same time, previous studies provide guidelines to identify heterogenous flow as discussed in Chapter 2.2. If the flow curves measured by different geometries overlap (e.g. **Figure 3.11** in Section 3.4.5) then there is no heterogenous flow problem, and this check has been accepted by the CNM community. Nevertheless, there are no systematic studies of the fibril characteristics and the concentrations that are likely to cause flow problems. A follow-up study would be desirable that uses both rheology and the visualization techniques developed in previous studies [150, 187] to investigate the extent of heterogenous flow in TEMPO-CNF suspensions. In particular, it would be of interest to identify the transition from homogenous to heterogenous flow caused by changes in concentrations, fibril morphology and surface charge. Such a study would provide insights for processes in which homogenous flow is critical, for example continuous processing of CNMs into barrier coatings. [48, 245]

7.2.2 CNC Phase Transition Induced by Temperature

Literature reports describe extensive studies of the phase transition of CNC induced by concentration and ionic strength, and a comprehensive phase diagram has been established as discussed in Section 2.2.5. In contrast, studies on temperature induced phase

transitions are very limited (Section 2.2.4). Part of the reason is probably that temperature induced viscosity changes are small compared to the salt-induced changes, and happen in a narrow concentration and temperature range (biphasic and liquid crystalline phase, 30-60 ºC). Non-monotonic viscosity change versus temperature is observed, where the viscosity first decreases then increases with increasing temperature, but the underlying mechanism is unclear. Understanding the phase behavior at different temperatures can help broaden the application of the CNC materials in areas such as flexible electronics. [27]

A follow-up experiment that can be done to study the temperature-influenced flow behaviors based on the results on Section 3.4.7 is measuring the flow curves using well-dispersed CNC suspensions that are prepared by sonication. Shafiei-Sabet *et al.* have shown that the chiral nematic structure and the pitch size become more apparent after sonication. [246] Thus, the rheology may be more sensitive in such samples to microstructural changes induced by elevated temperature. For those concentrations that exhibit non-monotonic viscosity change as a function of temperature, polarized microscope images can be taken to observe if phase change has occurred. In addition to imaging the phase domains, once can also image the phase boundary of the chiral nematic and isotropic phase. [8, 247] Xu *et al.* have suggested that higher temperature may melt the liquid crystalline phase, causing viscosity increased. [127] Moreover, a rheo-optics study that combines rheology and polarized optical microscope imaging can be performed to detect optical changes under shear, especially at low shear rates, where the viscosity change is most apparent. (**Figure 3.18**)

7.2.3 Rheological Parameter for CNC

A rheological flow index was developed in Section 4.3.6 to establish a one-to-one relationship between TEMPO-CNF rheology and the fibril characteristics, which can be used for quality control in TEMPO-CNF manufacturing. The idea can be extended to quality control for producing CNC. The two key properties are the particle size and the surface charge. CNC of different sizes and surface charges need to be produced and their morphology be characterized. Using sulfuric acid hydrolysis, a typical method to produce CNC, [248] Abitbol *et al.* produced CNC of different surface charges, but similar sizes, by varying the acid to cellulose ratio. [175] The surface charge, quantified by sulfur content, ranges from 0.27% to 0.89%, and the corresponding viscosity at 1 s^{-1} decreased from around 5 Pa·s to 0.02 Pa·s, which can very easily be captured by rheology. The particle length can be modified by the acid hydrolysis time. Dong *et al.* produced CNC of lengths ranging from around 390 nm to 177 nm by increasing the hydrolysis time from 10 to 240 minutes. [249] The length difference is obvious under TEM imaging.

Similar to the parameter development procedure for TEMPO-CNF, models need to be fitted to the flow curve at different concentrations to extract the parameters. Unlike TEMPO-CNF flow curves which can fitted mostly by the Cross model, flow curves of CNC can be fitted by the Cross model or the combined model depending on the concentration. One may need to first identify the concentration range where the rheology reflects the change in size or surface charge most sensitively, then decide the appropriate model to fit the flow curves.

It would be interesting to investigate how accurate and sensitive the rheological parameter can reflect the change in the actual particle size values. Since the CNC are rigid nanoparticles, its size – whether length or width are much easier to measure compared to TEMPO-CNF fibrils. Nevertheless, accurate size measurement is still challenging, due to several hard-to-control factors like agglomeration and human bias. [49] Researchers are currently developing ISO standards to measure the size of CNC and compare the results between labs. [250] Development of algorithms to calculate the particle size given an electron microscopy image is also ongoing, which will significantly simplify the process and provide more objective size information of a sample. Thus, a one-to-one relationship between the rheological parameter value and the size value can be established, which can be implemented to the quality control of CNC manufacturing.

7.2.4 Dewatering and Drying of CNM

In Chapter 6, we show that reverse dialysis is an effective dewatering method, as quantified by viscosity, that does not compromise the redispersibility of TEMPO cellulose nanofibrils which is extremely sensitive to aggregation. Viscosity measures the bulk properties of a sample and could be further developed as a standard method to quantify the degree of redispersion. Test protocols and evaluation criteria need to be set up to classify samples as fully redispersed, partially redispersed and non-redispersed. This will help comparing or benchmarking different drying methods/processes.

More work can be performed to investigate polymer composites of CNM prepared using reverse dialysis. We showed that polymer composite gels can be prepared via reverse dialysis with high loadings of well-dispersed CNM. Mechanical testing can be performed

on the gels prepared by this method to investigate whether the strength of the gel increases due to the improved dispersion of CNM. CNM of different morphologies and surface charges can also be mixed with the polymer solution to investigate the effect of composite properties, and can be compared to composites prepared by direct mixing of polymer and concentrated CNM. [251]

The potential of implementing reverse dialysis as a dewatering step in the manufacturing process can be explored. For the CNC produced at InnoTech Alberta, ultrafiltration via membrane separation has been established mainly for purification, and for concentrating the purified CNC suspensions from 0.5 wt% to 3 wt% before the final spray drying step. [225] Thus, reverse dialysis, which also relies on membrane separation techniques similar to ultrafiltration, has the possibility to be incorporated into the system as a final step to produce slurry product, or as an intermediate step to concentrate the materials before drying to powders. Partial dehydration followed by freeze-drying has been shown to improve redispersibility of the freeze-dried CNF. [89] Feasibility tests of reverse dialysis via ultrafiltration membranes need to be performed to understand the process kinetics, and homogeneity and redispersibility of the product. The PEG solution that is used to remove water also be reused by evaporating water or through ultrafiltration to increase the concentration back to its initial level.

Reverse dialysis can also be explored to concentrate electrode suspensions containing CNM, instead of using vacuum filtration to fabricate electrodes used in energy storage devices. [252-254] The microstructure of the electrode composite after water removal needs to be characterized to investigate the resulting homogeneity and porous structure, and the electrode performance must be evaluated. Because reverse dialysis can

remove a significant amount of water without completely drying the CNM (Figure 6.11), these highly concentrated CNMs can potentially be used as separators in solid-state polymer electrolyte batteries, [255] or used as substrates for flexible electronic devices. [256, 257] Their performance can be benchmarked with the CNMs prepared by filtration or pressing.

APPENDIX A. OPTICAL MICROSCOPE AND SCANNING ELECTRON MICROSCOPY (SEM) IMAGES OF CELLULOSE NANOFIBRIL AND TEMPO OXIDIZED CELLULOSE NANOFIBRIL

The samples were observed using the Leica DFC425 optical microscope, and the Leica objectives with magnifications 50x (numerical aperture NA = 0.55), 20x (NA = 0.5) and 10x (NA = 0.25) were used. The theoretical resolution is determined using the equation: wavelength/(2 NA); the wavelength assumed is 568 nm. Thus, for these objectives, the theoretical resolution is 0.52 μm (50x), 0.57 μm (20x) and 1.1 μm (10x). The glass slide was cleaned using isopropyl alcohol. The sample was deposited directly onto the glass slide, and was air dried in the fume hood.

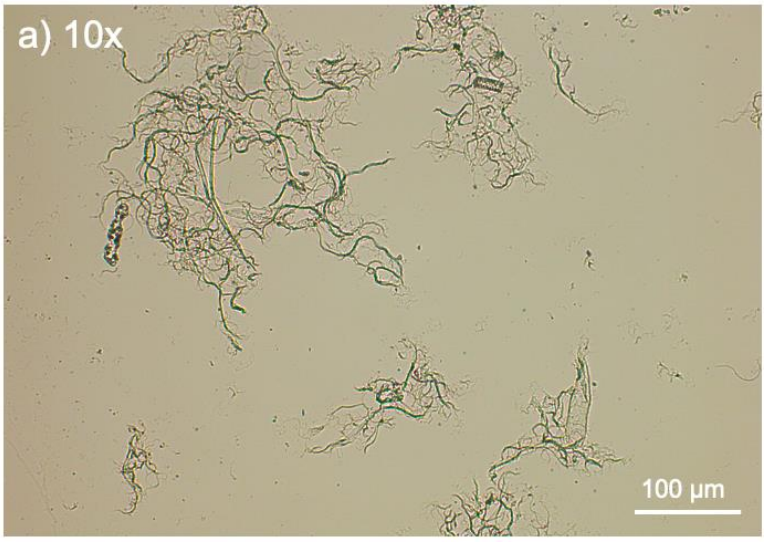

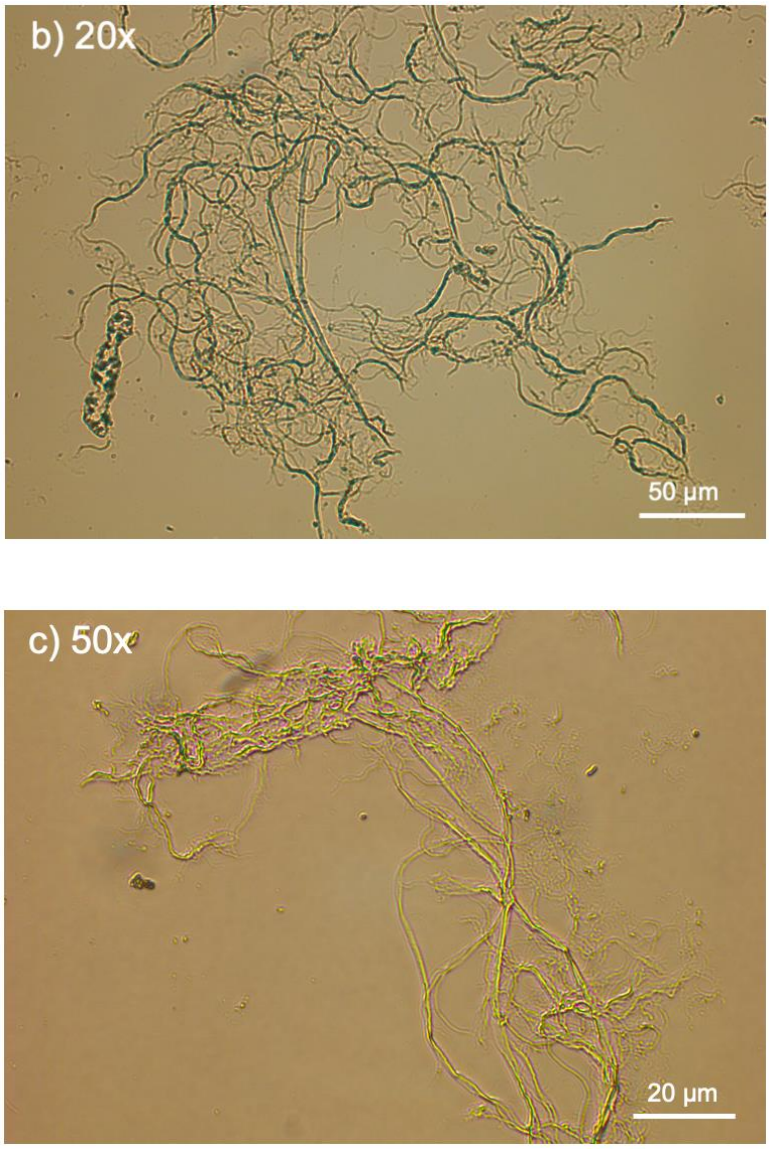

Figure A.1 Cellulose nanofibril (CNF) of 0.01 wt% imaged using the three objectives a) 10x, b) 20x and c) 50x. The large fibrils bundles are observed, and the length of some fibrils exceed 100 µm.

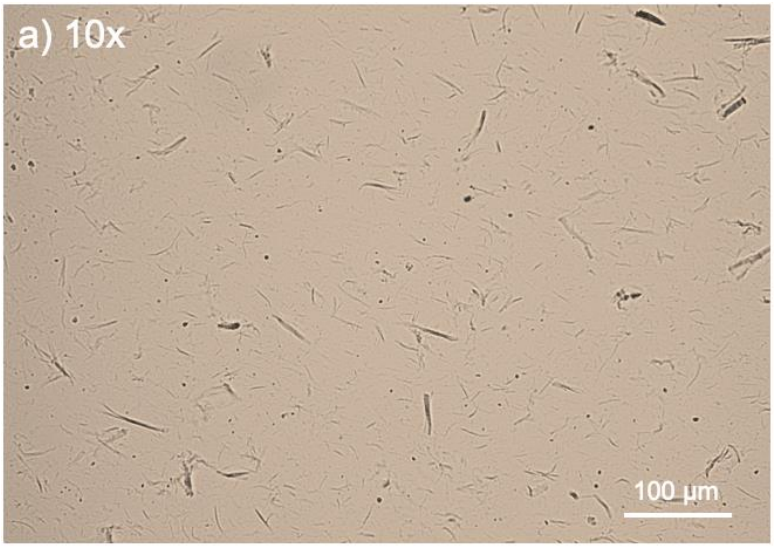
a) 10x
100 µm

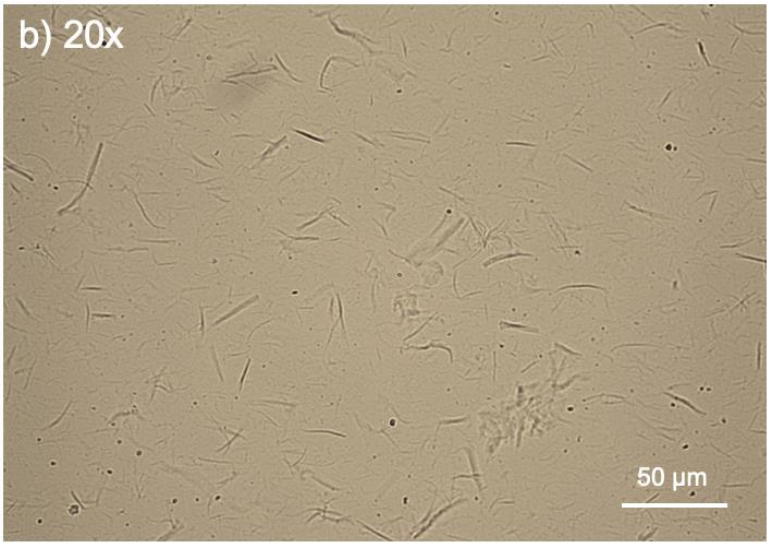
b) 20x
50 µm

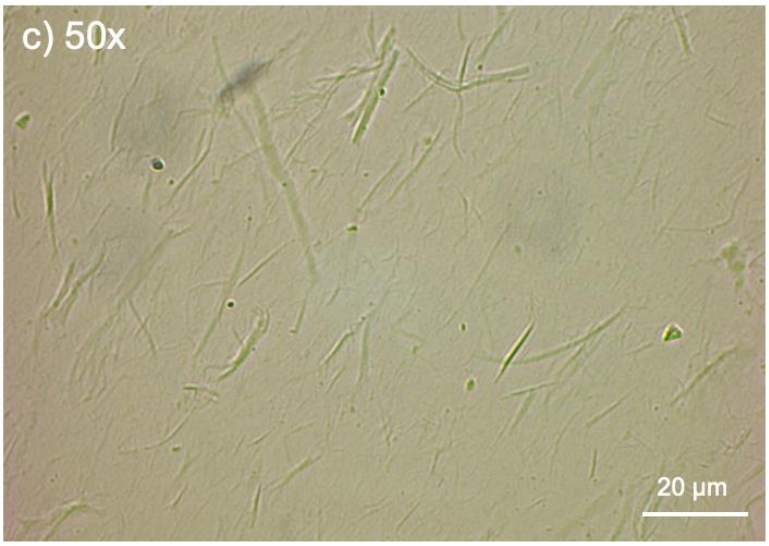

Figure A.2 TEMPO oxidized cellulose nanofibril (TEMPO-CNF) of 0.5 wt% imaged using the three objectives a) 10x, b) 20x and c) 50x. No fibril network can be observed, though fibrils at length scale of 100, 50 and 20 µm all exist. Fibrils smaller than 20 µm can also be seen scatter in the background.

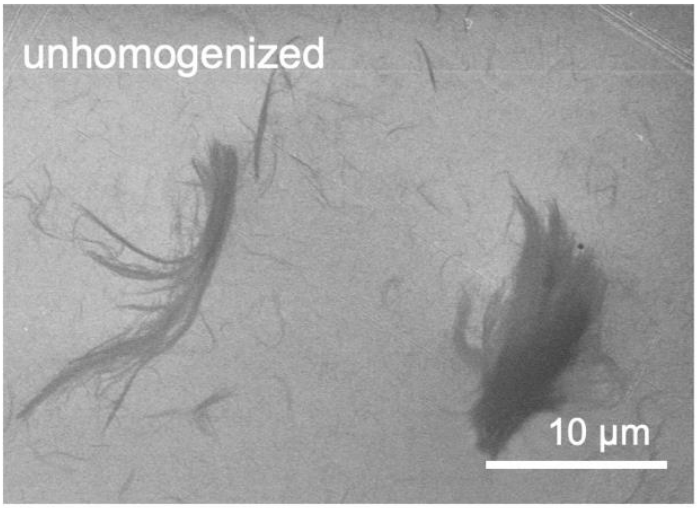

Figure A.3 SEM image of unhomogenized TEMPO-CNF showing the existence of non-fibrillated fragments, though it is only a tiny fraction of the materials. (Compared to the Figure 4.8a in Section 4.3.5) The SEM preparation and imaging procedure are the same as described in Section 3.2.6.

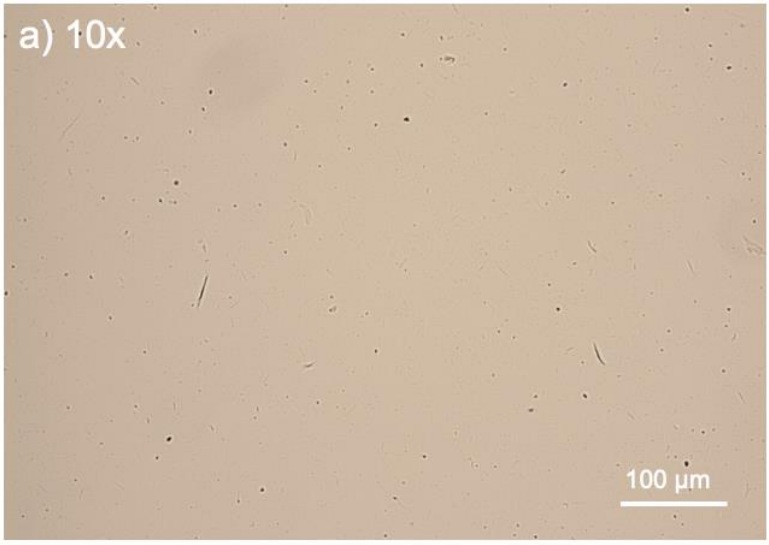
a) 10x
100 µm

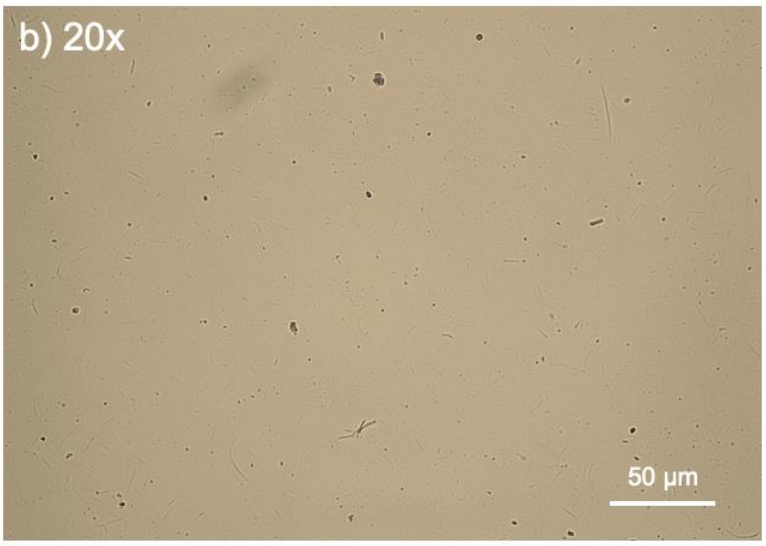
b) 20x
50 µm

Figure A.4 TEMPO oxidized cellulose nanofibril (TEMPO-CNF) of 0.5 wt% that is pressure homogenized for 1 pass at 15000 psi. The sample is imaged using the three objectives a) 10x, b) 20x and c) 50x. No fibrils can be observed clearly at 100 µm and 50 µm. At 20 µm, most of the fibrils are scatter in the background and a partially fibrillated fibril is observed. Compared to Figure A.2, the size of the fibrils are significantly reduced after 1 pass of homogenization.

REFERENCES

1. Ollikainen, M., *Forestry in bioeconomy–smart green growth for the humankind.* Scandinavian Journal of Forest Research, 2014. **29**(4): p. 360-366.

2. Klemm, D., B. Heublein, H.P. Fink, and A. Bohn, *Cellulose: fascinating biopolymer and sustainable raw material.* Angewandte chemie international edition, 2005. **44**(22): p. 3358-3393.

3. Moon, R.J., A. Martini, J. Nairn, J. Simonsen, and J. Youngblood, *Cellulose nanomaterials review: structure, properties and nanocomposites.* Chem Soc Rev, 2011. **40**(7): p. 3941-94.

4. Milanez, D.H., R.M.d. Amaral, L.I.L.d. Faria, and J.A.R. Gregolin, *Assessing nanocellulose developments using science and technology indicators.* Materials Research, 2013. **16**(3): p. 635-641.

5. Dong, H., J.F. Snyder, K.S. Williams, and J.W. Andzelm, *Cation-induced hydrogels of cellulose nanofibrils with tunable moduli.* Biomacromolecules, 2013. **14**(9): p. 3338-3345.

6. Gonzalez, J.S., L.N. Ludueña, A. Ponce, and V.A. Alvarez, *Poly (vinyl alcohol)/cellulose nanowhiskers nanocomposite hydrogels for potential wound dressings.* Materials Science and Engineering: C, 2014. **34**: p. 54-61.

7. Li, V.C.-F., C.K. Dunn, Z. Zhang, Y. Deng, and H.J. Qi, *Direct Ink Write (DIW) 3D Printed Cellulose Nanocrystal Aerogel Structures.* Scientific Reports, 2017. **7**(1): p. 8018.

8. Gray, D.G. and X. Mu, *Chiral nematic structure of cellulose nanocrystal suspensions and films; polarized light and atomic force microscopy.* Materials, 2015. **8**(11): p. 7873-7888.

9. Grüneberger, F., T. Künniger, T. Zimmermann, and M. Arnold, *Rheology of nanofibrillated cellulose/acrylate systems for coating applications.* Cellulose, 2014. **21**(3): p. 1313-1326.

10. Serpa, A., J. Velásquez-Cock, P. Gañán, C. Castro, L. Vélez, and R. Zuluaga, *Vegetable nanocellulose in food science: A review.* Food Hydrocolloids, 2016. **57**: p. 178-186.

11. Heggset, E.B., R. Aaen, T. Veslum, M. Henriksson, S. Simon, and K. Syverud, *Cellulose nanofibrils as rheology modifier in mayonnaise–A pilot scale demonstration.* Food Hydrocolloids, 2020: p. 106084.

12. Sun, X., Q. Wu, S. Lee, Y. Qing, and Y. Wu, *Cellulose nanofibers as a modifier for rheology, curing and mechanical performance of oil well cement.* Scientific reports, 2016. **6**: p. 31654.

13. Li, M.-C., S. Ren, X. Zhang, L. Dong, T. Lei, S. Lee, and Q. Wu, *Surface-chemistry-tuned cellulose nanocrystals in a bentonite suspension for water-based drilling fluids.* ACS Applied Nano Materials, 2018. **1**(12): p. 7039-7051.

14. Satam, C.C., C.W. Irvin, A.W. Lang, J.C.R. Jallorina, M.L. Shofner, J.R. Reynolds, and J.C. Meredith, *Spray-coated multilayer cellulose nanocrystal—chitin nanofiber films for barrier applications.* ACS Sustainable Chemistry & Engineering, 2018. **6**(8): p. 10637-10644.

15. Bertsch, P., M. Arcari, T. Geue, R. Mezzenga, G. Nystrom, and P. Fischer, *Designing Cellulose Nanofibrils for Stabilization of Fluid Interfaces.* Biomacromolecules, 2019. **20**(12): p. 4574-4580

16. Oechsle, A.-L., L. Lewis, W.Y. Hamad, S.G. Hatzikiriakos, and M.J. MacLachlan, *CO2-Switchable Cellulose Nanocrystal Hydrogels.* Chemistry of Materials, 2018. **30**(2): p. 376-385

17. Hasani, M., E.D. Cranston, G. Westman, and D.G. Gray, *Cationic surface functionalization of cellulose nanocrystals.* Soft Matter, 2008. **4**(11): p. 2238-2244.

18. Risteen, B., G. Delepierre, M. Srinivasarao, C. Weder, P. Russo, E. Reichmanis, and J. Zoppe, *Thermally Switchable Liquid Crystals Based on Cellulose Nanocrystals with Patchy Polymer Grafts.* Small, 2018. **14**(46): p. 1802060.

19. Abitbol, T., A. Rivkin, Y. Cao, Y. Nevo, E. Abraham, T. Ben-Shalom, S. Lapidot, and O. Shoseyov, *Nanocellulose, a tiny fiber with huge applications.* Current opinion in biotechnology, 2016. **39**: p. 76-88.

20. Ellebracht, N.C. Engineered Cellulose Nanomaterial Systems for Biomass Upgrading Catalysis. PhD Thesis, Georgia Institute of Technology, 2019.

21. Miyashiro, D., R. Hamano, and K. Umemura, *A review of applications using mixed materials of cellulose, nanocellulose and carbon nanotubes.* Nanomaterials, 2020. **10**(2): p. 186.

22. Salas, C., T. Nypelö, C. Rodriguez-Abreu, C. Carrillo, and O.J. Rojas, *Nanocellulose properties and applications in colloids and interfaces.* Current Opinion in Colloid & Interface Science, 2014. **19**(5): p. 383-396.

23. Kedzior, S.A., V.A. Gabriel, M.A. Dubé, and E.D. Cranston, *Nanocellulose in emulsions and heterogeneous water‐based polymer systems: A review.* Advanced Materials, 2020: p. 2002404.

24. Li, V.C., A. Mulyadi, C.K. Dunn, Y. Deng, and H.J. Qi, *Direct Ink Write 3D Printed Cellulose Nanofiber Aerogel Structures with Highly Deformable, Shape Recoverable, and Functionalizable Properties.* ACS Sustainable Chemistry & Engineering, 2018. **6**(2): p. 2011-2022.

25. Leppiniemi, J., P. Lahtinen, A. Paajanen, R. Mahlberg, S. Metsä-Kortelainen, T. Pinomaa, H. Pajari, I. Vikholm-Lundin, P. Pursula, and V.P. Hytönen, *3D-printable bioactivated nanocellulose–alginate hydrogels.* ACS applied materials & interfaces, 2017. **9**(26): p. 21959-21970.

26. Elder, B., R. Neupane, E. Tokita, U. Ghosh, S. Hales, and Y.L. Kong, *Nanomaterial Patterning in 3D Printing.* Advanced Materials, 2020. **32**(17): p. 1907142.

27. Zhao, D., Y. Zhu, W. Cheng, W. Chen, Y. Wu, and H. Yu, *Cellulose‐Based Flexible Functional Materials for Emerging Intelligent Electronics.* Advanced Materials, 2020: p. 2000619.

28. Wang, Z., Y.H. Lee, S.W. Kim, J.Y. Seo, S.Y. Lee, and L. Nyholm, *Why Cellulose‐Based Electrochemical Energy Storage Devices?* Advanced Materials, 2020: p. 2000892.

29. Salimi, S., R. Sotudeh-Gharebagh, R. Zarghami, S.Y. Chan, and K.H. Yuen, *Production of Nanocellulose and Its Applications in Drug Delivery: A Critical Review.* ACS Sustainable Chemistry & Engineering, 2019. **7**(19): p. 15800-15827.

30. Ferreira, F.V., C.G. Otoni, J. Kevin, H.S. Barud, L.M. Lona, E.D. Cranston, and O.J. Rojas, *Porous nanocellulose gels and foams: Breakthrough status in the development of scaffolds for tissue engineering.* Materials Today, 2020. **37**: p. 126-141.

31. Tummala, G.K., T. Joffre, R. Rojas, C. Persson, and A. Mihranyan, *Strain-induced stiffening of nanocellulose-reinforced poly (vinyl alcohol) hydrogels mimicking collagenous soft tissues.* Soft Matter, 2017. **13**(21): p. 3936-3945.

32. De France, K., Z. Zeng, T. Wu, and G. Nyström, *Functional Materials from Nanocellulose: Utilizing Structure–Property Relationships in Bottom‐Up Fabrication.* Advanced Materials, 2020: p. 2000657.

33. Yang, X., S.K. Biswas, J. Han, S. Tanpichai, M.C. Li, C. Chen, S. Zhu, A.K. Das, and H. Yano, *Surface and Interface Engineering for Nanocellulosic Advanced Materials.* Advanced Materials, 2020: p. 2002264.

34. Oksman, K., Y. Aitomäki, A.P. Mathew, G. Siqueira, Q. Zhou, S. Butylina, S. Tanpichai, X. Zhou, and S. Hooshmand, *Review of the recent developments in cellulose nanocomposite processing.* Compos. Part A Appl. Sci. Manuf., 2016. **83**: p. 2-18.

35. De France, K.J., T. Hoare, and E.D. Cranston, *Review of hydrogels and aerogels containing nanocellulose.* Chemistry of Materials, 2017. **29**(11): p. 4609-4631.

36. Clarkson, C.M., S.M. El Awad Azrak, E.S. Forti, G.T. Schueneman, R.J. Moon, and J.P. Youngblood, *Recent Developments in Cellulose Nanomaterial Composites.* Advanced Materials, 2020: p. 2000718.

37. Ajdary, R., B.L. Tardy, B.D. Mattos, L. Bai, and O.J. Rojas, *Plant nanomaterials and inspiration from nature: Water interactions and hierarchically structured hydrogels.* Advanced Materials, 2020: p. 2001085.

38. Butylina, S., S. Geng, K. Laatikainen, and K. Oksman, *Cellulose nanocomposite hydrogels: From formulation to material properties.* Front. Chem., 2020. **8**: p. 655.

39. Liu, C., H. Du, L. Dong, X. Wang, Y. Zhang, G. Yu, B. Li, X. Mu, H. Peng, and H. Liu, *Properties of nanocelluloses and their application as rheology modifier in paper coating.* Industrial & Engineering Chemistry Research, 2017. **56**(29): p. 8264-8273.

40. Dimic-Misic, K., P.A.C. Gane, and J. Paltakari, *Micro- and nanofibrillated cellulose as a rheology modifier additive in CMC-containing pigment-coating formulations.* Industrial and Engineering Chemistry Research, 2013. **52**(45): p. 16066-16083.

41. Kumar, V., A. Elfving, H. Koivula, D. Bousfield, and M. Toivakka, *Roll-to-roll processed cellulose nanofiber coatings.* Industrial & Engineering Chemistry Research, 2016. **55**(12): p. 3603-3613.

42. Aaen, R., S. Simon, F.W. Brodin, and K. Syverud, *The potential of TEMPO-oxidized cellulose nanofibrils as rheology modifiers in food systems.* Cellulose, 2019. **26**(9): p. 5483-5496.

43. de Amorim, J.D.P., K.C. de Souza, C.R. Duarte, I. da Silva Duarte, F.d.A.S. Ribeiro, G.S. Silva, P.M.A. de Farias, A. Stingl, A.F.S. Costa, and G.M. Vinhas, *Plant and bacterial nanocellulose: production, properties and applications in medicine, food, cosmetics, electronics and engineering. A review.* Environmental Chemistry Letters, 2020. **18**: p. 851–869.

44. Ludwicka, K., M. Jedrzejczak-Krzepkowska, K. Kubiak, M. Kolodziejczyk, T. Pankiewicz, and S. Bielecki, *Medical and cosmetic applications of bacterial nanocellulose*, in *Bacterial NanoCellulose*. 2016, Elsevier. p. 145-165.

45. Lin, N. and A. Dufresne, *Nanocellulose in biomedicine: Current status and future prospect.* European Polymer Journal, 2014. **59**: p. 302-325.

46. Satam, C.C., C.W. Irvin, C.J. Coffey, R.K. Geran, R. Ibarra-Rivera, M.L. Shofner, and J.C. Meredith, *Controlling Barrier and Mechanical Properties of Cellulose*

Nanocrystals by Blending with Chitin Nanofibers. Biomacromolecules, 2019. **21**(2): p. 545-555.

47. Sarwar, M.S., M.B.K. Niazi, Z. Jahan, T. Ahmad, and A. Hussain, *Preparation and characterization of PVA/nanocellulose/Ag nanocomposite films for antimicrobial food packaging.* Carbohydrate polymers, 2018. **184**: p. 453-464.

48. Koppolu, R., J. Lahti, T. Abitbol, A. Swerin, J. Kuusipalo, and M. Toivakka, *Continuous Processing of Nanocellulose and Polylactic Acid into Multilayer Barrier Coatings.* ACS applied materials & interfaces, 2019. **11**(12): p. 11920-11927.

49. Jakubek, Z.J., M. Chen, M. Couillard, T. Leng, L. Liu, S. Zou, U. Baxa, J.D. Clogston, W.Y. Hamad, and L.J. Johnston, *Characterization challenges for a cellulose nanocrystal reference material: dispersion and particle size distributions.* Journal of Nanoparticle Research, 2018. **20**(4): p. 98.

50. Nelson, K., T. Retsina, M. Iakovlev, A. van Heiningen, Y. Deng, J.A. Shatkin, and A. Mulyadi, *American process: Production of low cost nanocellulose for renewable, advanced materials applications*, in *Materials Research for Manufacturing*. 2016, Springer. p. 267-302.

51. Sacui, I.A., R.C. Nieuwendaal, D.J. Burnett, S.J. Stranick, M. Jorfi, C. Weder, E.J. Foster, R.T. Olsson, and J.W. Gilman, *Comparison of the properties of cellulose nanocrystals and cellulose nanofibrils isolated from bacteria, tunicate, and wood processed using acid, enzymatic, mechanical, and oxidative methods.* ACS applied materials & interfaces, 2014. **6**(9): p. 6127-6138.

52. Reid, M.S., M. Villalobos, and E.D. Cranston, *Benchmarking cellulose nanocrystals: from the laboratory to industrial production.* Langmuir, 2016. **33**(7): p. 1583-1598.

53. Abitbol, T., E. Kloser, and D.G. Gray, *Estimation of the surface sulfur content of cellulose nanocrystals prepared by sulfuric acid hydrolysis.* Cellulose, 2013. **20**(2): p. 785-794.

54. Shafiei-Sabet, S., W.Y. Hamad, and S.G. Hatzikiriakos, *Rheology of nanocrystalline cellulose aqueous suspensions.* Langmuir, 2012. **28**(49): p. 17124-17133.

55. Dong, X.M., T. Kimura, J.-F. Revol, and D.G. Gray, *Effects of ionic strength on the isotropic− chiral nematic phase transition of suspensions of cellulose crystallites.* Langmuir, 1996. **12**(8): p. 2076-2082.

56. De Gennes, P.-G. and J. Prost, *The physics of liquid crystals*. Vol. 83. 1993: Oxford university press.

57. Ureña-Benavides, E.E., G. Ao, V.A. Davis, and C.L. Kitchens, *Rheology and phase behavior of lyotropic cellulose nanocrystal suspensions.* Macromolecules, 2011. **44**(22): p. 8990-8998.

58. Zhang, Y., Q. Cheng, C. Chang, and L. Zhang, *Phase transition identification of cellulose nanocrystal suspensions derived from various raw materials.* Journal of Applied Polymer Science, 2018. **135**(24): p. 45702.

59. Nechyporchuk, O., M.N. Belgacem, and J. Bras, *Production of cellulose nanofibrils: A review of recent advances.* Industrial Crops and Products, 2016. **93**: p. 2-25.

60. Fotie, G., S. Limbo, and L. Piergiovanni, *Manufacturing of Food Packaging Based on Nanocellulose: Current Advances and Challenges.* Nanomaterials, 2020. **10**(9): p. 1726.

61. Facchine, E.G., R.J. Spontak, O.J. Rojas, and S.A. Khan, *Shear-dependent Structures of Flocculated Micro/Nanofibrillated Cellulose (MFNC) in Aqueous Suspensions.* Biomacromolecules, 2020. **21**(9): p. 3561-3570

62. Jowkarderis, L. and T.G. van de Ven, *Intrinsic viscosity of aqueous suspensions of cellulose nanofibrils.* Cellulose, 2014. **21**(4): p. 2511-2517.

63. Isogai, A., *Emerging Nanocellulose Technologies: Recent Developments.* Advanced Materials, 2020: p. 2000630.

64. Khalil, H.A., Y. Davoudpour, M.N. Islam, A. Mustapha, K. Sudesh, R. Dungani, and M. Jawaid, *Production and modification of nanofibrillated cellulose using various mechanical processes: a review.* Carbohydrate polymers, 2014. **99**: p. 649-665.

65. Ang, S., V. Haritos, and W. Batchelor, *Effect of refining and homogenization on nanocellulose fiber development, sheet strength and energy consumption.* Cellulose, 2019. **26**(8): p. 4767-4786.

66. Rol, F., B. Karakashov, O. Nechyporchuk, M. Terrien, V.r. Meyer, A. Dufresne, M.N. Belgacem, and J. Bras, *Pilot-scale twin screw extrusion and chemical pretreatment as an energy-efficient method for the production of nanofibrillated cellulose at high solid content.* ACS Sustainable Chemistry & Engineering, 2017. **5**(8): p. 6524-6531.

67. Baati, R., A.B. Mabrouk, A. Magnin, and S. Boufi, *CNFs from twin screw extrusion and high pressure homogenization: A comparative study.* Carbohydrate polymers, 2018. **195**: p. 321-328.

68. Kargarzadeh, H., M. Mariano, D. Gopakumar, I. Ahmad, S. Thomas, A. Dufresne, J. Huang, and N. Lin, *Advances in cellulose nanomaterials.* Cellulose, 2018. **25**(4): p. 2151-2189.

69. Saito, T., Y. Nishiyama, J.-L. Putaux, M. Vignon, and A. Isogai, *Homogeneous suspensions of individualized microfibrils from TEMPO-catalyzed oxidation of native cellulose.* Biomacromolecules, 2006. **7**(6): p. 1687-1691.

70. Saito, T., S. Kimura, Y. Nishiyama, and A. Isogai, *Cellulose nanofibers prepared by TEMPO-mediated oxidation of native cellulose.* Biomacromolecules, 2007. **8**(8): p. 2485-2491.

71. Onyianta, A.J., M. Dorris, and R.L. Williams, *Aqueous morpholine pre-treatment in cellulose nanofibril (CNF) production: comparison with carboxymethylation and TEMPO oxidisation pre-treatment methods.* Cellulose, 2018. **25**(2): p. 1047-1064.

72. Chen, J.-H., J.-G. Liu, Y.-Q. Su, Z.-H. Xu, M.-C. Li, R.-F. Ying, and J.-Q. Wu, *Preparation and properties of microfibrillated cellulose with different carboxyethyl content.* Carbohydrate polymers, 2019. **206**: p. 616-624.

73. Noguchi, Y., I. Homma, and Y. Matsubara, *Complete nanofibrillation of cellulose prepared by phosphorylation.* Cellulose, 2017. **24**(3): p. 1295-1305.

74. Yang, H., D. Chen, and T.G. van de Ven, *Preparation and characterization of sterically stabilized nanocrystalline cellulose obtained by periodate oxidation of cellulose fibers.* Cellulose, 2015. **22**(3): p. 1743-1752.

75. Naderi, A., *Nanofibrillated cellulose: properties reinvestigated.* Cellulose, 2017. **24**(5): p. 1933-1945.

76. Isogai, A. and Y. Zhou, *Diverse nanocelluloses prepared from TEMPO-oxidized wood cellulose fibers: Nanonetworks, nanofibers, and nanocrystals.* Current Opinion in Solid State and Materials Science, 2019. **23**(2): p. 101-106.

77. Foster, E.J., R.J. Moon, U.P. Agarwal, M.J. Bortner, J. Bras, S. Camarero-Espinosa, K.J. Chan, M.J. Clift, E.D. Cranston, and S.J. Eichhorn, *Current characterization methods for cellulose nanomaterials.* Chemical Society Reviews, 2018. **47**(8): p. 2609-2679.

78. Miller, J. *Nanocellulose: technology applications, and markets*. in *TAPPI international conference on nanotechnology for renewable materials*. 2014.

79. Miller, J., *Cellulose Nanomaterials: State of the Industry The Road to Commercialization.* Paper Days 2017, 2017.

80. Miller, J., *Nanocellulose: Producers, Products, and Applications: A Guide for End Users*. 2017: TAPPI Press.

81. Davis, C.S., R.J. Moon, S. Ireland, E.J. Foster, L. Johnston, J.A. Shatkin, K. Nelson, A.M. Forster, M.T. Postek, and A.s.E. Vladár, *NIST-TAPPI workshop on*

measurement needs for cellulose nanomaterials. NIST Special Publication, 2015. **1192**.

82. Davis, C.S., R.J. Moon, S. Ireland, E.J. Foster, L. Johnston, J.A. Shatkin, K. Nelson, A.M. Forster, M.T. Postek, and A.s.E. Vladár, *NIST-TAPPI Workshop on Measurement Needs for Cellulose Nanomaterials*. 2015.

83. Sinquefield, S., P.N. Ciesielski, K. Li, D.J. Gardner, and S. Ozcan, *Nanocellulose Dewatering and Drying: Current State and Future Perspectives.* ACS Sustainable Chemistry & Engineering, 2020. **8**(26): p. 9601-9615.

84. Hansen, F., V. Brun, E. Keller, W. Nieh, and M.M. Theodore Wegner, Lisa Friedersdorf *Cellulose Nanomaterials—A Path Towards Commercialization Workshop Report*. 2014, U.S. Department of Agriculture (USDA) and National Nanotechnology Initiative (NNI): Washington D.C., USA.

85. Posada, P., J. Velásquez-Cock, C. Gómez-Hoyos, A.S. Guerra, S. Lyulin, J. Kenny, P. Gañán, C. Castro, and R. Zuluaga, *Drying and redispersion of plant cellulose nanofibers for industrial applications: a review.* Cellulose, 2020. **27**: p. 10649–10670

86. Peng, Y., D.J. Gardner, and Y. Han, *Drying cellulose nanofibrils: in search of a suitable method.* Cellulose, 2012. **19**(1): p. 91-102.

87. Iwamoto, S., K. Abe, and H. Yano, *The effect of hemicelluloses on wood pulp nanofibrillation and nanofiber network characteristics.* Biomacromolecules, 2008. **9**(3): p. 1022-1026.

88. Eyholzer, C., N. Bordeanu, F. Lopez-Suevos, D. Rentsch, T. Zimmermann, and K. Oksman, *Preparation and characterization of water-redispersible nanofibrillated cellulose in powder form.* Cellulose, 2010. **17**(1): p. 19-30.

89. Huang, D., M. Wu, C. Wang, S. Kuga, and Y. Huang, *Effect of Partial Dehydration on Freeze-Drying of Aqueous Nanocellulose Suspension.* ACS Sustainable Chemistry & Engineering, 2020. **8**(30): p. 11389-11395.

90. Hietala, M., S. Sain, and K. Oksman, *Highly redispersible sugar beet nanofibers as reinforcement in bionanocomposites.* Cellulose, 2017. **24**(5): p. 2177-2189.

91. Jongaroontaprangsee, S., N. Chiewchan, and S. Devahastin, *Production of nanofibrillated cellulose with superior water redispersibility from lime residues via a chemical-free process.* Carbohydrate polymers, 2018. **193**: p. 249-258.

92. Missoum, K., J. Bras, and M.N. Belgacem, *Water redispersible dried nanofibrillated cellulose by adding sodium chloride.* Biomacromolecules, 2012. **13**(12): p. 4118-4125.

93. Butchosa, N. and Q. Zhou, *Water redispersible cellulose nanofibrils adsorbed with carboxymethyl cellulose.* Cellulose, 2014. **21**(6): p. 4349-4358.

94. Wang, L., J.E. Sanders, D.G. Gardner, and Y. Han, *In-situ modification of cellulose nanofibrils by organosilanes during spray drying.* Industrial Crops and Products, 2016. **93**: p. 129-135.

95. Xu, Y., A.D. Atrens, and J.R. Stokes, *Rheology and microstructure of aqueous suspensions of nanocrystalline cellulose rods.* Journal of Colloid and Interface Science, 2017. **496**: p. 130-140.

96. Larson, R.G., *The structure and rheology of complex fluids*. Vol. 150. 1999: Oxford university press New York.

97. Wissbrun, K.F., *Rheology of rod‐like polymers in the liquid crystalline state.* Journal of Rheology, 1981. **25**(6): p. 619-662.

98. Walker, L. and N. Wagner, *Rheology of region I flow in a lyotropic liquid‐crystal polymer: The effects of defect texture.* Journal of Rheology, 1994. **38**(5): p. 1525-1547.

99. Shafiei-Sabet, S. Shear rheology of cellulose nanocrystal (CNC) aqueous suspensions. University of British Columbia, 2013.

100. Haywood, A.D. and V.A. Davis, *Effects of liquid crystalline and shear alignment on the optical properties of cellulose nanocrystal films.* Cellulose, 2017. **24**(2): p. 705-716.

101. Lu, A., U. Hemraz, Z. Khalili, and Y. Boluk, *Unique viscoelastic behaviors of colloidal nanocrystalline cellulose aqueous suspensions.* Cellulose, 2014. **21**(3): p. 1239-1250.

102. Bercea, M. and P. Navard, *Shear dynamics of aqueous suspensions of cellulose whiskers.* Macromolecules, 2000. **33**(16): p. 6011-6016.

103. Qiao, C., G. Chen, J. Zhang, and J. Yao, *Structure and rheological properties of cellulose nanocrystals suspension.* Food Hydrocolloids, 2016. **55**: p. 19-25.

104. Haywood, A.D., K.M. Weigandt, P. Saha, M. Noor, M.J. Green, and V.A. Davis, *New insights into the flow and microstructural relaxation behavior of biphasic cellulose nanocrystal dispersions from RheoSANS.* Soft matter, 2017. **13**(45): p. 8451-8462.

105. Buffa, J.M., U. Casado, V. Mucci, and M.I. Aranguren, *Cellulose nanocrystals in aqueous suspensions: rheology of lyotropic chiral liquid crystals.* Cellulose, 2019. **26**(4): p. 2317-2332.

106. de Souza Lima, M.M. and R. Borsali, *Rodlike cellulose microcrystals: structure, properties, and applications.* Macromolecular rapid communications, 2004. **25**(7): p. 771-787.

107. Oguzlu, H., C. Danumah, and Y. Boluk, *Colloidal behavior of aqueous cellulose nanocrystal suspensions.* Current Opinion in Colloid & Interface Science, 2017. **29**: p. 46-56.

108. El Achaby, M., N. El Miri, H. Hannache, S. Gmouh, V. Trabadelo, A. Aboulkas, and H.B. Youcef, *Cellulose nanocrystals from Miscanthus fibers: insights into rheological, physico-chemical properties and polymer reinforcing ability.* Cellulose, 2018. **25**: p. 6603–6619.

109. Beuguel, Q., J.R. Tavares, P.J. Carreau, and M.-C. Heuzey, *Ultrasonication of spray-and freeze-dried cellulose nanocrystals in water.* Journal of Colloid and Interface Science, 2018. **516**: p. 23-33.

110. Lindström, T., *Aspects on nanofibrillated cellulose (NFC) processing, rheology and NFC-film properties.* Current Opinion in Colloid and Interface Science, 2017. **29**: p. 68-75.

111. Beck, S., J. Bouchard, and R. Berry, *Dispersibility in water of dried nanocrystalline cellulose.* Biomacromolecules, 2012. **13**(5): p. 1486-1494.

112. Gicquel, E., J. Bras, C. Rey, J.-L. Putaux, F. Pignon, B. Jean, and C. Martin, *Impact of sonication on the rheological and colloidal properties of highly concentrated cellulose nanocrystal suspensions.* Cellulose, 2019. **26**: p. 7619-7634.

113. Eberhard, U., H.J. Seybold, M. Floriancic, P. Bertsch, J. Jiménez-Martínez, J.S. Andrade Jr, and M. Holzner, *Determination of the effective viscosity of non-Newtonian fluids flowing through porous media.* Frontiers in Physics, 2019. **7**: p. 71.

114. Hubbe, M.A., P. Tayeb, M. Joyce, P. Tyagi, M. Kehoe, K. Dimic-Misic, and L. Pal, *Rheology of Nanocellulose-rich Aqueous Suspensions: A Review.* BioResources, 2017. **12**(4): p. 9556-9661.

115. Lenfant, G., M. Heuzey, T. van de Ven, and P. Carreau, *Intrinsic viscosity of suspensions of electrosterically stabilized nanocrystals of cellulose.* Cellulose, 2015. **22**(2): p. 1109-1122.

116. Simha, R., *The Influence of Brownian Movement on the Viscosity of Solutions.* The Journal of physical chemistry, 1940. **44**(1): p. 25-34.

117. Fedors, R., *An equation suitable for describing the viscosity of dilute to moderately concentrated polymer solutions.* Polymer, 1979. **20**(2): p. 225-228.

118. Boluk, Y., R. Lahiji, L. Zhao, and M.T. McDermott, *Suspension viscosities and shape parameter of cellulose nanocrystals (CNC).* Colloids and Surfaces A: Physicochemical and Engineering Aspects, 2011. **377**(1): p. 297-303.

119. Wu, Q., X. Li, S. Fu, Q. Li, and S. Wang, *Estimation of aspect ratio of cellulose nanocrystals by viscosity measurement: Influence of surface charge density and NaCl concentration.* Cellulose, 2017. **24**(8): p. 3255-3264.

120. Li, M.-C., Q. Wu, K. Song, S. Lee, Y. Qing, and Y. Wu, *Cellulose nanoparticles: structure–morphology–rheology relationships.* ACS Sustainable Chemistry & Engineering, 2015. **3**(5): p. 821-832.

121. Pamies, R., J.G.H. Cifre, M.d.C.L. Martínez, and J.G. de la Torre, *Determination of intrinsic viscosities of macromolecules and nanoparticles. Comparison of single-point and dilution procedures.* Colloid and Polymer Science, 2008. **286**(11): p. 1223-1231.

122. Curvale, R., M. Masuelli, and A.P. Padilla, *Intrinsic viscosity of bovine serum albumin conformers.* International journal of biological macromolecules, 2008. **42**(2): p. 133-137.

123. Molnes, S.N., K.G. Paso, S. Strand, and K. Syverud, *The effects of pH, time and temperature on the stability and viscosity of cellulose nanocrystal (CNC) dispersions: implications for use in enhanced oil recovery.* Cellulose, 2017. **24**(10): p. 4479-4491.

124. Vanderfleet, O.M., M.S. Reid, J. Bras, L. Heux, J. Godoy-Vargas, M.K. Panga, and E.D. Cranston, *Insight into thermal stability of cellulose nanocrystals from new hydrolysis methods with acid blends.* Cellulose, 2019. **56**: p. 507–528.

125. Heggset, E.B., G. Chinga-Carrasco, and K. Syverud, *Temperature stability of nanocellulose dispersions.* Carbohydrate polymers, 2017. **157**: p. 114-121.

126. Pan, J., W. Hamad, and S.K. Straus, *Parameters affecting the chiral nematic phase of nanocrystalline cellulose films.* Macromolecules, 2010. **43**(8): p. 3851-3858.

127. Xu, Y. Rheology and structure of aqueous nanocrystalline cellulose suspensions. Doctoral Thesis, The University of Queensland, 2019.

128. Guido, S. and N. Grizzuti, *Phase separation effects in the rheology of aqueous solutions of hydroxypropylcellulose.* Rheologica acta, 1995. **34**(2): p. 137-146.

129. Guido, S., *Phase behavior of aqueous solutions of hydroxypropyl cellulose.* Macromolecules, 1995. **28**(13): p. 4530-4539.

130. Chau, M., S.E. Sriskandha, D. Pichugin, H.l. Thérien-Aubin, D. Nykypanchuk, G.g. Chauve, M. Méthot, J. Bouchard, O. Gang, and E. Kumacheva, *Ion-mediated*

gelation of aqueous suspensions of cellulose nanocrystals. Biomacromolecules, 2015. **16**(8): p. 2455-2462.

131. Nordenström, M., A. Fall, G. Nyström, and L. Wågberg, *Formation of Colloidal Nanocellulose Glasses and Gels.* Langmuir, 2017. **33**(38): p. 9772-9780.

132. Lenfant, G., M.-C. Heuzey, T.G. van de Ven, and P.J. Carreau, *A comparative study of ECNC and CNC suspensions: effect of salt on rheological properties.* Rheologica Acta, 2017. **56**(1): p. 51-62.

133. Shafiei-Sabet, S., W. Hamad, and S. Hatzikiriakos, *Ionic strength effects on the microstructure and shear rheology of cellulose nanocrystal suspensions.* Cellulose, 2014. **21**(5): p. 3347-3359.

134. Cherhal, F., F. Cousin, and I. Capron, *Influence of charge density and ionic strength on the aggregation process of cellulose nanocrystals in aqueous suspension, as revealed by small-angle neutron scattering.* Langmuir, 2015. **31**(20): p. 5596-5602.

135. Peddireddy, K.R., I. Capron, T. Nicolai, and L. Benyahia, *Gelation Kinetics and Network Structure of Cellulose Nanocrystals in Aqueous Solution.* Biomacromolecules, 2016. **17**(10): p. 3298-3304.

136. Phan-Xuan, T., A. Thuresson, M. Skepö, A. Labrador, R. Bordes, and A. Matic, *Aggregation behavior of aqueous cellulose nanocrystals: the effect of inorganic salts.* Cellulose, 2016. **23**(6): p. 3653-3663.

137. Beck, S. and J. Bouchard, *Ionic strength control of sulfated cellulose nanocrystal suspension viscosity.* TAPPI Journal, 2016. **15**(6): p. 363-372.

138. Bertsch, P., S. Isabettini, and P. Fischer, *Ion-induced hydrogel formation and nematic ordering of nanocrystalline cellulose suspensions.* Biomacromolecules, 2017. **18**(12): p. 4060-4066.

139. Li, C., J. Evans, N. Wang, T. Guo, and S. He, *pH dependence of the chirality of nematic cellulose nanocrystals.* Scientific Reports, 2019. **9**(1): p. 1-7.

140. Xu, Y., A.D. Atrens, and J.R. Stokes, *"Liquid, Gel and Soft Glass" phase transitions and rheology of nanocrystalline cellulose suspensions as a function of concentration and salinity.* Soft Matter, 2018. **14**(10): p. 1953-1963.

141. Xu, Y., A.D. Atrens, and J.R. Stokes, *Liquid crystal hydroglass formed via phase separation of nanocellulose colloidal rods.* Soft matter, 2019. **15**: p. 1716-1720.

142. Xu, Y., A. Atrens, and J.R. Stokes, *Structure and rheology of liquid crystal hydroglass formed in aqueous nanocrystalline cellulose suspensions.* Journal of colloid and interface science, 2019. **555**: p. 702-713.

143. Xu, Y., A. Atrens, and J.R. Stokes, *A review of nanocrystalline cellulose suspensions: rheology, liquid crystal ordering and colloidal phase behaviour.* Advances in colloid and interface science, 2020. **275**: p. 102076.

144. Bertsch, P., A. Sanchez-Ferrer, M. Bagnani, S. Isabettini, J. Kohlbrecher, R. Mezzenga, and P. Fischer, *Ion-induced formation of nanocrystalline cellulose colloidal glasses containing nematic domains.* Langmuir, 2019. **35**(11): p. 4117-4124

145. Nechyporchuk, O., M.N. Belgacem, and F. Pignon, *Concentration effect of TEMPO-oxidized nanofibrillated cellulose aqueous suspensions on the flow instabilities and small-angle X-ray scattering structural characterization.* Cellulose, 2015. **22**(4): p. 2197-2210.

146. Schenker, M., J. Schoelkopf, P. Gane, and P. Mangin, *Influence of shear rheometer measurement systems on the rheological properties of microfibrillated cellulose (MFC) suspensions.* Cellulose, 2018. **25**(2): p. 961-976.

147. Martoïa, F., P. Dumont, L. Orgéas, M. Belgacem, and J.-L. Putaux, *Micro-mechanics of electrostatically stabilized suspensions of cellulose nanofibrils under steady state shear flow.* Soft Matter, 2016. **12**(6): p. 1721-1735.

148. Meeker, S.P., R.T. Bonnecaze, and M. Cloitre, *Slip and flow in pastes of soft particles: Direct observation and rheology.* Journal of Rheology, 2004. **48**(6): p. 1295-1320.

149. Marze, S., D. Langevin, and A. Saint-Jalmes, *Aqueous foam slip and shear regimes determined by rheometry and multiple light scattering.* Journal of rheology, 2008. **52**(5): p. 1091-1111.

150. Nechyporchuk, O., M.N. Belgacem, and F. Pignon, *Rheological properties of micro-/nanofibrillated cellulose suspensions: wall-slip and shear banding phenomena.* Carbohydrate polymers, 2014. **112**: p. 432-439.

151. Nazari, B., V. Kumar, D.W. Bousfield, and M. Toivakka, *Rheology of cellulose nanofibers suspensions: boundary driven flow.* Journal of Rheology, 2016. **60**(6): p. 1151-1159.

152. Iotti, M., Ø.W. Gregersen, S. Moe, and M. Lenes, *Rheological studies of microfibrillar cellulose water dispersions.* Journal of Polymers and the Environment, 2011. **19**(1): p. 137-145.

153. Tanaka, R., T. Saito, T. Hänninen, Y. Ono, M. Hakalahti, T. Tammelin, and A. Isogai, *Viscoelastic properties of core–shell-structured, hemicellulose-rich nanofibrillated cellulose in dispersion and wet-film states.* Biomacromolecules, 2016. **17**(6): p. 2104-2111.

154. Jowkarderis, L. and T.G. van de Ven, *Rheology of semi-dilute suspensions of carboxylated cellulose nanofibrils.* Carbohydrate polymers, 2015. **123**: p. 416-423.

155. Fneich, F., J. Ville, B. Seantier, and T. Aubry, *Structure and rheology of aqueous suspensions and hydrogels of cellulose nanofibrils: effect of volume fraction and ionic strength.* Carbohydrate Polymers, 2019. **211**: p. 315-321.

156. Agoda-Tandjawa, G., S. Durand, S. Berot, C. Blassel, C. Gaillard, C. Garnier, and J.-L. Doublier, *Rheological characterization of microfibrillated cellulose suspensions after freezing.* Carbohydrate Polymers, 2010. **80**(3): p. 677-686.

157. Naderi, A., T. Lindström, and J. Sundström, *Carboxymethylated nanofibrillated cellulose: rheological studies.* Cellulose, 2014. **21**(3): p. 1561-1571.

158. Pääkkö, M., M. Ankerfors, H. Kosonen, A. Nykänen, S. Ahola, M. Österberg, J. Ruokolainen, J. Laine, P.T. Larsson, and O. Ikkala, *Enzymatic hydrolysis combined with mechanical shearing and high-pressure homogenization for nanoscale cellulose fibrils and strong gels.* Biomacromolecules, 2007. **8**(6): p. 1934-1941.

159. Nechyporchuk, O., M.N. Belgacem, and F. Pignon, *Current progress in rheology of cellulose nanofibril suspensions.* Biomacromolecules, 2016. **17**(7): p. 2311-2320.

160. Besbes, I., S. Alila, and S. Boufi, *Nanofibrillated cellulose from TEMPO-oxidized eucalyptus fibres: effect of the carboxyl content.* Carbohydrate Polymers, 2011. **84**(3): p. 975-983.

161. Naderi, A., T. Lindström, and T. Pettersson, *The state of carboxymethylated nanofibrils after homogenization-aided dilution from concentrated suspensions: a rheological perspective.* Cellulose, 2014. **21**(4): p. 2357-2368.

162. Lin, D., R. Li, P. Lopez-Sanchez, and Z. Li, *Physical properties of bacterial cellulose aqueous suspensions treated by high pressure homogenizer.* Food hydrocolloids, 2015. **44**: p. 435-442.

163. Shogren, R.L., S.C. Peterson, K.O. Evans, and J.A. Kenar, *Preparation and characterization of cellulose gels from corn cobs.* Carbohydrate polymers, 2011. **86**(3): p. 1351-1357.

164. Li, J., X. Wei, Q. Wang, J. Chen, G. Chang, L. Kong, J. Su, and Y. Liu, *Homogeneous isolation of nanocellulose from sugarcane bagasse by high pressure homogenization.* Carbohydrate polymers, 2012. **90**(4): p. 1609-1613.

165. Nechyporchuk, O., F. Pignon, and M.N. Belgacem, *Morphological properties of nanofibrillated cellulose produced using wet grinding as an ultimate fibrillation process.* Journal of materials science, 2015. **50**(2): p. 531-541.

166. Reiner, R. and A. Rudie, *Pilot plant scale-up of TEMPO-pretreated cellulose nanofibrils*, in *Production and applications of cellulose nanomaterials*. 2013, TAPPI Press: Peachtree Corners, GA. p. 177-178.

167. Moberg, T., K. Sahlin, K. Yao, S. Geng, G. Westman, Q. Zhou, K. Oksman, and M. Rigdahl, *Rheological properties of nanocellulose suspensions: effects of fibril/particle dimensions and surface characteristics.* Cellulose, 2017. **24**(6): p. 2499-2510.

168. Mendoza, L., T. Gunawardhana, W. Batchelor, and G. Garnier, *Effects of fibre dimension and charge density on nanocellulose gels.* Journal of Colloid and Interface Science, 2018. **525**: p. 119-125.

169. Maestri, C., M. Abrami, S. Hazan, E. Chistè, Y. Golan, J. Rohrer, A. Bernkop-Schnürch, M. Grassi, M. Scarpa, and P. Bettotti, *Role of sonication pre-treatment and cation valence in the sol-gel transition of nano-cellulose suspensions.* Scientific Reports, 2017. **7**(1): p. 11129.

170. Lee, D., Y. Oh, J.-K. Yoo, J.W. Yi, M.-K. Um, and T. Park, *Rheological study of cellulose nanofiber disintegrated by a controlled high-intensity ultrasonication for a delicate nano-fibrillation.* Cellulose, 2020. **27**(16): p. 9257-9269.

171. Zhou, Y., T. Saito, L. Bergström, and A. Isogai, *Acid-free preparation of cellulose nanocrystals by TEMPO oxidation and subsequent cavitation.* Biomacromolecules, 2018. **19**(2): p. 633-639.

172. Pinto, L.O., J.S. Bernardes, and C.A. Rezende, *Low-energy preparation of cellulose nanofibers from sugarcane bagasse by modulating the surface charge density.* Carbohydrate Polymers, 2019. **218**: p. 145-153.

173. Lasseuguette, E., D. Roux, and Y. Nishiyama, *Rheological properties of microfibrillar suspension of TEMPO-oxidized pulp.* Cellulose, 2008. **15**(3): p. 425-433.

174. Benhamou, K., A. Dufresne, A. Magnin, G. Mortha, and H. Kaddami, *Control of size and viscoelastic properties of nanofibrillated cellulose from palm tree by varying the TEMPO-mediated oxidation time.* Carbohydrate polymers, 2014. **99**: p. 74-83.

175. Abitbol, T., D. Kam, Y. Levi-Kalisman, D.G. Gray, and O. Shoseyov, *Surface charge influence on the phase separation and viscosity of cellulose nanocrystals.* Langmuir, 2018. **34**(13): p. 3925-3933.

176. Bettaieb, F., O. Nechyporchuk, R. Khiari, M.F. Mhenni, A. Dufresne, and M.N. Belgacem, *Effect of the oxidation treatment on the production of cellulose nanofiber suspensions from Posidonia oceanica: The rheological aspect.* Carbohydrate polymers, 2015. **134**: p. 664-672.

177. Wen, Y., Z. Yuan, X. Liu, J. Qu, S. Yang, A. Wang, C. Wang, B. Wei, J. Xu, and Y. Ni, *Preparation and characterization of lignin-containing cellulose nanofibril from poplar high-yield pulp via TEMPO-mediated oxidation and homogenization.* ACS Sustainable Chemistry & Engineering, 2019. **7**(6): p. 6131-6139.

178. Šebenik, U., M. Krajnc, B. Alič, and R. Lapasin, *Ageing of aqueous TEMPO-oxidized nanofibrillated cellulose dispersions: a rheological study.* Cellulose, 2019. **26**: p. 917-931.

179. Taheri, H. and P. Samyn, *Effect of homogenization (microfluidization) process parameters in mechanical production of micro-and nanofibrillated cellulose on its rheological and morphological properties.* Cellulose, 2016. **23**(2): p. 1221-1238.

180. Iwamoto, S., S.-H. Lee, and T. Endo, *Relationship between aspect ratio and suspension viscosity of wood cellulose nanofibers.* Polymer journal, 2014. **46**(1): p. 73-76.

181. Shinoda, R., T. Saito, Y. Okita, and A. Isogai, *Relationship between length and degree of polymerization of TEMPO-oxidized cellulose nanofibrils.* Biomacromolecules, 2012. **13**(3): p. 842-849.

182. Tanaka, R., T. Saito, H. Hondo, and A. Isogai, *Influence of flexibility and dimensions of nanocelluloses on the flow properties of their aqueous dispersions.* Biomacromolecules, 2015. **16**(7): p. 2127-2131.

183. Ishii, D., T. Saito, and A. Isogai, *Viscoelastic evaluation of average length of cellulose nanofibers prepared by TEMPO-mediated oxidation.* Biomacromolecules, 2011. **12**(3): p. 548-550.

184. Tanaka, R., T. Saito, D. Ishii, and A. Isogai, *Determination of nanocellulose fibril length by shear viscosity measurement.* Cellulose, 2014. **21**(3): p. 1581-1589.

185. Dealy, J.M., D.J. Read, and R.G. Larson, *Structure and rheology of molten polymers: from structure to flow behavior and back again*. 2018: Carl Hanser Verlag GmbH Co KG.

186. Ball, R. and T. McLeish, *Dynamic dilution and the viscosity of star-polymer melts.* Macromolecules, 1989. **22**(4): p. 1911-1913.

187. Martoïa, F., C. Perge, P. Dumont, L. Orgéas, M. Fardin, S. Manneville, and M. Belgacem, *Heterogeneous flow kinematics of cellulose nanofibril suspensions under shear.* Soft Matter, 2015. **11**(24): p. 4742-4755.

188. Luo, J., N. Semenikhin, H. Chang, R.J. Moon, and S. Kumar, *Post-sulfonation of cellulose nanofibrils with a one-step reaction to improve dispersibility.* Carbohydrate Polymers, 2018. **181**: p. 247-255.

189. Wang, R., T. Rosen, C. Zhan, S. Chodankar, J. Chen, P.R. Sharma, S.K. Sharma, T. Liu, and B.S. Hsiao, *Morphology and flow behavior of cellulose nanofibers dispersed in glycols.* Macromolecules, 2019. **52**(15): p. 5499-5509.

190. Geng, L., N. Mittal, C. Zhan, F. Ansari, P.R. Sharma, X. Peng, B.S. Hsiao, and L.D. Söderberg, *Understanding the mechanistic behavior of highly charged cellulose nanofibers in aqueous systems.* Macromolecules, 2018. **51**(4): p. 1498-1506.

191. Vadodaria, S.S., A.J. Onyianta, and D. Sun, *High-shear rate rheometry of micro-nanofibrillated cellulose (CMF/CNF) suspensions using rotational rheometer.* Cellulose, 2018. **25**(10): p. 5535-5552.

192. Mohtaschemi, M., K. Dimic-Misic, A. Puisto, M. Korhonen, T. Maloney, J. Paltakari, and M.J. Alava, *Rheological characterization of fibrillated cellulose suspensions via bucket vane viscometer.* Cellulose, 2014. **21**(3): p. 1305-1312.

193. Geng, L., X. Peng, C. Zhan, A. Naderi, P.R. Sharma, Y. Mao, and B.S. Hsiao, *Structure characterization of cellulose nanofiber hydrogel as functions of concentration and ionic strength.* Cellulose, 2017. **24**(12): p. 5417-5429.

194. Liu, Y., K. Gordeyeva, and L. Bergström, *Steady-shear and viscoelastic properties of cellulose nanofibril–nanoclay dispersions.* Cellulose, 2017. **24**(4): p. 1815-1824.

195. CSA, *Cellulose nanomaterials — Test methods for characterization (CAN/CSA-Z5100-17)*. 2017, CSA: Toronto, Ontario, Canada.

196. Beck, S. and J. Bouchard, *Effect of storage conditions on cellulose nanocrystal stability.* TAPPI JOURNAL, 2014. **13**(5): p. 53-61.

197. Mattos, B.D., B.L. Tardy, and O.J. Rojas, *Accounting for substrate interactions in the measurement of cellulose nanofibrils dimensions.* Biomacromolecules, 2019. **20**(7): p. 2657-2665.

198. Sato, J. and V. Breedveld, *Evaporation blocker for cone-plate rheometry of volatile samples.* Applied Rheology, 2005. **15**(6): p. 390-397.

199. Henriksson, M. and L.A. Berglund, *Structure and properties of cellulose nanocomposite films containing melamine formaldehyde.* Journal of Applied Polymer Science, 2007. **106**(4): p. 2817-2824.

200. Chang, H., J. Luo, A.A. Bakhtiary Davijani, A.-T. Chien, P.-H. Wang, H.C. Liu, and S. Kumar, *Individually dispersed wood-based cellulose nanocrystals.* ACS applied materials & interfaces, 2016. **8**(9): p. 5768-5771.

201. Mendoza, L., W. Batchelor, R.F. Tabor, and G. Garnier, *Gelation mechanism of cellulose nanofibre gels: A colloids and interfacial perspective.* Journal of colloid and interface science, 2018. **509**: p. 39-46.

202. Arola, S., M. Ansari, A. Oksanen, E. Retulainen, S.G. Hatzikiriakos, and H. Brumer, *The sol–gel transition of ultra-low solid content TEMPO-cellulose nanofibril/mixed-linkage β-glucan bionanocomposite gels.* Soft matter, 2018. **14**(46): p. 9393-9401.

203. Naderi, A., T. Lindström, and J. Sundström, *Repeated homogenization, a route for decreasing the energy consumption in the manufacturing process of carboxymethylated nanofibrillated cellulose?* Cellulose, 2015. **22**(2): p. 1147-1157.

204. Albornoz-Palma, G., F. Betancourt, R.T. Mendonça, G. Chinga-Carrasco, and M. Pereira, *Relationship between rheological and morphological characteristics of cellulose nanofibrils in dilute dispersions.* Carbohydrate Polymers, 2020. **230**: p. 115588.

205. da Silva, L.C., A. Cassago, L.C. Battirola, M. do Carmo Gonçalves, and R.V. Portugal, *Specimen preparation optimization for size and morphology characterization of nanocellulose by TEM.* Cellulose, 2020. **27**(9): p. 5435--5444.

206. Mourtas, S., M. Haikou, M. Theodoropoulou, C. Tsakiroglou, and S.G. Antimisiaris, *The effect of added liposomes on the rheological properties of a hydrogel: A systematic study.* Journal of colloid and interface science, 2008. **317**(2): p. 611-619.

207. Cross, M.M., *Rheology of non-Newtonian fluids: a new flow equation for pseudoplastic systems.* Journal of colloid science, 1965. **20**(5): p. 417-437.

208. Hule, R.A., R.P. Nagarkar, A. Altunbas, H.R. Ramay, M.C. Branco, J.P. Schneider, and D.J. Pochan, *Correlations between structure, material properties and bioproperties in self-assembled β-hairpin peptide hydrogels.* Faraday Discussions, 2008. **139**: p. 251-264.

209. Crowther, H.M., B.R. Saunders, S.J. Mears, T. Cosgrove, B. Vincent, S.M. King, and G.-E. Yu, *Poly (NIPAM) microgel particle de-swelling: a light scattering and small-angle neutron scattering study.* Colloids and Surfaces A: Physicochemical and Engineering Aspects, 1999. **152**(3): p. 327-333.

210. Liao, J., K.A. Pham, and V. Breedveld, *Rheological characterization and modeling of cellulose nanocrystal and TEMPO-oxidized cellulose nanofibril suspensions.* Cellulose, 2020. **27**(7): p. 3741-3757.

211. Tatsumi, D., S. Ishioka, and T. Matsumoto, *Effect of fiber concentration and axial ratio on the rheological properties of cellulose fiber suspensions.* Nihon Reoroji Gakkaishi, 2002. **30**(1): p. 27-32.

212. Koponen, A.I., *The effect of consistency on the shear rheology of aqueous suspensions of cellulose micro-and nanofibrils: a review.* Cellulose, 2020. **27**(4): p. 1879-1897.

213. Saito, T., T. Uematsu, S. Kimura, T. Enomae, and A. Isogai, *Self-aligned integration of native cellulose nanofibrils towards producing diverse bulk materials.* Soft matter, 2011. **7**(19): p. 8804-8809.

214. Ankerfors, M. Microfibrillated cellulose: Energy-efficient preparation techniques and key properties. Licentiate thesis, KTH Royal Institute of Technology, 2012.

215. Cho, J., M.-C. Heuzey, A. Bégin, and P.J. Carreau, *Viscoelastic properties of chitosan solutions: Effect of concentration and ionic strength.* Journal of Food Engineering, 2006. **74**(4): p. 500-515.

216. Pakravan, M., M.-C. Heuzey, and A. Ajji, *A fundamental study of chitosan/PEO electrospinning.* Polymer, 2011. **52**(21): p. 4813-4824.

217. Klossner, R.R., H.A. Queen, A.J. Coughlin, and W.E. Krause, *Correlation of chitosan's rheological properties and its ability to electrospin.* Biomacromolecules, 2008. **9**(10): p. 2947-2953.

218. Desmaisons, J., E. Boutonnet, M. Rueff, A. Dufresne, and J. Bras, *A new quality index for benchmarking of different cellulose nanofibrils.* Carbohydrate polymers, 2017. **174**: p. 318-329.

219. González-Labrada, E. and D.G. Gray, *Viscosity measurements of dilute aqueous suspensions of cellulose nanocrystals using a rolling ball viscometer.* Cellulose, 2012. **19**(5): p. 1557-1565.

220. Moser, C., M.E. Lindström, and G. Henriksson, *Toward industrially feasible methods for following the process of manufacturing cellulose nanofibers.* BioResources, 2015. **10**(2): p. 2360-2375.

221. Mitschka, P., *Simple conversion of Brookfield RVT readings into viscosity functions.* Rheologica Acta, 1982. **21**(2): p. 207-209.

222. Mezger, T.G., *The rheology handbook: for users of rotational and oscillatory rheometers*. 2006: Vincentz Network GmbH & Co KG.

223. Reiner, R.S. and A.W. Rudie, *Process scale-up of cellulose nanocrystal production to 25 kg per batch at the forest products laboratory.* In: Production and applications of Cellulose nanomaterials, TAPPI Press, Chapter 1.1, 2013; pp. 21-24., 2013. **1**: p. 21-24.

224. Dunlop, M.J., C. Clemons, R. Reiner, R. Sabo, U.P. Agarwal, R. Bissessur, H. Sojoudiasli, P.J. Carreau, and B. Acharya, *Towards the scalable isolation of cellulose nanocrystals from tunicates.* Scientific reports, 2020. **10**(1): p. 1-13.

225. Ngo, T.-D., C. Danumah, and B. Ahvazi, *Production of cellulose nanocrystals at InnoTech Alberta.* Nanocellulose and sustainability. CRC Press, Boca Raton, 2018: p. 269-287.

226. Vauthier, C., B. Cabane, and D. Labarre, *How to concentrate nanoparticles and avoid aggregation?* Eur. J. Pharm. Biopharm, 2008. **69**(2): p. 466-475.

227. Tagalakis, A.D., S. Castellaro, H. Zhou, A. Bienemann, M.M. Munye, D. McCarthy, E.A. White, and S.L. Hart, *A method for concentrating lipid peptide DNA and siRNA nanocomplexes that retains their structure and transfection efficiency.* Int. J. Nanomedicine, 2015. **10**: p. 2673.

228. Li, Z., Z. Zheng, Y. Yang, G. Fang, J. Yao, Z. Shao, and X. Chen, *Robust protein hydrogels from silkworm silk.* ACS sustainable chemistry & engineering, 2016. **4**(3): p. 1500-1506.

229. Uddin, A.J., J. Araki, and Y. Gotoh, *Toward "strong" green nanocomposites: polyvinyl alcohol reinforced with extremely oriented cellulose whiskers.* Biomacromolecules, 2011. **12**(3): p. 617-624.

230. Wetterling, J., K. Sahlin, T. Mattsson, G. Westman, and H. Theliander, *Electroosmotic dewatering of cellulose nanocrystals.* Cellulose, 2018. **25**(4): p. 2321-2329.

231. Liao, J., K.A. Pham, and V. Breedveld, *TEMPO-CNF suspensions in the viscoelastic regime: capturing the effect of morphology and surface charge with a rheological parameter.* Cellulose, 2021. **28**: p. 813–827.

232. Zhou, G., Z. Shao, D.P. Knight, J. Yan, and X. Chen, *Silk fibers extruded artificially from aqueous solutions of regenerated Bombyx mori silk fibroin are tougher than their natural counterparts.* Advanced Materials, 2009. **21**(3): p. 366-370.

233. Trunec, M., *Osmotic drying of gelcast bodies in liquid desiccant.* Journal of the European Ceramic Society, 2011. **31**(14): p. 2519-2524.

234. Jiang, F. and Y.-L. Hsieh, *Self-assembling of TEMPO oxidized cellulose nanofibrils as affected by protonation of surface carboxyls and drying methods.* ACS Sustainable Chemistry & Engineering, 2016. **4**(3): p. 1041-1049.

235. Cheng, D., P. Wei, L. Zhang, and J. Cai, *New Approach for the Fabrication of Carboxymethyl Cellulose Nanofibrils and the Reinforcement Effect in Water-Borne Polyurethane.* ACS Sustainable Chemistry & Engineering, 2019. **7**(13): p. 11850-11860.

236. Häggblom, M. and V.-M. Vuorenpalo, *Method for producing dewatered microfibrillated cellulose. U.S. Patent No. 10,113,005.* 2018.

237. Galanakis, C.M., *Separation of functional macromolecules and micromolecules: from ultrafiltration to the border of nanofiltration.* Trends in Food Science & Technology, 2015. **42**(1): p. 44-63.

238. Hsieh, D.S., M. Lindrud, X. Lu, C. Zordan, L. Tang, and M. Davies, *A process for active pharmaceutical ingredient recovery from tablets using green engineering technology.* Organic Process Research & Development, 2017. **21**(9): p. 1272-1285.

239. Allegretti, C., S. Fontanay, Y. Krauke, M. Luebbert, A. Strini, J. Troquet, S. Turri, G. Griffini, and P. D'Arrigo, *Fractionation of Soda Pulp Lignin in Aqueous Solvent through Membrane-Assisted Ultrafiltration.* ACS Sustainable Chemistry & Engineering, 2018. **6**(7): p. 9056-9064.

240. Endo, R., T. Saito, and A. Isogai, *TEMPO-oxidized cellulose nanofibril/poly (vinyl alcohol) composite drawn fibers.* Polymer, 2013. **54**(2): p. 935-941.

241. Shrestha, S., F. Montes, G.T. Schueneman, J.F. Snyder, and J.P. Youngblood, *Effects of aspect ratio and crystal orientation of cellulose nanocrystals on properties of poly (vinyl alcohol) composite fibers.* Composites Science and Technology, 2018. **167**: p. 482-488.

242. Tanpichai, S. and K. Oksman, *Cross-linked nanocomposite hydrogels based on cellulose nanocrystals and PVA: Mechanical properties and creep recovery.* Composites Part A: Applied Science and Manufacturing, 2016. **88**: p. 226-233.

243. Liu, D., X. Sun, H. Tian, S. Maiti, and Z. Ma, *Effects of cellulose nanofibrils on the structure and properties on PVA nanocomposites.* Cellulose, 2013. **20**(6): p. 2981-2989.

244. Wu, X., X. Han, L. Lv, M. Li, J. You, and C. Li, *Supramolecular proteinaceous biofilms as trapping sponges for biologic water treatment and durable catalysis.* Journal of colloid and interface science, 2018. **527**: p. 117-123.

245. Koppolu, R., T. Abitbol, V. Kumar, A.K. Jaiswal, A. Swerin, and M. Toivakka, *Continuous roll-to-roll coating of cellulose nanocrystals onto paperboard.* Cellulose, 2018. **25**(10): p. 6055-6069.

246. Shafeiei-Sabet, S., W.Y. Hamad, and S.G. Hatzikiriakos, *Influence of degree of sulfation on the rheology of cellulose nanocrystal suspensions.* Rheologica Acta, 2013. **52**(8-9): p. 741-751.

247. Hirai, A., O. Inui, F. Horii, and M. Tsuji, *Phase separation behavior in aqueous suspensions of bacterial cellulose nanocrystals prepared by sulfuric acid treatment.* Langmuir, 2009. **25**(1): p. 497-502.

248. Beck-Candanedo, S., M. Roman, and D.G. Gray, *Effect of reaction conditions on the properties and behavior of wood cellulose nanocrystal suspensions.* Biomacromolecules, 2005. **6**(2): p. 1048-1054.

249. Dong, X.M., J.-F. Revol, and D.G. Gray, *Effect of microcrystallite preparation conditions on the formation of colloid crystals of cellulose.* Cellulose, 1998. **5**(1): p. 19-32.

250. Vanderfleet, O.M. and E.D. Cranston, *Production routes to tailor the performance of cellulose nanocrystals.* Nature Reviews Materials, 2020. **in press**.

251. Zhou, L., H. He, M.-C. Li, K. Song, H. Cheng, and Q. Wu, *Morphological influence of cellulose nanoparticles (CNs) from cottonseed hulls on rheological properties of polyvinyl alcohol/CN suspensions.* Carbohydrate polymers, 2016. **153**: p. 445-454.

252. Hamedi, M.M., A. Hajian, A.B. Fall, K. Hakansson, M. Salajkova, F. Lundell, L. Wagberg, and L.A. Berglund, *Highly conducting, strong nanocomposites based on nanocellulose-assisted aqueous dispersions of single-wall carbon nanotubes.* ACS nano, 2014. **8**(3): p. 2467-2476.

253. Cho, S.J., K.H. Choi, J.T. Yoo, J.H. Kim, Y.H. Lee, S.J. Chun, S.B. Park, D.H. Choi, Q. Wu, and S.Y. Lee, *Hetero‐nanonet rechargeable paper batteries: toward ultrahigh energy density and origami foldability.* Advanced Functional Materials, 2015. **25**(38): p. 6029-6040.

254. Lizundia, E., C.M. Costa, R. Alves, and S. Lanceros-Méndez, *Cellulose and its derivatives for lithium ion battery separators: A review on the processing methods and properties.* Carbohydrate Polymer Technologies and Applications, 2020. **1**: p. 100001.

255. Lizundia, E. and D. Kundu, *Advances in Natural Biopolymer‐Based Electrolytes and Separators for Battery Applications.* Advanced Functional Materials, 2020: p. 2005646.

256. Kim, J.H., D. Lee, Y.H. Lee, W. Chen, and S.Y. Lee, *Nanocellulose for energy storage systems: beyond the limits of synthetic materials.* Advanced Materials, 2019. **31**(20): p. 1804826.

257. Qin, H., K. Fu, Y. Zhang, Y. Ye, M. Song, Y. Kuang, S.-H. Jang, F. Jiang, and L. Cui, *Flexible nanocellulose enhanced Li+ conducting membrane for solid polymer electrolyte.* Energy Storage Materials, 2020. **28**: p. 293-299.